Università degli Studi di Ferrara

DOTTORATO DI RICERCA IN
"FISICA ASTROPARTICELLARE E COSMOLOGIA"

CICLO XXV

COORDINATORE Prof. Vincenzo Guidi

A refined reference Earth model for the geoneutrino studies at Borexino

Settore Scientifico Disciplinare FIS/04

Dottorando
Dott. Chubakov Viacheslav

Tutore
Prof. Fiorentini Giovanni

Co-Tutore
Dr. Mantovani Fabio

Anni 2010/2012

1 Introduction

Structure, composition and evolution of the Earth were always of a great scientific interest. Some measurements have already revealed the general aspects of the planet. Seismology allowed to reconstruct the physical properties and display the crust-mantle-core layer structure. Geochemical analysis of representative rocks established the composition of the crust and top of the mantle; in turn samples of a deep mantle and core are unreachable.

The Bulk Silicate Earth (BSE) models based on cosmo-chemical approach model the bulk chemical composition of the Earth. The CI Carbonaceous Chondrite meteorites are considered to have composition of the solar photosphere and assuming to be basic material for the planet construction [*McDonough and Sun*, 1995; *Palme and O'Neill*, 2003]. However some authors have argued, that other chondrite - enstatite chondrites represent chemical composition of the Earth [*Javoy et al.*, 2010]. Moreover different compositional BSE models, being in agreement on a Th/U of 3.9 and a K/U of 14,000 [*Arevalo et al., 2009*], vary by nearly a factor of three in their U content (i.e., ~10 ng/g [*Javoy et al., 2010; O'Neill and Palme, 2008*], ~20 ng/g [*Allègre et al., 1995; Hart and Zindler, 1986; McDonough and Sun, 1995; Palme and O'Neill, 2003*], and ~30 ng/g [*Anderson, 2007; Turcotte and Schubert, 2002; Turcotte et al., 2001*]).

Thus the detailed knowledge is available only for a thin layer close to the surface and the major part of the Earth is lack from direct observations. Since the deepest hole which has ever been dug is about 12 km deep, and the maximal depth of rock collected on the surface is about 200 km, still far from the radius magnitude (6371 km).

Another topic of debate is understanding of the Earth's energy sources and heat budget. All activities on the planet: movement of tectonic plates, volcanic eruptions, earthquakes, and terrestrial magnetism are powered by Earth heat generation. Though estimates of energy budget have large uncertainties (the central value between 30 to 46 TW) and relative contributions of different sources (radiogenic, gravitational, chemical etc.) are not fixed.

In this regard neutrinos from the decay chains of radioactive elements, such as U, Th, and K, are considered as a new unique probe. Generated inside the Earth, they escape freely and instantaneously to its surface and bring the direct information about its interior. Particularly amount and distribution of Heat Producing Elements (HPEs: U, Th and K) can be evaluated by measuring geo-neutrino flux. It, in turn, permits to test existing BSE models and calculate the radiogenic heat generation.

Use of neutrinos for studying the Earth was first proposed by Eder [*Eder 1966*] and Marx [*Marx 1969*]. However for a long period of time no observations were made due to its

vanishingly small cross-section. In the last years construction of a large volume liquid scintillator detector, which located deep underground to shield it from cosmic radiation, allowed to make first measurements of electron-type antineutrinos.

Borexino located at the Gran Sasso underground laboratories in Italy, and KamLAND at the Kamioka mine in Japan are only two detectors which now are operative. They have already presented their first experimental results of geo-neutrino detection [*Araki et al., 2005, Gando et al., 2011, Bellini et al., 2010*]. Another detector SNO+ at the Sudbury Neutrino Observatory in Canada will start to collect data in 2013 [Chen 2006].

The purpose of this study is to use state-of-the-art information about distribution and amount of HPEs to estimate the geo-neutrino flux and its uncertainties at Gran Sasso area. The detailed study was performed of the region close to Borexino detector, since it gives the major contribution to the signal. Moving away the signal gradually decreases as $1/R^2$.

The dissertation consists of four parts. In the first part, Chapter 2 the main physical properties of geo-neutrinos are discussed. Geophysics as a new field is presented. Chapter 3 is dedicated to the study of amount and distribution of HPE in the main Earth's reservoirs. The detailed study is given to the area around Gran Sasso. In Chapter 4 I calculated the antineutrino flux from nuclear reactors, as it gives the main part of the background. Chapter 5 describes the Borexino detector and summarizes all the information to predict the geo-neutrino signal and background from nuclear reactors. The dissertation is concluded in Chapter 6.

2 Geoneutrinos

2.1 Geoneutrinos from different elements

Geo-neutrinos are neutrinos produced in the decay chains of radioactive isotopes inside the Earth. To the present day few main nuclear isotopes (^{238}U, ^{232}Th, ^{40}K, ^{235}U and ^{87}Rb) remained on the Earth. They have half-lives comparable or longer than Earth's age. Actually neutrinos are produced only in electron capture of ^{40}K. In contrast to Sun, Earth shines mainly antineutrinos. Main properties of these isotopes and (anti)neutrinos from them are summarized in Table 1.

Table 1. Properties of ^{238}U, ^{232}Th, ^{40}K, ^{235}U, and ^{87}Rb and of (anti)neutrinos produced in their decay chains. For each nuclear isotope table presents the natural isotopic mass abundance, half-life, (anti)neutrino maximal energy. Q value, $Q_{eff} = Q - \langle E_{(\nu,\bar{\nu})} \rangle$, antineutrino and heat production rates for unit mass of the isotope $(\varepsilon_{\bar{\nu}}, \varepsilon_H)$, and for unit mass at natural isotopic composition $(\varepsilon'_{\bar{\nu}}, \varepsilon'_H)$ (Nuclear data are taken from [*Firestone and Shirley, 1996*]). The antineutrinos with energy above threshold for inverse beta decay on free proton (E_{th} = 1.806 MeV) are produced only in the decay chains of ^{238}U, ^{232}Th.

Decay	Natural isotopic abundance	$T_{1/2}$ [10^9 yr]	E_{max} [MeV]	Q [MeV]	Q_{eff} [MeV]	$\varepsilon_{\bar{\nu}}$ [kg^{-1}s^{-1}]	ε_H [W/kg]	$\varepsilon'_{\bar{\nu}}$ [kg^{-1}s^{-1}]	ε'_H [W/kg]
$^{238}U \rightarrow {}^{206}Pb + 8^4He + 6e + 6\bar{\nu}$	0.9927	4.47	3.26	51.7	47.7	7.46×10^{7}	0.95×10^{-4}	7.41×10^{7}	0.94×10^{-4}
$^{232}Th \rightarrow {}^{208}Pb + 6^4He + 4e + 4\bar{\nu}$	1.0000	14.0	2.25	42.3	40.4	1.62×10^{7}	0.27×10^{-4}	1.62×10^{7}	0.27×10^{-4}
$^{40}K \rightarrow {}^{40}Ca + e + \bar{\nu}$ (89%)	1.17×10^{-4}	1.28	1.311	1.311	0.590	2.32×10^{8}	2.55×10^{-4}	2.71×10^{4}	2.55×10^{-9}
$^{40}K + e \rightarrow {}^{40}Ar + \nu$ (11%)	1.17×10^{-4}	1.28	0.044	1.505	1.461	-	0.78×10^{-5}	-	0.78×10^{-9}
$^{235}U \rightarrow {}^{207}Pb + 7^4He + 4e + 4\bar{\nu}$	0.0072	0.704	1.23	46.4	44	3.19×10^{8}	0.56×10^{-3}	2.30×10^{6}	0.40×10^{-5}
$^{87}Rb \rightarrow {}^{87}Sr + e + \bar{\nu}$	0.2783	47.5	0.283	0.283	0.122	3.20×10^{6}	0.61×10^{-7}	8.91×10^{5}	0.17×10^{-7}

The energy of antineutrinos from ^{87}Rb is so low that unlikely their flux could be measured. Moreover heat production from Rb and some other rare elements (La, Lu, etc) account for the 1% of the total. Therefore only U, Th and ^{40}K are considered further as the Heat

Producing Elements (HPEs) and unless otherwise specially stated geo-neutrinos refer to antineutrinos produced in the decay chains of these elements.

Geoneutrinos from different elements can be distinguished due to their different energy spectra, e.g. geoneutrinos with energy above 2.25 MeV can be produced only in ^{238}U decay chain. The geoneutrino spectra are needed for calculation of the signal in a detector. Nowadays geoneutrinos are detected via inverse beta decay on free proton:

$$\bar{\nu}_e + p \rightarrow e^+ + n - 1.806\text{MeV} \qquad (1.1)$$

where 1.806 MeV is a threshold of the reaction. Only neutrinos from ^{238}U, ^{232}Th (not those from ^{235}U and ^{40}K) are above it. On these grounds the antineutrino energy spectra from ^{238}U and ^{232}Th decay chains are considered.

2.2 Geoneutrino spectra, cross section, oscillations

In general, the decay chain of an isotope involves many different β decays and the total antineutrino spectrum (in a case of radioactive equilibrium) results from the sum of the normalized individual spectra, with weights of production ratio of the isotopes and branching ratio of the beta decays. The detailed description of its calculation can be found in literature [*Sanshiro, 2005, Fiorentini et al., 2007*]. Here I present only general aspects of it.

The ^{238}U decay chain has nine different β-decays Fig. 1. Only three of them (from ^{234}Pa, ^{214}Bi and ^{210}Tl) produce antineutrinos with energy larger than the threshold 1.806 MeV. The contribution from ^{210}Tl is negligible, due to its small probability.

The ^{232}Th decay chain has four β-decays Fig. 2. Only two of them (from ^{228}Ac and ^{212}Bi) produce antineutrinos with energy larger than the threshold 1.806 MeV.

^{40}K β-decay to ^{40}Ca. The simplified scheme is shown in Fig. 3. Antineutrinos from ^{40}K have lower energy than the threshold 1.806 MeV.

Calculated geo-neutrino spectra from U, Th and K decay chains are shown in Fig. 4.

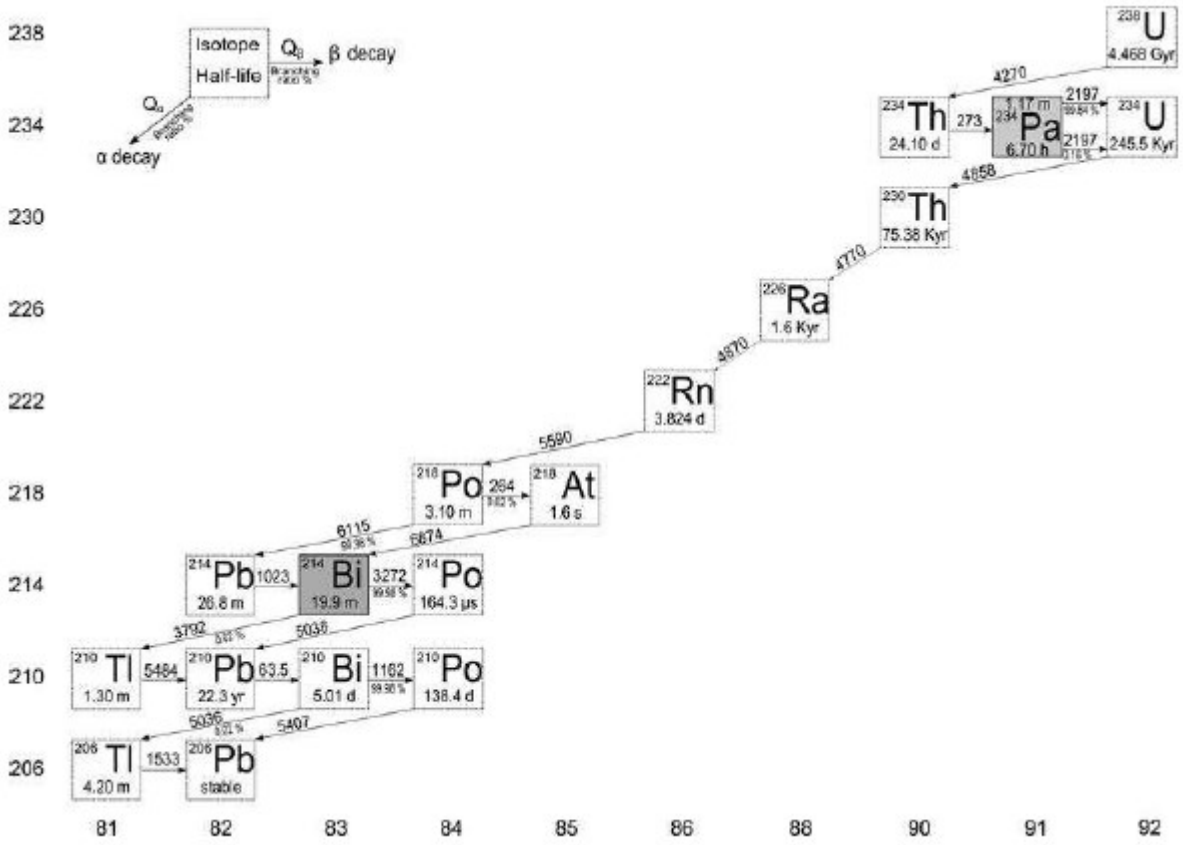

Fig. 1. The ^{238}U decay chain [*Fiorentini et al. 2007*]. The two nuclides inside the grey boxes (^{234}Pa and ^{214}Bi) are the main sources of geo-neutrinos.

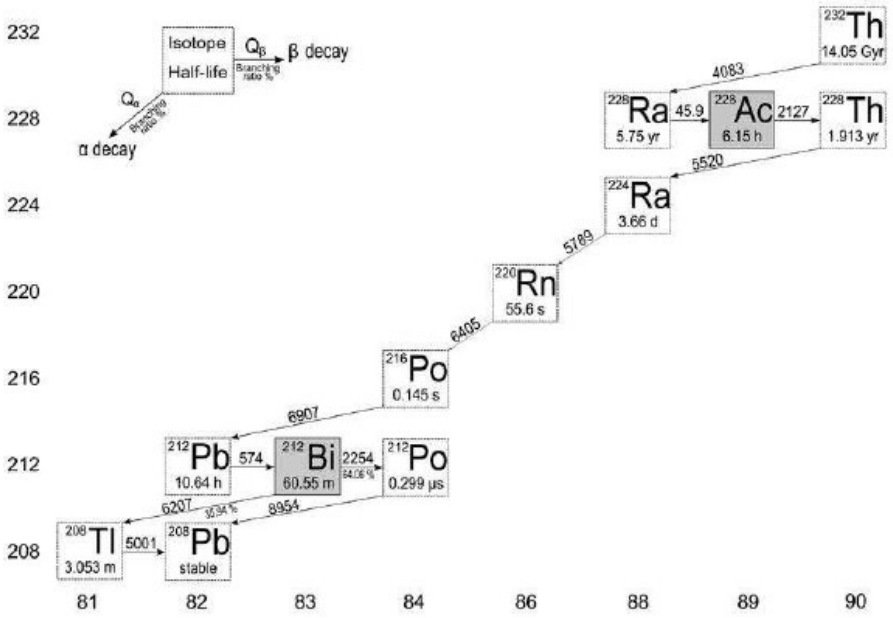

Fig. 2. The ^{232}Th decay chain [*Fiorentini et al. 2007*]. The two nuclides inside the grey boxes (^{228}Ac and ^{212}Bi) are the main sources of geo-neutrinos.

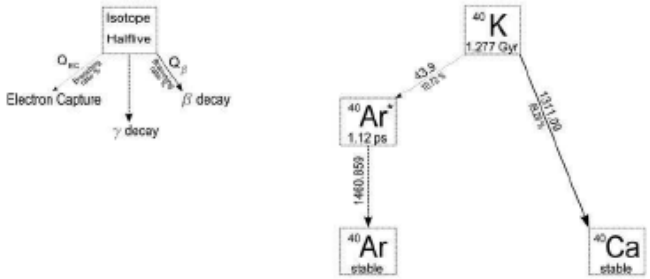

Fig. 3. Decay scheme of ^{40}K [*Fiorentini et al. 2007*].

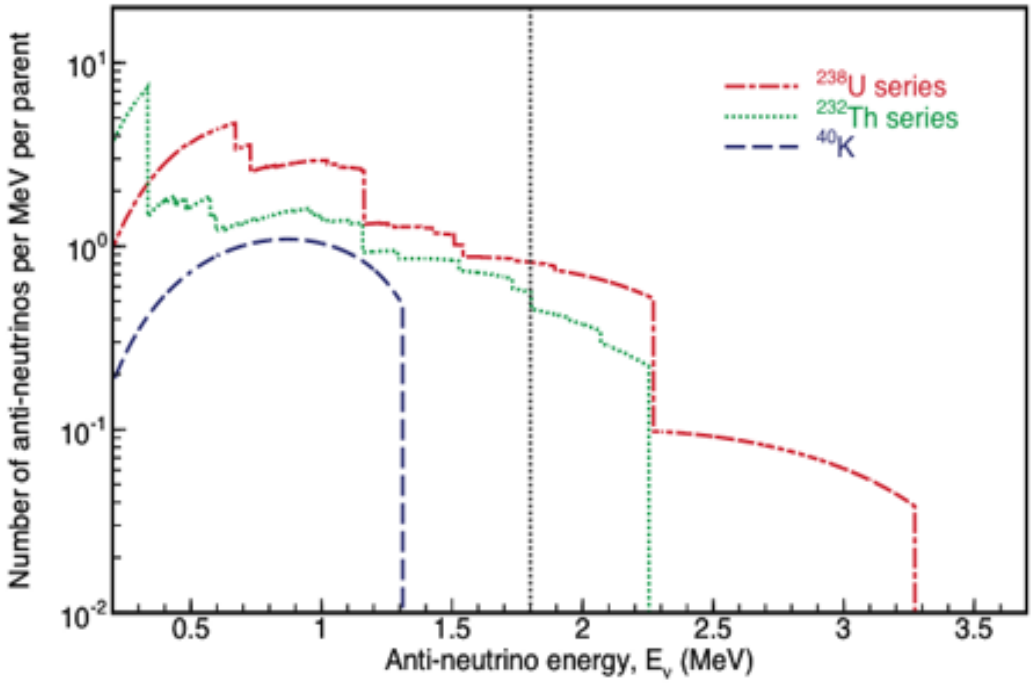

Fig. 4. Geo-neutrino spectra from U, Th and K decay chains. In this calculation, 82 beta decays in the U chain and 70 beta decays in the Th chain are considered. Neutrinos from ^{40}K electron capture are not shown in this figure. [*Enomoto, 2005]*.

The total geoneutrino spectrum depends on the spectra of the individual decays, and on the abundances and spatial distribution of the HPE elements. In Fig. 5 it is shown for a specific model.

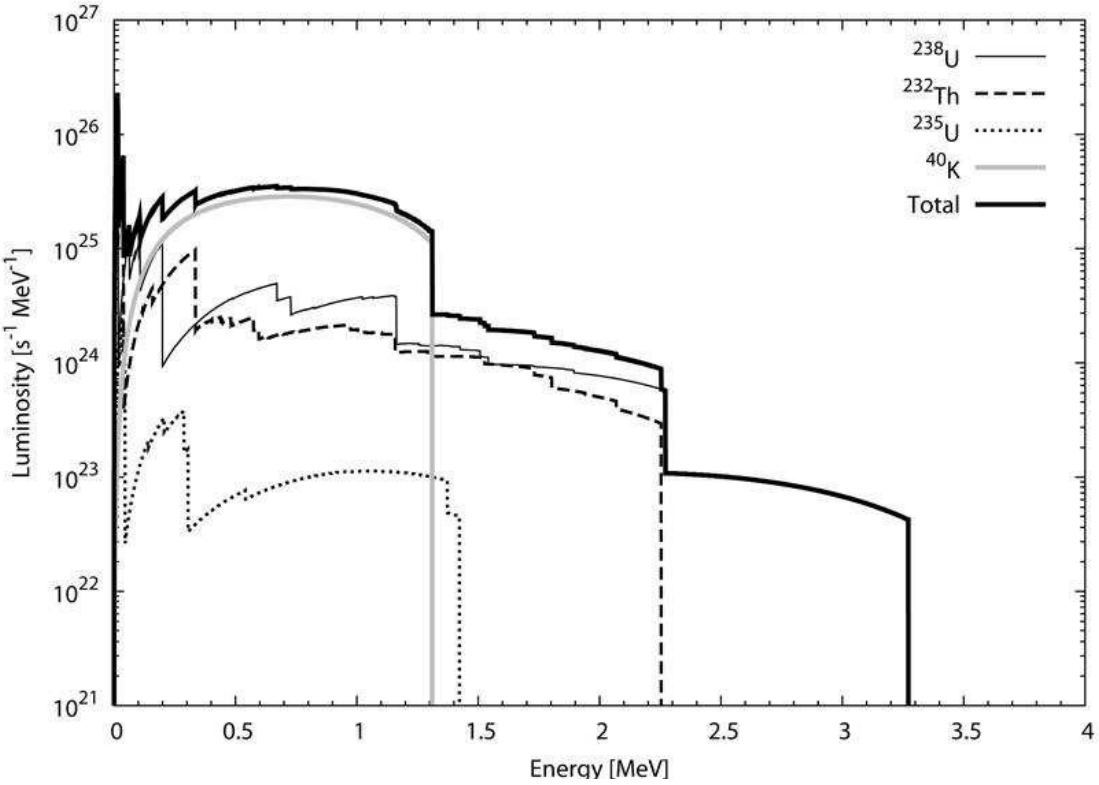

Fig. 5. Differential geo-neutrino luminosity, from [*Enomoto, 2005*]. One assumes the following global abundances: $a(^{238}\mathrm{U})$ =15 ppb, $a(^{235}\mathrm{U})$ = 0.1 ppb, $a(^{232}\mathrm{Th})$ = 55 ppb, $a(^{40}\mathrm{K})$ = 160 ppm [*McDonough, 1999*].

Geoneutrino cross section

A general discussion of neutrino/nucleon interaction cross section can be found in [*Strumia and Vissani, 2003*]. Here a simple approximation for the energies $E_\nu \le 300\mathrm{MeV}$ is considered:

$$\sigma(\bar{\nu}_e p) \approx 10^{-43}[cm^2]\, p_e E_e E_\nu^{-0.07056+0.02018\ln E_\nu - 0.00195\ln^3 E_\nu}, \quad E_e = E_\nu - \Delta, \tag{1.2}$$

where Δ is the neutron-proton mass difference and all energies are in MeV. The uncertainty of cross section calculated by eq. (1.2) is 0.4%.

Calculation of geo-neutrino flux and signal

The number of geoneutrinos with energy $E_{\bar{\nu}}$ produced from the decay chain of element X (^{238}U, ^{232}Th) in time from a unit volume ($d\vec{\mathbf{r}}$) is:

$$dN_X(E_{\bar{\nu}}, \vec{r}) = \frac{\rho(\vec{r}) a_X(r) C_X}{\tau_X m_X} f_X(E_{\bar{\nu}}) d\vec{\mathbf{r}} \tag{1.3}$$

where ρ – density, a_X – elemental mass abundance, C_X – isotopic concentration, τ_X –lifetime and m_X – mass of nucleus X. The energy distribution of antineutrinos $f_X(E_\nu)$ is normalized to the number of antineutrinos n_X emitted per decay chain:

$$n_X = \int dE_\nu f_X(E_\nu). \tag{1.4}$$

The geoneutrino flux decreases with distance as the inverse of square law and obtains by volume integration:

$$\Phi_X(E_\nu) = \int_{V_\oplus} \frac{1}{4\pi\left|\vec{R}-\vec{r}\right|^2} \frac{\rho(\vec{r})a_X(r)C_X}{\tau_X m_X} f_X(E_\nu) p\left(E_\nu, \left|\vec{R}-\vec{r}\right|\right) d\mathbf{r} \tag{1.5}$$

The flux arriving at detectors is smaller than produced due to neutrino oscillations. $p\left(E_\nu, \left|\vec{R}-\vec{r}\right|\right)$ is the survival probability for antineutrino with energy E_ν to reach the detector at $\vec{R}$. Initially predicted theoretically, it was experimentally demonstrated in recent studies that neutrinos can change their flavor and at least two flavors have non zero masses.

$$P_{ee} = 1 - \sin^2(2\theta)\sin^2\left(\frac{\delta m^2 R}{4E}\right) \tag{1.6}$$

where δm is the difference of aqua red masses between two neutrinos, and θ is a mixing angle. The neutrino oscillation parameters δm and $\sin^2(\theta)$ are well determined be the recent studies [Fogli et al. 2011]. The survival probability averaged over a short distance with 1 σ uncertainty is equal to $\langle P_{ee} \rangle \approx 0.551 \pm 0.015$ [*Fogli et al. 2011*] It gives

$$\Phi_X = \langle P_{ee} \rangle \frac{n_X C_X}{4\pi\tau_X m_X} \int_{V_\oplus} \frac{\rho(\vec{r})a_X(r)}{\left|\vec{R}-\vec{r}\right|^2} d\mathbf{r} \tag{1.7}$$

The measured signal depends on number of protons (N_p), which have role of target in reaction (1.1), detection efficiency ($\varepsilon(E_\nu)$) and cross section $\sigma(E_\nu)$:

$$S(X) = N_p \int \varepsilon(E_\nu)\sigma(E_\nu)\Phi_X(E_\nu) dE_\nu \tag{1.8}$$

Assuming to have constant detection efficiency:

$$S(X) = N_p \varepsilon \Phi(X) \int \frac{\sigma(E_\nu) f_X(E_\nu)}{n_X} dE_\nu \tag{1.9}$$

Calculation of an average cross section:

$$\langle \sigma(X) \rangle = \frac{\int \sigma(E_\nu) f_X(E_\nu) dE_\nu}{\int f_X(E_\nu) dE_\nu} \tag{1.10}$$

gives $\langle \sigma(^{238}\mathrm{U}) \rangle = 0.404 \times 10^{-44}\,\mathrm{cm}^2$ and $\langle \sigma(^{232}Th) \rangle = 0.127 \times 10^{-44}\,\mathrm{cm}^2$. It results in ratio between geoneutrino signal and flux [*Fiorentini et al. 2007*]:

$$S(X) = N_p \langle P_{ee}\varepsilon \rangle \Phi(X) \langle \sigma(X) \rangle \tag{1.11}$$

$$S\left(^{238}\mathrm{U}\right) = 12.8 \times \langle P_{ee} \rangle \varepsilon \left(\frac{N_p}{10^{32}} \mathrm{yr}^{-1} \right) \left(\frac{\Phi\left(^{238}\mathrm{U}\right)}{10^6 \,\mathrm{cm}^{-2}\mathrm{s}^{-1}} \right) \tag{1.12}$$

$$S\left(^{232}\mathrm{Th}\right) = 4.0 \times \langle P_{ee} \rangle \varepsilon \left(\frac{N_p}{10^{32}} 10^{-7}\, yr^{-1} \right) \left(\frac{\Phi\left(^{232}\mathrm{Th}\right)}{10^6 \,\mathrm{cm}^{-2}\mathrm{s}^{-1}} \right) \tag{1.13}$$

Signals are expressed in terms of a Terrestrial Neutrino Unit (TNU), defined as one event per 10^{32} target nuclei per year, or 3.17×10^{-40} s^{-1} per target nucleus. This unit is convenient, since, in practice, detectors, which utilize reaction (1.1) to measure antineutrino flux, contain about 1 kton of liquid scintillator. One kton of liquid scintillator contains about 10^{32} free protons (the precise value depending on the chemical composition) and the exposure times are of order of a few years.

2.3 Geoneutrinos and radiogenic heat generation

The total heat released from the Earth's surface is believed to be between 30 and 46 TW [*H.N.Pollack et al. 1993*, *A.M.Hofmeister, 2005*, *Jaupart et al., 2007*]. Estimation is based on compilation of heat flow measurements at different sites. Where no observations are avaliable, heat flow is assumed to be the same as in the places with similar geological settings.

Different sources on the Earth may account for the released heat: radiogenic, gravitational, chemical, etc. According to existing BSE models, decay of radioactive elements contributes from 11 to 21 TW: 11 TW [*Javoy et al. 2010*], 16 TW [*Lyubetskaya and Korenaga, 2007*], 20 TW [*McDonough and Sun, 1995*], 21 TW [*Palme and O'Neil, 2003*].

Geochemical analysis evaluates the average abundances of HPEs in different layers of crust [*Rudnick and Gao, 2003*]. Seismic measurements determined thicknesses and densities of the layers [*Bassin et al., 2000*]. All together it allowed to estimate the mass of HPEs and released heat. On the ground of these data, the radiogenic heat production in the crust accounts for about 8 TW. The rest comes from the mantle and core.

The energy budget influences dynamics and thermal evolution of the Earth and observationally based determination of the radiogenic heat production would provide an important contribution for it understanding.

The minimal amount of radioactive elements in the Earth is the one compatible with lower bounds on measured abundances in the crust. In the same time, from available geochemical and/or geophysical knowledge, one cannot exclude that radioactivity in the present

Earth is enough to account for even the all terrestrial heat flow. This interval is rather large and can be reduced using geo-neutrino data. In fact, for each radioactive isotope there is a strict connection between the geoneutrino luminosity (L) (anti-neutrinos produced in the Earth per unit time), the radiogenic heat production rate (H) and the mass (m) of that isotope in the Earth [*Fiorentini et al. 2007*]:

$$L = 7.46 \times m(^{238}U) + 31.49 \times m(^{235}U) + 1.62 \times m(^{232}Th) + 23.16 \times m(^{40}K)$$

$$H_R = 9.52 \times m(^{238}U) + 55.53 \times m(^{235}U) + 2.67 \times m(^{232}Th) + 2.85 \times m(^{40}K)$$

where units are 10^{24} s^{-1}, 10^{12} W, and 10^{17} kg respectively. Assuming to have natural isotopic abundances (Table 1), equations can be rewritten in terms of masses of these elements:

$$L = 7.64 \times m(U) + 1.62 \times m(Th) + 27.10 \times 10^{-4} \times m(K)$$

$$H_R = 9.85 \times m(U) + 2.67 \times m(Th) + 3.33 \times 10^{-4} \times m(K)$$

Thus after collecting required statistics geo-neutrino measurements would reduce allowed interval of radiogenic heat production in the Earth.

3 Global and local models for studying geoneutrinos in Borexino

Deeper in the Earth, direct observations decrease dramatically, particularly, direct sampling of rocks for which geochemical data may be obtained. On the other hand, geoneutrinos are an extraordinary probe of the deep Earth. These particles carry to the surface information about the chemical composition of the whole planet and, in comparison with other emissions of the planet (e.g., heat or noble gases), they escape freely and instantaneously from the Earth's interior.

The recent geoneutrino experimental results from KamLAND and Borexino detectors reveal the usefulness of analyzing the Earth's geoneutrino flux, as it provides a constraint on the strength of the radiogenic heat power and this, in turn, provides a test of compositional models of the bulk silicate Earth (BSE). This flux is proportional to the amount and distribution of U and Th in the Earth's interior.

A reference model (RM) for geo-neutrino production is a necessary starting point for studying the potential and expectations of detectors at different locations. It models the amount and distribution of neutrino sources inside the Earth. By definition, it should incorporate the best available geological, geochemical and geophysical information on our planet. In practice, it has to be based on selected geophysical and geochemical data and models (when available), on plausible hypotheses (when possible), and admittedly on arbitrary assumptions (when unavoidable) [*Fogli et al., 2006*].

In the last years several such models have been presented in the literature (Mantovani et al., 2004; Fogli et al., 2006; Enomoto et al., 2007; Dye 2010,). Review of these models is given in the next section. In general, geo-neutrino signal is calculated as a sum of contributions from three main reservoirs: crust, mantle and core.

Also a new RM is developed. Earth is considered as the sum of its metallic, silicate, and hydrospheric shells (see Fig. 1). The silicate shell of the Earth (equivalent to the BSE) is considered to be the main repository of U, Th and K, and attention is given on understanding internal differentiation of this region (Fig. 1). The BSE is composed of five dominant domains, or reservoirs: the DM (Depleted Mantle, which is the source of mid-ocean-ridge-basalts -- MORB), the EM (Enriched Mantle, which is the source of Ocean Island Basalts -- OIB), the CC (continental crust), the OC (oceanic crust), and the lithospheric mantle (LM). It follows that BSE = DM + EM + CC + OC + LM. The modern convecting mantle is composed of the DM and the

EM. We do not include a term for a hidden reservoir, which may or may not exist in the BSE; its potential existence is not a consideration of this paper.

Following the discussion in [*McDonough, 2003*], the Earth's core is considered to have negligible amounts of K, Th and U.

Radiogenic heat production in the Earth is also determined by using developed reference model, because it is critical for understanding plate tectonics and the thermal evolution of the Earth.

3.1 Review of the previous estimations

Recently several reference models have been presented in the literature [*Mantovani et al., 2004*, *Fogli et al., 2005*, *Enomoto, 2005*, *Dye, 2010*]. All these models rely on the geophysical 2° × 2° crustal map of [*Bassin et al., 2001, Laske et al. 2003*] and on the density profile of the mantle as given by PREM [*Dziewonski and Anderson, 1981*].

The geoneutrino signals at Gran Sasso National Laboratories predicted by these authors are compared in Table 3.1. Predicted signals are in good agreement with each other. The small differences are due to the adopted abundances of U and Th in the crust and upper mantle, and to the model of mantle. All papers use the BSE mass constraint in order to determine the abundances in the lower portion of the mantle.

Table 3.1. The geo-neutrino signal from U+Th at Gran Sasso area predicted by different authors.

References	$S_{\text{Gran Sasso}}$, TNU
Mantovani et al. [*Mantovani et al., 2004*]	40.5 ± 6.5
Fogli et al. [*Fogli et al., 2005*]	40.5 ± 2.9
Enomoto [*Enomoto, 2005*]	43.1
Dye [*Dye, 2010*]	42 ± 7.2

3.2 Global model of the crust

Crust is a thin spherical shell on the top of the Earth. Its mass is negligible (about 0.5%) in the planetary scale. But, in spite of tiny volume and mass, crust contains about 40% of all radioactive elements presented in the Earth and contributes from 30% to 80% of the total geo-neutrino signal [*Fiorentini et al. 2007*]. Modern detectors are insensitive to directionality, and measure geo-neutrino flux generated from the whole planet (Crust+Mantle+Core). For the aim of the studying deep Earth one need to subtract contribution from the crust. Here the reference model of crust is build with the goal to encompass different published information and estimation of uncertainties, which comes from different constituents.

3.2.1 Geophysical model of the crust

All the previously considered reference models based their studies of crust on CRUST2.0 model of [*Bassin et al. 2000*]. CRUST2.0 has 16,200 tiles with resolution of 2°×2°. It was developed on refraction, reflection seismic measurements as an update of previously published 5°×5° CRUST5.1 model [*Mooney et al., 1998*]. Topography, bathymetry and thickness are given for each tile of 7 layers: ice, water, soft sediments, hard sediments, upper, middle and lower crust. Density and velocity of compressional (Vp) and shear waves (Vs) are determined for 360 key profiles for each tile. The Vp values are based on field measurements, while Vs and density are estimated by using empirical Vp-Vs and Vp-density relationships, respectively [*Mooney et al., 1998*]. For regions lacking field measurements, the seismic velocity structure of the crust is extrapolated from the average crustal structure for regions with similar crustal age and tectonic setting [*Bassin et al., 2000*]. Topography and bathymetry are adopted from a standard database (*ETOPO-5*). The same physical and elastic parameters are reported in a global sediment map digitized on a 1°×1° grid [*Laske and Masters, 1997*]. The accuracies of these models are not specified and they must vary with location and data coverage.

Evaluation of the uncertainties of the crustal structure is complex, as the physical parameters (thickness, density, Vp and Vs) are correlated, and their direct measurements are inhomogeneous over the globe [*Mooney et al., 1998*]. Seismic velocities generally have smaller relative uncertainties than thickness [*Christensen and Mooney, 1995*], since seismic velocities (Vp) are measured directly in the refraction method, while the depths of refracting horizons are successively calculated from the uppermost to the deepest layer measured. The uncertainties of seismic velocities in some previous global crustal models were estimated to be 3-4% [*Holbrook*

et al., 1992; Mooney et al., 1998]. To be conservative, 5% (1-sigma) uncertainties are adopted for both Vp and Vs.

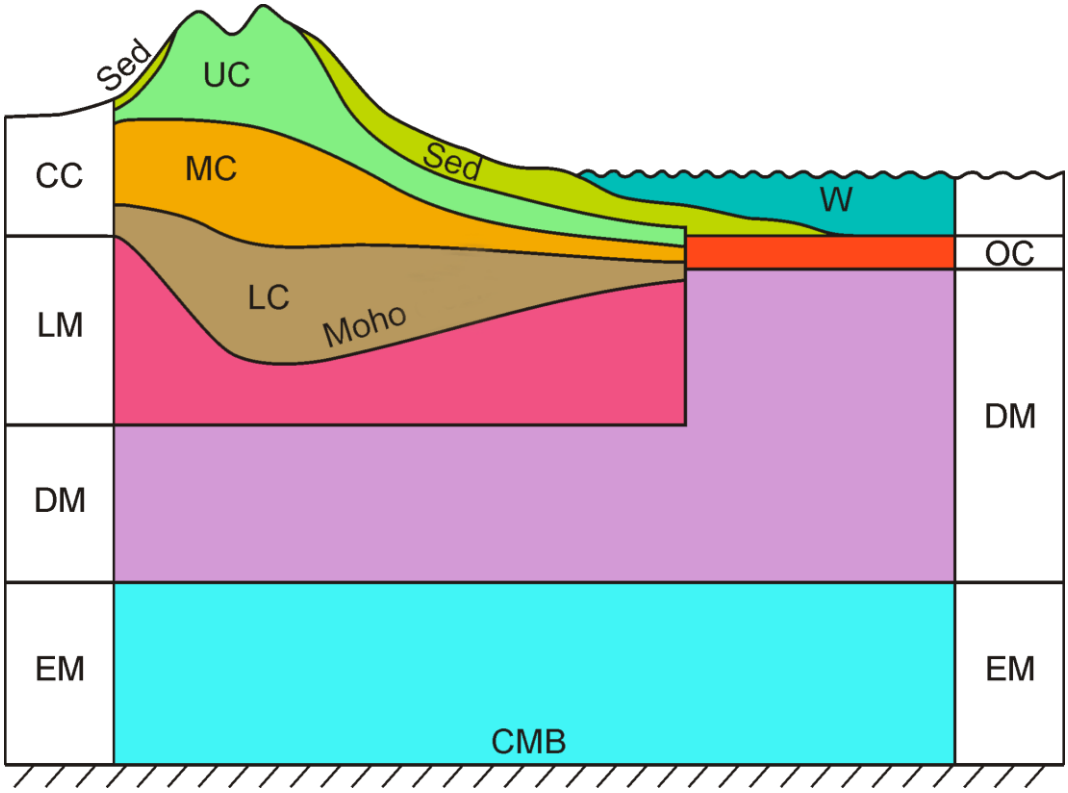

Fig. 3.1: Schematic drawing of the structure of the reference model (not to scale). Under the continental crust (CC; to the left of vertical dashed line), the lithospheric mantle (LM) from depleted mantle (DM), as discussed in the text is distinguished. The DM under the CC and the oceanic crust (OC) is assumed to be chemically homogeneous, but with variable thickness because of the depth variation of the Moho discontinuity as well as the continental lithospheric mantle. The boundary between DM and enriched mantle (EM) is determined by assuming that the mass of the enriched reservoir is 17% of the total mantle. The EM is a homogeneous symmetric shell between the DM and core mantle boundary (CMB).

In the reference model of Earth, presented here (see Fig. 3.1), the crust is digitalized on 1°x1° scale and consists of 8 reservoirs: ice, water, sediments 1, sediments 2, sediments 3, upper crust (UC), middle crust (MC) and lower crust (LC). Thicknesses of ice and water are well known and no uncertainties are associated with it. For each layer of crust model, the Vp, Vs, density and thickness are adopted for three sediment layers from the global sediment map [*Laske and Masters, 1997*]; for upper, middle and lower crust the Vp, Vs, density are adopted from

CRUST 2.0 [*Bassin et al., 2000*]. Thickness of crust is estimated from the comparison of different models, each crustal layer is proportionally rescaled. However thickness of CRUST2.0 gives reliable results and no significant geological discrepancies were found at 2°×2° scale, other existing models of crust obtained from different assumptions, are needed to be considered.

Determination of the CC-OC boundary is another crucial point. Amount of HPEs in the CC and OC crust can be several orders of magnitude different. The geo-neutrino signal, calculated for detectors placed far from the CC-OC boundary (SNO+, Hanohano, etc.), is not affected by small changes of its shape, but for others like KamLAND a movement of boundary can affect the final result. One way to obtain CC-OC boundary is to consider 360 key profiles of CRUST 2.0. Following [*Huang et al. 2013*] in the OC I include the oceanic plateaus and the melt affected oceanic crust of [*Bassin et al. 2000*]. The other crustal types identified in CRUST 2.0 are considered to be CC, including oceanic plateaus comprised of continental crust, which are mainly found in the north of the Scotia Plate, in the Seychelles Plate, in the plateaus around New Zealand (Campbell Plateau, Challenger Plateau, Lord Howe Rise and Chatham Rise), and on the northwest European continental shelf. The final 2°×2° map is presented in Fig. 3.2a. Another way can be based on gravimetrical measurements. The GOCE satellite (Gravity field and steady-state Ocean Circulation Explorer), launched in March, 2009, is the first gravity gradiometry satellite mission dedicated to providing an accurate and detailed global model of the Earth's gravity field with a resolution of about 80 km and an accuracy of 1-2 cm in terms of geoid [*Pail et al., 2011*]. The GEMMA project (GOCE Exploitation for Moho Modeling and Applications) has developed the first global high-resolution map (0.5°×0.5°) of Moho depth by applying regularized spherical harmonic inversion to gravity field data collected by GOCE and preprocessed using the space-wise approach [*Reguzzoni and Tselfes, 2009*; *Reguzzoni and Sampietro, 2012*]. This global crustal model is obtained by dividing the crust into different geological provinces and defining a characteristic density profile for each of them. The gravity field is determined by multiplication of density with thickness. M. Reguzzoni and D. Sampietro have found that crossing of CC to OC is accompanied by a visible change of gravity. As a first approximation it can be considered as a boundary between CC and OC. Fig 3.2b shows the first 0.5°×0.5° map of CC-OC boundary obtained by this approach. The new countour decreases the mass of CC by 5%. The implication of the new CC-OC boundary on the geoneutrino signal needs to be studied in future. Here I consider determination of CC specified in CRUST 2.0, since all the previous models are based somehow on it.

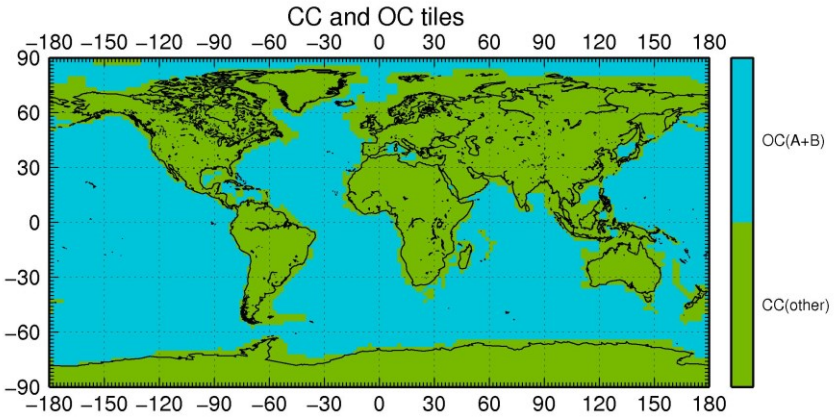

(a)

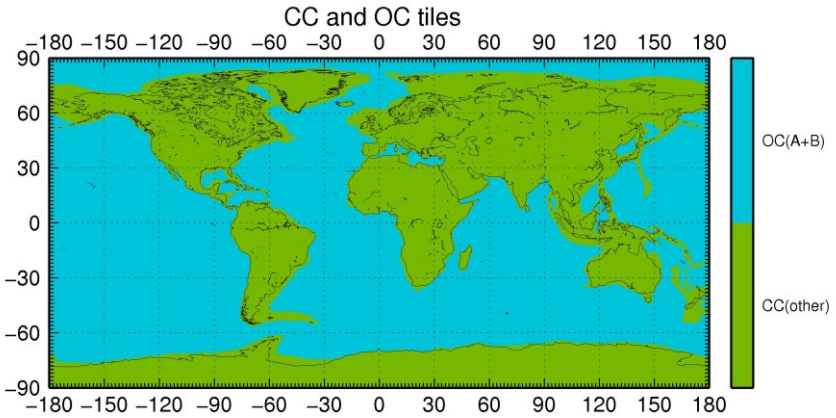

(b)

Fig. 3.2 (a) CC-OC boundary determined on the ground of CRUST 2.0 model [*Bassin et al. 2000*]

(b) CC-OC boundary determined from gravity field measurements [*Reguzzoni and Tselfes, 2009*; *Reguzzoni and Sampietro, 2012*].

The accuracy of the crustal thickness model is crucial to the calculations, as the uncertainties of all boundary depths affect the global crustal mass, the radiogenic heat power and the geoneutrino flux. In particular, uncertainties in Moho depths are a major source of uncertainty in the global crustal model. Although CRUST 2.0 does not provide uncertainties for global crustal thickness, the previous 3SMAC topographic model [*Nataf and Richard, 1996*] included the analysis of crust-mantle boundary developed by [*Čadek and Martinec 1991*], in

which the average uncertainties of continental and oceanic crustal thickness are 5 km and 3 km (1-sigma), respectively. Fig. 3.3a shows the dispersion of the thickness of all CC voxels in CRUST 2.0. The surface area weighted average continental and oceanic crustal thickness (ice and water excluded, sediment included) in CRUST 2.0 is 35.7 km and 7.5 km, respectively (Table 3.3). Distribution of crustal thicknes in CRUST 2.0 model is presented in Fig. 3.4a.

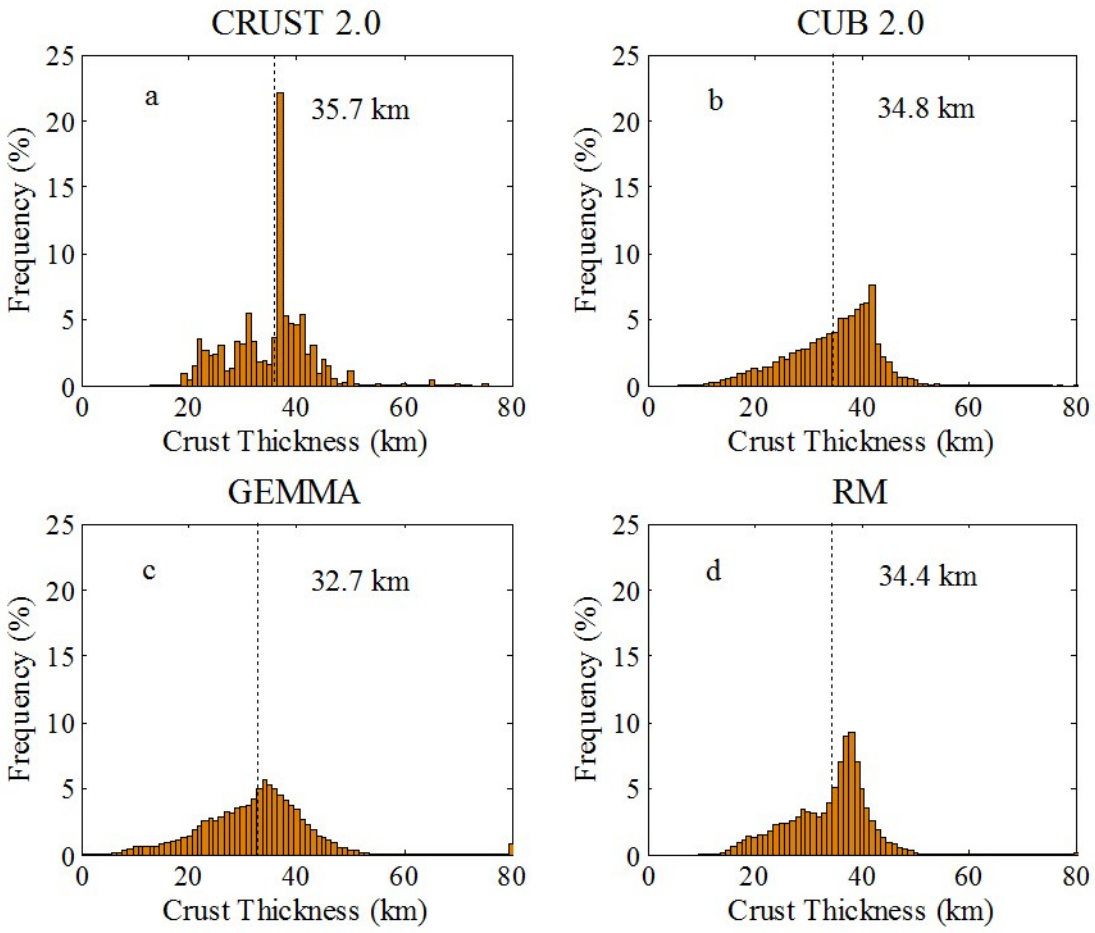

Fig. 3.3: Distributions of continental crustal thickness (without ice or water) in three global crustal models and the reference model (RM). The average thicknesses of the four models, as shown by the dots lines, are calculated from surface area weighted averaging, and so do not coincide with the mean of the distribution. CRUST 2.0: *Laske et al.* [2001]; CUB2.0: *Shapiro and Ritzwoller* [2002]; GEMMA: *Negretti et al.* [2012].

The gravimetric method can be used to check the crustal thickness of CRUST2.0. It is particularly valuable because crustal density cannot be directly determined from seismic refraction field measurements [*Mooney et al. 1998, Tenzer 2009*]. Using the database of GEMMA [*Negretti et al., 2012*], the surface area weighted average thicknesses of CC and OC are 32.7 km and 8.8 km (Table 3.3), respectively (Fig. 3.3b, Fig 3.4b).

Another way to evaluate the global crustal thickness is by utilizing the phase and group velocity measurements of the fundamental mode of Rayleigh and Love waves. [*Shapiro and Ritzwoller 2002*] used a Monte Carlo method to invert surface wave dispersion data for a global shear-velocity model of the crust and upper mantle on a 2°×2° grid (CUB 2.0), with *a priori* constraints (including density) from the CRUST 5.1 model [*Mooney et al., 1998*]. The surface area weighted average thicknesses of the CC and OC are 34.8 km and 7.6 km, respectively (Fig. 3.3c, Fig. 3.4, Table 3.3).

The three global crustal models described above were obtained by different approaches and the constraints on the models are slightly dependent. Ideally, the best solution for a geophysical global crustal model is to combine data from different approaches: reflection and refraction seismic body wave, surface wave dispersion, and gravimetric anomalies. In the reference model the thickness and its associated uncertainty of each 1°×1° crustal voxel is obtained as the mean and the half-range of the three models. The surface area weighted average thicknesses of CC and OC are 34.4 ±4.1 km (Fig. 2d, Fig3.5) and 8.0±2.7 km (1-sigma) for our reference crustal model, respectively. The uncertainties reported here are not based on the dispersions of thicknesses of CC and OC voxels, but are the surface area weighted average of uncertainties of each voxel's thickness. The estimated average CC thickness is about 16% less than 41 km determined previously by [Christensen and Mooney 1995] (see their Fig. 3.3) on the basis of available seismic refraction data at that time and assignment of crustal type sections for areas that were not sampled seismically. However, their compilation did not include continental margins, nor submerged continental platforms, which are included in the three global crustal models used here. Inclusion of these areas will make the CC thinner, on average, than that based solely on exposed continents.

Table 3.2. Thickness of crust and its 1 σ uncertainty (where available) in different models.

Model	$D_{total\ crust}$, km	d_{CC}, km	d_{OC}, km
Crust 2.0	18.4	35.7 ± 5	7.5 ± 3
Cub 2.0	18.9 ± 2.76	34.8	7.6
GEMMA	18.7	32.7	8.8
RM	18.9 ± 2.5	34.4 ± 4.1	8.0± 2.7

The calculated thickness and mass of crust for all layers are presented in Table 3.3. Summing the masses of sediment, upper, middle and lower crust, the total masses of CC and OC are estimated to be $M_{CC} = (20.6\pm2.5) \times10^{21}$ kg and $M_{OC} = (6.7\pm2.3) \times10^{21}$ kg (1-sigma). Thus,

the fractional mass contribution to the BSE of the CC is 0.51% and the contribution of the OC is 0.17%. The uncertainty of crustal thickness of one cell is correlated somehow with the others, since the three crustal models are mutually dependent, and the estimates of crustal thicknesses for some cells are extrapolated from the others. Considering these complexities, a conservative assumption was made, the uncertainty of Moho depth in each cell is totally dependent on that of all the others.

CRUST 2.0

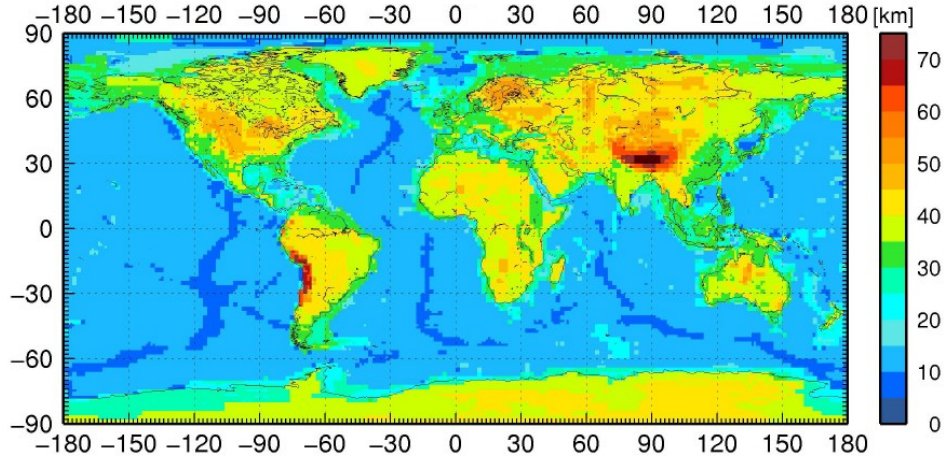

CUB2.0

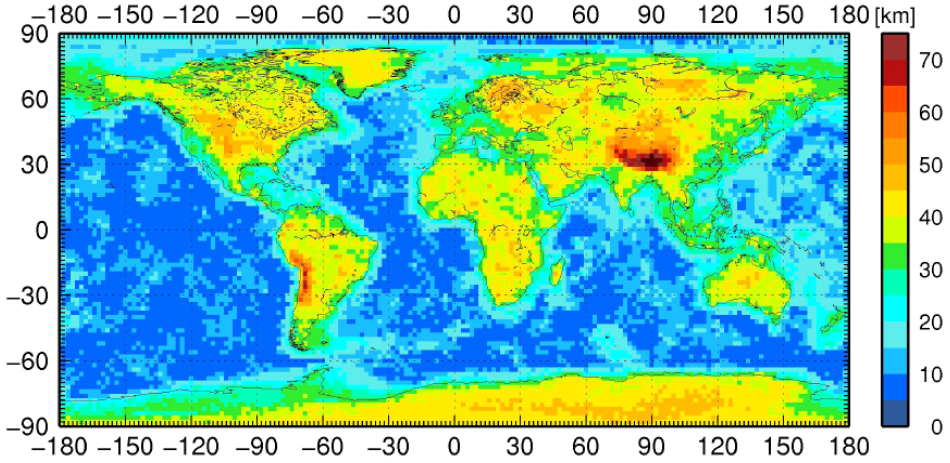

GEMMA

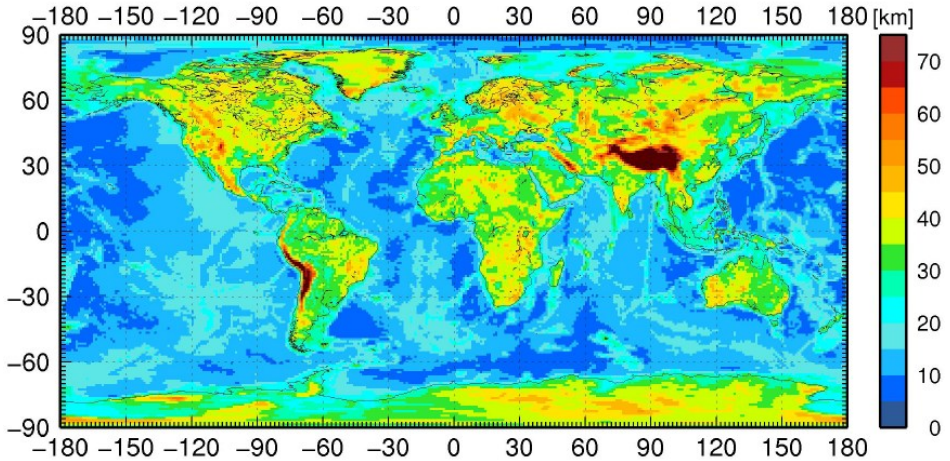

Fig. 3.4 Distributions of crustal thickness (without ice or water) in three global crustal models. CRUST 2.0: *Laske et al.* [2001]; CUB2.0: *Shapiro and Ritzwoller* [2002]; GEMMA: *Negretti et al.* [2012].

Table 3.3: Global average physical (density, thickness, mass and radiogenic heat power) and chemical (abundance and mass of HPEs) properties of each reservoir as described in the reference model. The BSE model is based on [*McDonough and Sun 1995*] and [*Arevalo et al. 2009*]. The physical structure of BSE above and beneath the Moho is based on this study and PREM, respectively. The uncertainty in density is about the same as that of Vp (3-4%) [*Mooney et al., 1998*]. We adopt a simple model for the mantle and do not report any uncertainties for its properties. [*Sramek et al. 2012*] review different mantle models and predict the consequences to the surface geoneutrino flux.

		ρ, g/cm^3	d, km	M, 10^{21} kg	Abundance			Mass			H, TW
					U, μg/g	Th, μg/g	K, %	U, 10^{15} kg	Th, 10^{15} kg	K, 10^{19} kg	
CC	Sed	2.25	1.5±0.3	0.7±0.1	1.73±0.09	8.10±0.59	1.83±0.12	$1.2^{+0.2}_{-0.2}$	$5.8^{+1.1}_{-1.1}$	$1.3^{+0.2}_{-0.2}$	$0.3^{+0.1}_{-0.1}$
	UC	2.76	11.6±1.3	6.7±0.8	2.7±0.6	10.5±1.0	2.32±0.19	$18.2^{+4.8}_{-4.3}$	$70.7^{+10.7}_{-10.2}$	$15.6^{+2.3}_{-2.1}$	$4.2^{+0.7}_{-0.6}$
	MC	2.88	11.4±1.3	6.9±0.9	$0.97^{+0.58}_{-0.36}$	$4.86^{+4.30}_{-2.25}$	$1.52^{+0.81}_{-0.52}$	$6.6^{+4.1}_{-2.5}$	$33.3^{+30.0}_{-15.5}$	$10.4^{+5.7}_{-3.7}$	$1.9^{+0.9}_{-0.6}$
	LC	3.05	10.0±1.2	6.3±0.7	$0.16^{+0.14}_{-0.07}$	$0.96^{+1.18}_{-0.51}$	$0.65^{+0.34}_{-0.22}$	$1.0^{+0.9}_{-0.4}$	$6.0^{+7.7}_{-3.3}$	$4.1^{+2.2}_{-1.4}$	$0.4^{+0.3}_{-0.1}$
	LM	3.37	140±71	97±47	$0.03^{+0.05}_{-0.02}$	$0.15^{+0.28}_{-0.10}$	$0.03^{+0.04}_{-0.02}$	$2.9^{+5.4}_{-2.0}$	$14.5^{+29.4}_{-9.4}$	$3.1^{+4.7}_{-1.8}$	$0.8^{+1.1}_{-0.6}$
OC	Sed	2.03	0.6±0.2	0.3±0.1	1.73±0.09	8.10±0.59	1.83±0.12	$0.6^{+0.2}_{-0.2}$	$2.8^{+0.9}_{-0.9}$	$0.6^{+0.2}_{-0.2}$	$0.2^{+0.1}_{-0.1}$
	C	2.88	7.4±2.6	6.3±2.2	0.07±0.02	0.21±0.06	0.07±0.02	$0.4^{+0.2}_{-0.2}$	$1.3^{+0.7}_{-0.5}$	$0.4^{+0.2}_{-0.2}$	$0.1^{+0.04}_{-0.03}$
DM		4.66	2090	3207	0.008	0.022	0.015	25.7	70.6	48.7	6.0
EM		5.39	710	704	0.034	0.162	0.041	24.0	113.7	28.7	6.3
BSE		4.42	2891	4035	0.020	0.079	0.028	80.7	318.8	113.0	20.1

3.2.2 Composition of the crust

Crust is an onliest reservoir which can be directly sampled. Its composition can be estimated better than of the other reservoirs.

Compositional estimates for some portions of the crust are adopted from previous work, whereas the composition of the deep continental crust is re-evaluated.

Sediments: The average composition of sediments and uncertainties are adopted from the GLOSS II model (GLObal Subducting Sediments) [*Plank, 2013*].

Oceanic Crust: An average oceanic crust composition is adopted from [*White and Klein 2013*] with a conservative uncertainty of 30%. The three seismically defined layers of basaltic oceanic crust reported by [Mooney et al. [1998] is treated as one reservoir.

Upper Continental Crust: The compositional model reported by [*Rudnick and Gao 2003*] for the upper continental crust and the uncertainties are adopted. Following [*Mooney et al. 1998*], the upper continental crust is defined seismically as the uppermost crystalline region in CRUST 2.0, having an average Vp of between 5.3 and 6.5 km s^{-1}.

Middle and Lower Crust: Composition of these layers was calculated following [*Huang et al. 2013*]. The correlation between seismic velocities and rock types was used for quantitative estimates of deep crustal composition and associated uncertainties. Middle and lower CC are assumed to be a binary mixture of felsic and mafic rocks.

Intermediate rocks, which have intermediate seismic velocities compared to those of felsic and mafic rocks, are not considered. As pointed out by [*Rudnick and Fountain 1995*], the very large range in velocities makes determination of their deep crustal abundances using seismic velocities impossible. It is assumed that a negligible amount of intermediate rocks is hidden in the deep crust. Since they have higher abundances of HPEs than mafic rocks and similar HPE contents to felsic rocks, ignoring their presence may lead to an underestimation of HPEs in the deep continental crust. Thus, estimates perfumed here should be regarded as minima.

At room temperature and 600 MPa pressure, amphibolite facies felsic rocks and mafic amphibolites, which represent felsic and mafic rocks in middle crust, have an average Vp of 6.34±0.16 km/s and Vp of 6.98±0.20 km/s (1-sigma) respectively. Granulite-facies felsic rocks and mafic granulites (felsic and mafic rocks in lower crust) have average Vp of 6.52±0.19 km/s and 7.21±0.20 km/s (see Table 3.4).

Because seismic velocities of rocks in the deep crust are strongly influenced by pressure and temperature, the laboratory-measured velocities for all rock groups (which were attained at

0.6 GPa and room temperature) were corrected to seismic velocities appropriate for pressure-temperature conditions in the deep crust. The pressure and temperature derivatives of 2×10^{-4} km s^{-1} MPa^{-1} and -4×10^{-4} km s^{-1} $^{o}C^{-1}$ were applied respectively [*Christensen and Mooney, 1995*; *Rudnick and Fountain, 1995*], and assume a typical conductive geotherm equivalent to a surface heat flow of 60 $mW \cdot m^{-2}$ [*Pollack and Chapman, 1977*]. Using the *in situ* Vp and Vs profiles for the middle (or lower) CC of each voxel given in CRUST 2.0, the fractions of felsic and mafic rocks were evaluated:

$$f + m = 1 \qquad \text{(Eq. 3.1)}$$

$$f \times v_f + m \times v_m = v_{crust} \qquad \text{(Eq. 3.2)}$$

where f and m are the mass fractions of felsic and mafic end members in the middle (or lower) CC; v_f, v_m and v_{crust} are Vp or Vs of the felsic and mafic end members (pressure- and temperature- corrected) and in the crustal layer, respectively. Only Vp is used to constrain the felsic fraction (f) in the middle or lower CC for three main reasons: using Vs gives results for (f) in the deep crust that are in good agreement with those derived from the Vp data, the larger overlap of Vs distributions for the felsic and mafic end-members in the deep crust limits its usefulness in distinguishing the two end-members [*Huang et al. 2012*], and Vs data in the crust are deduced directly from measured Vp data in CRUST 2.0.

The distributions of the HPE abundances in felsic and mafic amphibolite and granulite facies rocks are taken from compilation of [*Huang et al. 2012*] and presented in Table 3.4 with associated 1 σ uncertainties. These values were calculated on the basis of compositional databases of representative rocks. The abundances have asymmetrical uncertainties due to log-normal distribution of the applied fit.

Table 3.4. Average laboratory-measured Vp (600 MPa, room temperature) and HPE abundances in amphibolite facies, granulite facies and peridotite rocks with 1σ uncertainty.

Rock type		Vp, km/s	K_2O, wt.%	Th, μg/g	U, μg/g
Amphibolite Facies (MC)	Felsic	6.34±0.16	$2.89^{+1.81}_{-1.11}$	$8.27^{+8.12}_{-4.10}$	$1.37^{+1.03}_{-0.59}$
	Mafic	6.98±0.20	$0.50^{+0.41}_{-0.23}$	$0.58^{+0.57}_{-0.29}$	$0.37^{+0.39}_{-0.19}$
Granulite Facies (LC)	Felsic	6.52±0.19	$2.71^{+2.05}_{-1.17}$	$3.87^{+7.53}_{-2.54}$	$0.42^{+0.41}_{-0.21}$
	Mafic	7.21±0.20	$0.39^{+0.31}_{-0.17}$	$0.30^{+0.46}_{-0.18}$	$0.10^{+0.14}_{-0.06}$

3.2.3 Calculation of amount of HPE and geoneutrino signal from the crust

Calculated amount of HPEs (Table 3.3), which determines the radiogenic heat power and geoneutrino signal is based on the physical (density and thickness) and chemical (abundance of HPEs) characteristics of each crustal layer in the reference model. For the middle and lower CC, Vp and composition of amphibolite and granulite facies rocks were used to determine the average abundance of HPEs, as it was discussed:

$$a = f \times a_f + m \times a_m \qquad \text{(Eq. 3.3)}$$

where a_f and a_m is the abundance of HPEs in the felsic and mafic end member, respectively; a is the average abundance in the reservoir. Equations 3.1 and 3.2 define the mass fractions of felsic and mafic end members (f and m) in the MC and LC reservoirs. In the rare circumstance when the calculated average abundance is more (or less) than the felsic (or mafic) end member, it is assumes that the average abundance should be the same as the felsic (or mafic) end member. The calculated radiogenic heat power is a direct function of the masses of HPEs and their heat production rates: 9.85×10^{-5}, 2.63×10^{-5} and 3.33×10^{-9} W/kg for U, Th and K, respectively [*Dye, 2012*].

The distribution of HPEs in these different reservoirs affects the geoneutrino flux on the Earth's surface. Summing the antineutrino flux produced by HPEs in each volume of the model, the geoneutrino unoscillated flux $\Phi^{(\text{unosc.})}$ expected in Gran Sasso area can be calculated. The flux from U and Th arriving at detectors is smaller than that produced, due to neutrino oscillations, $\Phi^{(\text{osc.})}_{\text{U, Th}} = \langle \text{Pee} \rangle \, \Phi^{(\text{unosc.})}_{\text{U, Th}}$, where $\langle \text{Pee} \rangle = 0.55$ is the average survival probability [*Fiorentini et al., 2012*]. The geoneutrino event rate in a liquid scintillator detector depends on the number of free protons in the detector, the detection efficiency, the cross section of the inverse beta reaction, and the differential flux of antineutrinos from ^{238}U and ^{232}Th decay arriving at the detector. Taking into account the U and Th distribution in the Earth, energy distribution of antineutrinos [*Fiorentini et al., 2010*], the cross section of inverse beta reaction [*Bemporad et al., 2002*], and mass-mixing oscillation parameters [*Fogli et al., 2011*], the geoneutrino event rate from the decay chain of ^{238}U and ^{232}Th at the site of Borexino detector was computed (Table 3.5). For simplicity, the finite energy resolution of the detector is neglected, and 100% detection efficiency is assumed. The expected signal is expressed in TNU.

Table 3.5. Geoneutrino signal at the site of Borexino detector from each reservoir as described in the reference Earth model. The unit of signal is TNU as defined in Section 3.1. The reported uncertainties are 1 σ. ROC is defined as Rest of Crust with the geoneutrino signal originated from the 24 closest 1°×1° crustal voxels excluded from the total crustal signal (see Section 3.3).

	Borexino 42.45 N, 13.57 E		
	S(U)	S(Th)	S(U+Th)
Sed_CC	$1.3^{+0.3}_{-0.3}$	$0.4^{+0.09}_{-0.09}$	$1.8^{+0.3}_{-0.3}$
UC	$13.7^{+3.6}_{-3.4}$	$3.7^{+0.6}_{-0.5}$	$17.5^{+3.6}_{-3.4}$
MC	$4.7^{+3.3}_{-1.8}$	$1.8^{+1.7}_{-0.9}$	$7.0^{+3.9}_{-2.5}$
LC	$1.0^{+0.8}_{-0.4}$	$0.5^{+0.9}_{-0.3}$	$1.7^{+1.3}_{-0.7}$
CLM	$1.4^{+2.7}_{-1.0}$	$0.4^{+1.0}_{-0.3}$	$2.2^{+3.1}_{-1.3}$
Sed_OC	$0.2^{+0.06}_{-0.05}$	$0.06^{+0.02}_{-0.02}$	$0.2^{+0.1}_{-0.1}$
OC	$0.05^{+0.02}_{-0.02}$	$0.01^{+0.005}_{-0.004}$	$0.06^{+0.02}_{-0.02}$
Bulk Crust	$21.4^{+5.2}_{-4.6}$	$6.8^{+2.3}_{-1.4}$	$29.0^{+6.0}_{-5.0}$
ROC	$10.3^{+2.6}_{-2.2}$	$3.2^{+1.1}_{-0.7}$	$13.7^{+2.8}_{-2.3}$
Total LS	$23.6^{+6.8}_{-5.2}$	$7.6^{+2.9}_{-1.8}$	$31.9^{+7.3}_{-5.8}$
DM	4.1	0.8	4.9
EM	2.7	0.8	3.5
Grand Total	$40.2^{+7.3}_{-5.8}$		--

3.2.4 Estimation of uncertainties

Estimation of the uncertainties in the reference model is not straightforward. The commonly used quadratic error propagation method [*Bevington and Robinson, 2003*] is only applicable for linear combinations (addition and subtraction) of errors of normally distributed variables. For non-linear combinations (such as multiplication and division) of uncertainties, the equation provides an approximation when dealing with small uncertainties, and it is derived from the first-order Taylor series expansion applied to the output. Moreover, the error propagation equation cannot be applied when combining asymmetric uncertainties (non-normal distributions). Because of this, the most common procedure for combining asymmetric uncertainties is separately tracking the negative error and the positive error using the error propagation equation. This method has no statistical justification and may yield the wrong approximation.

To trace the error propagation in the reference model, MATLAB was used to perform a Monte Carlo simulation [*Huang et al., 2012*; *Robert and Casella, 2004*; *Rubinstein and Kroese, 2008*]. Monte Carlo simulation is suitable for detailed assessment of uncertainty, particularly when dealing with larger uncertainties, non-normal distributions, and/or complex algorithms. The only requirement for performing Monte Carlo simulation is that the probability functions of all input variables (for example, the abundance of HPEs, seismic velocity, thickness of each layer in the reference model) are determined either from statistical analysis or empirical assumption. Monte Carlo analysis can be performed for any possible shape probability functions, as well as varying degrees of correlation. The Monte Carlo approach consists of three clearly defined steps using MATLAB. The first step is generating large matrices with pseudorandom samples of input variables according to the specified individual probability functions (Here 10^5 random numbers were enough to achieve stable result after series of iterations). Then the output variable (such as mass of HPEs, radiogenic heat power and geoneutrino flux) is calculated from the matrixes that are generated following the specified algorithms function. The final step is to do statistical analysis of the calculated matrix for the output variable (evaluation of the distribution, central value and uncertainty).

3.2.5. Discussion

Physical and Chemical Structure of the Reference Crustal Model

The thickness of the reference crustal model is obtained by averaging the three geophysical global crustal models obtained from different approaches, as described in Section 3.2.1. The distributions of crustal thickness and associated relative uncertainty in the model are shown in Figs. 3.5a and 3.5b, respectively. The uncertainties of the continental crustal thickness are not homogeneous: platform, Archean and Proterozoic shields, the main crustal types composing the interior of stable continents and covering ~50% surface area of the whole CC, have thickness uncertainties rarely exceeding 10%, while the thickness of continental margin crust is more elusive. Larger uncertainties for the thickness estimates occur in the OC, especially for the mid ocean ridges (Fig. 3.5b). The average crustal thicknesses (including the bulk CC, bulk OC and different continental crustal types) and masses of the reference model are compared with the three geophysical models. The global average thicknesses of platforms, Archean and Proterozoic shields are all previously estimated to be 40-43 km [*Christensen and Mooney, 1995*; *Rudnick and Fountain, 1995*]. Although GEMMA yields the thinnest thicknesses for shields and platforms, considering that the typical uncertainty in estimating global average CC thickness is more than 10% [*Čadek and Martinec*, 1991], the reference model, as well as the other three crustal models, fall within uncertainty of estimates by [*Christensen and Mooney 1995*] at the 1-sigma level. Extended crust and orogens in the three input models and in the average model show average thicknesses higher than, but within 1 σ of the estimations made by [*Christensen and Mooney 1995*]. The surface area weighted average thicknesses of bulk CC for the three input models and our reference model are smaller than the ~41 km estimated by [*Christensen and Mooney 1995*], likely due to the fact that they did not include continental margins, submerged continental platforms and other thinner crustal types in their compilation. The thickness of OC is generally about 7-8 km, with the exception of the GEMMA model, which yields 8.8 km thick average OC. The possible reason for the thick OC in GEMMA is due to the poorly global density distribution under the oceans. However, considering that the average uncertainty in determining the crustal thickness in the oceans is about 2-3 km [*Čadek and Martinec, 1991*], the three input models yield comparable results.

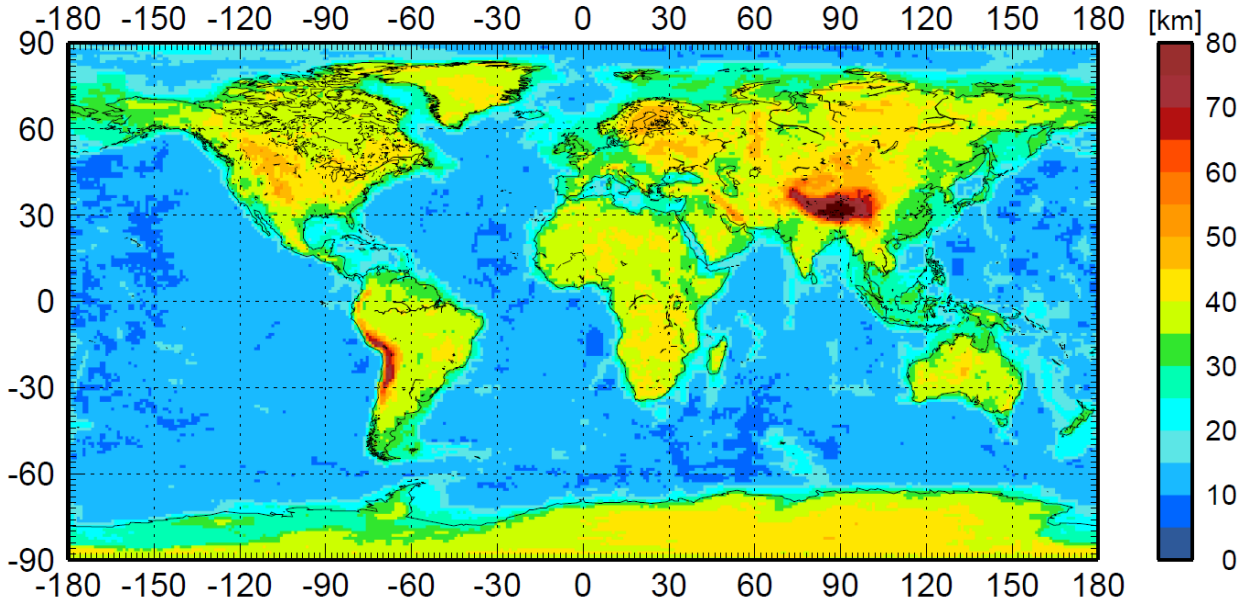

(a)

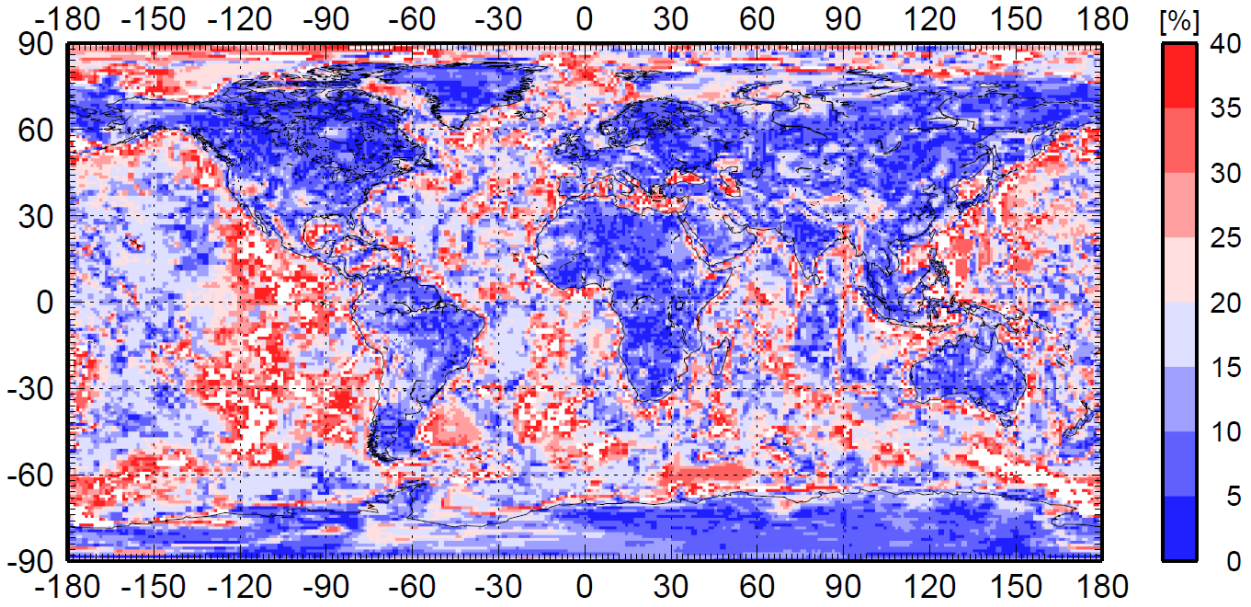

(b)

Fig.3.5: Thickness of crust (a) and its relative uncertainty (b) of the reference model.

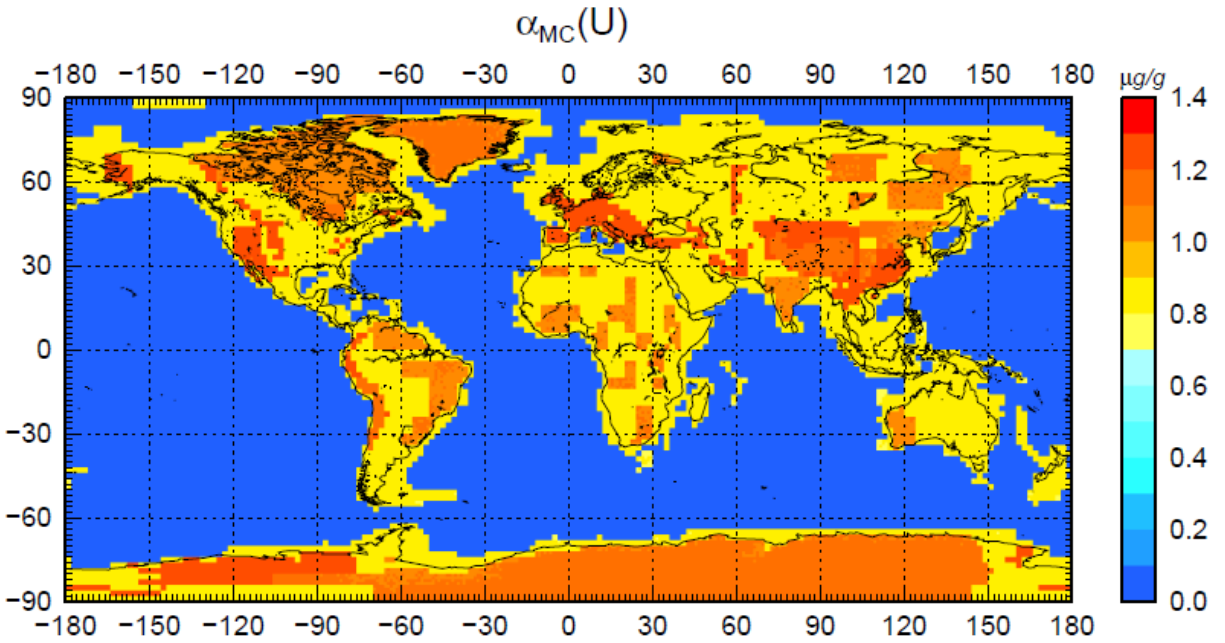

(a)

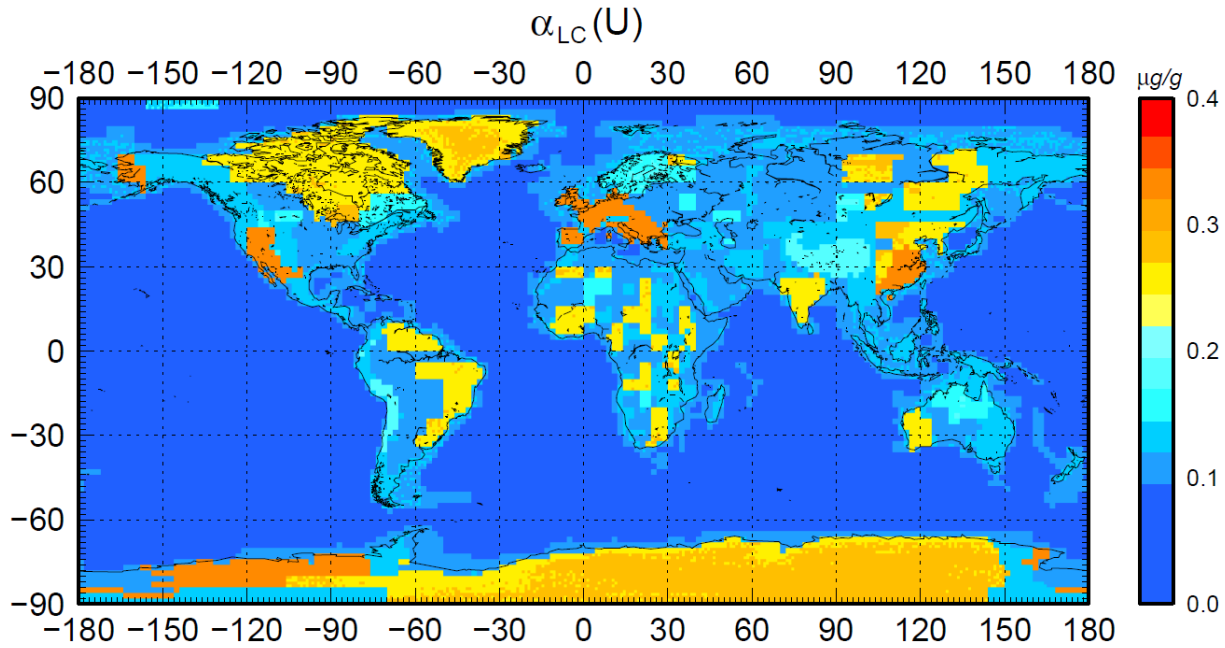

(b)

Fig. 3.6. The abundance of U in the middle (a) and lower (b) CC obtained by using seismic velocity argument.

As shown in Fig. 3.6 the middle and lower CC of the reference model are compositionally heterogeneous on a global scale. The average middle CC derived here has $0.97^{+0.58}_{-0.36}$ μg/g U, $4.86^{+4.30}_{-2.25}$ μg/g Th and $1.52^{+0.81}_{-0.52}$ wt.% K, while the average abundances of U, Th and K in the lower CC are $0.16^{+0.14}_{-0.07}$ μg/g, $0.96^{+1.18}_{-0.51}$ μg/g and $0.65^{+0.34}_{-0.22}$ wt.%, respectively (Table 3.6; Fig. 3.6). The uncertainties reported for the new estimates of the HPE abundances in the deep crust are significantly larger than reported in previous global crustal geochemical models [e.g., *Rudnick and Fountain, 1995*; *Rudnick and Gao, 2003*], due to the large dispersions of HPE abundances in amphibolite and granulite facies rocks.

Because of these large uncertainties, all of the estimates for HPEs in the deep crust of the reference model agree with most previous studies at the 1 σ level (Table 3.6). For the middle CC, the central values of estimates for HPEs are generally only ~10% to 30% lower than those made by [*Rudnick and Fountain 1995*] and [*Rudnick and Gao 2003*]. For the lower CC, the difference in HPEs between this model and several previous studies is significantly larger than that of the middle CC. The reference model has lower U and Th, but higher K concentrations, agreeing at the 1 σ level, than the previous estimates of the lower CC by [*Rudnick and Fountain 1995*] and [*Rudnick and Gao 2003*]. Taylor and McLennan [*Taylor and McLennan 1995*], McLennan [*McLennan 2001*], Wedepohl [*Wedepohl 1995*] and Hacker et al. [*Hacker et al. 2011*] constructed two-layer crustal models with the top layer being average upper CC (from either their own studies, or [*Rudnick and Gao 2003*] in the case of [*Hacker et al. 2011*]) and the bottom layer equal to the average of the middle and lower CC in the reference model presented here (see Fig. 3 in [*Hacker et al. 2011*]). The abundances of U, Th and K in the combined middle and lower CC of this model are $0.60^{+0.32}_{-0.20}$ μg/g, $3.22^{+2.35}_{-1.35}$ μg/g, and $1.14^{+0.45}_{-0.32}$ wt.%, respectively, which agrees within 1 σ uncertainty of the estimates of [*Hacker et al. 2011*] and within uncertainty of the Th and U abundances of [*McLennan 2001*] and of K abundance of [*Wedepohl 1995*], but are significantly higher than the abundance estimates of [*Taylor and McLennan 1995*] for all elements, and the K abundance estimate of [*McLennan 2001*], while lower than the Th and U abundances of [*Wedepohl, 1995*]. Similarly, for the bulk CC, estimates of HPE abundances presented here are close to those determined by [*Rudnick and Fountain 1995*], and [*Rudnick and Gao 2003*]. Obtained results also agree with those of [*Hacker et al. 2011*], though their Th concentration is at the 1 σ upper bound of our model. By contrast, the reference model has significantly higher concentrations of HPEs, beyond the 1 σ level, than estimates by [*McLennan 2001*] and [*Taylor and McLennan 1995*], and lower than estimates by [*Wedepohl 1995*]. The masses of U, Th and K concentrated in the bulk CC of the reference model are about 33%, 37%

and 28%, respectively, of their total amount in the BSE [*McDonough and Sun, 1995*]. The estimates of the K/U ($11,656^{+3,512}_{-2,516}$) and Th/U ($4.4^{+1.6}_{-1.0}$) in the bulk CC agree with all previous studies at the 1-σ level, due to the large uncertainties associated these two ratios derived from large uncertainties of HPE abundance in the CC.

Geoneutrino Flux and Radiogenic Heat Power

In the past decade different authors have presented models for geoneutrino production from the crust, and associated uncertainties. Mantovani et al. [*Mantovani et al., 2004*] adopted minimal and maximal HPE abundances in the literature for each crustal layer of CRUST 2.0 in order to obtain a range of acceptable geoneutrino fluxes. Based on the same geophysical crustal model, Fogli et al. [*Fogli et al.,2006*] and Dye [*Dye, 2010*] estimated the uncertainties of fluxes based on uncertainties of the HPE abundances reported by [*Rudnick and Gao, 2003*].

Fig. 3.7 shows the map of geoneutrino signal at Earth's surface. The reference model was built to estimate the 1 σ uncertainties of geoneutrino fluxes and radiogenic heat power taking into account two main sources of uncertainties: the physical structure (geophysical uncertainty) and the abundances of HPEs in the reservoirs (geochemical uncertainty). This approach allowed to evaluate the geophysical and geochemical contributions to the uncertainties of the model, particularly for the lithosphere. With respect to the previous estimates the asymmetrical distribution of the uncertainties as a consequence of the non-Gaussian distributions of HPE abundances in the deep CC and CLM was pointed out. Within 1 σ uncertainties, obtained results for U and Th geoneutrino signal from the crust predicted for Borexino detector (Table 3.5) is comparable to that reported by [*Mantovani et al., 2004*] and [*Dye, 2010*], for which symmetrical and homogeneous uncertainties were adopted. Reported in Table 3.5 asymmetrical 1 σ uncertainties of the geoneutrino signal are a consequence of the detailed characterization of the crustal structure and its radioactivity content.

The different contributions from geophysical and geochemical uncertainties to the 1-σ uncertainties of total crustal geoneutrino signals were studied. In the developed reference model the total predicted signal for Borexino is $29.0^{+6.0}_{-5.0}$ TNU. Fixing the HPE abundances in all crustal reservoirs constant at their central values, uncertainties associated with the geophysical model contribute ±2.7 TNU to the total uncertainties of the crustal geoneutrino signal at Borexino. By fixing the crustal thickness of all voxels constant, the geochemical uncertainties contribute $^{+5.0}_{-4.3}$

TNU to the total uncertainties crustal geoneutrino signal at Borexino. The geochemical uncertainties clearly dominate the total uncertainty of the crustal geoneutrino signals.

Precise estimation of crustal contribution to the total geoneutrino signal together with experimental measurement of the signal would provide constraints on permissible BSE compositional models [*Dye*, 2010; *Fiorentini et al.*, 2012; *Sramek et al.*, 2012]. In particular, by subtracting the predicted crustal signal (S_{crust}) from the experimental total rates ($S_{tot,\ exp}$), it is expected to infer the mantle contributions (S_{mantle}). Furthermore, refined model of the crustal structure in the region close to the detector gives the uncertainty of the signal from LOcal Crust (S_{LOC}, see next section 3.3), which reduce the uncertainty of global crustal signal [*Coltorti et al., 2011*]. Since S_{crust} in this study is the sum of S_{LOC} and S_{ROC} (the signal from the Rest Of the Crust after excluding local crust), Table3.5 reports the geoneutrino signal S_{ROC} (expected from Rest Of Crust + CLM) on the base of the reference model of all crust. In the next future all these calculations and experimental measurements of geoneutrino flux at different sites on the Earth surface can be used for extracting the mantle geoneutrino signals, following this equation:

$$S_{mantle} = S_{tot,\ exp} - S_{ROC} - S_{LOC}.$$

The CC in the reference model contributes $7.0^{+1.4}_{-1.1}$ TW radiogenic heat power to the total 20.1 TW radiogenic power generated in the considered BSE, which agrees with previous estimates by Hacker et al. [*Hacker et al., 2011*], Rudnick and Fountain [*Rudnick and Fountain,1995*], and Rudnick and Gao [*Rudnick and Gao, 2003*] and at the 1 σ level, but is higher than estimates by McLennan [*McLennan, 2001*] and Taylor and McLennan [*Taylor and McLennan, 1995*], and lower than estimate by Wedepohl [*Wedepohl, 1995*] (Table 3.6). The geophysical and geochemical contribution of to the total uncertainties of radiogenic heat power were estimated, they are: ±0.8 TW and $^{+1.1}_{-0.8}$ TW at 1-σ respectively.

Although the mass of OC (excluding the overlying sediment) is poorly known, its contribution to the anticipated geoneutrino signals is less than 0.2 TNU at the 1-σ level.

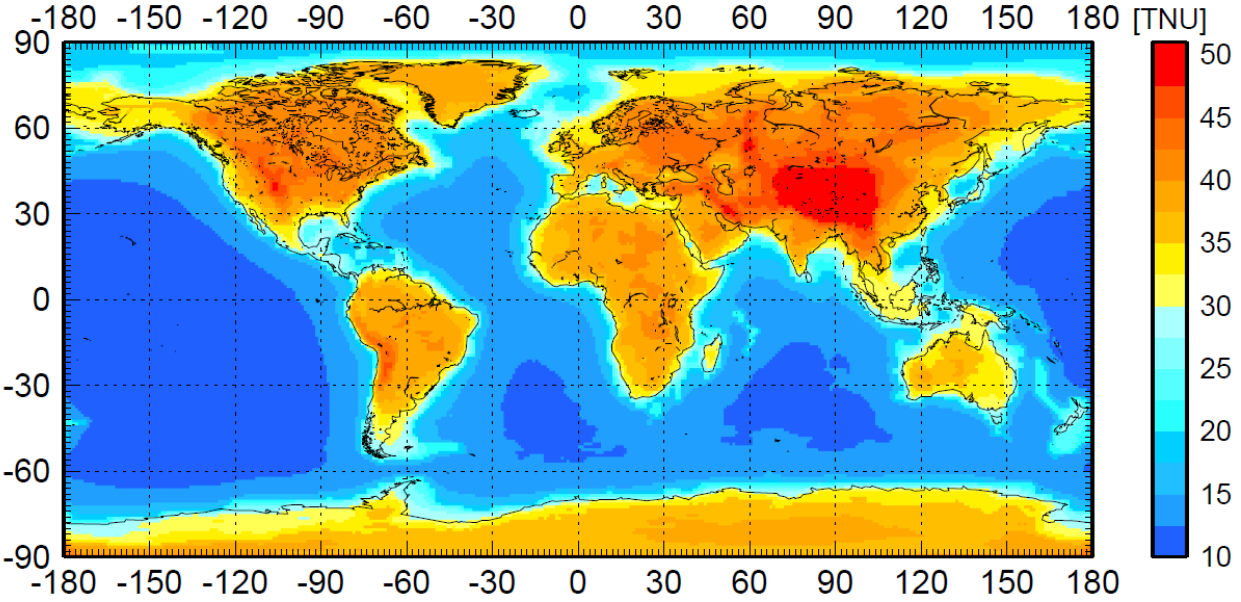

Fig. 3.7. Geoneutrino signal at Earth's surface. The unit is TNU.

Table 3.6. Estimates of the K, Th and U concentrations and radiogenic heat power (P) in the continental crust. K, Th and U concentrations are listed as wt. %, μg/g, and μg/g, respectively, P in TW (10^{12} W). Keys to models: TM [*Taylor and McLennan, 1995*]; M [*McLennan, 2001*]; W [*Wedepohl, 1995*]; H [*Hacker et al., 2011*]; RF [*Rudnick and Fountain, 1995*]; RG [*Rudnick and Gao, 2003*]. Radiogenic heat power is calculated from the bulk CC assuming it has a mass of 20.6×10^{21} kg as developed here reference model.

		TM	M	W	H	RF	RG	**RM**
Upper Crust	K	2.8	2.8	2.87	2.32	2.8	2.32±0.19	2.32±0.19
	Th	10.7	10.7	10.3	10.5	10.7	10.5±1.0	10.5±1.0
	U	2.8	2.8	2.5	2.7	2.8	2.7±0.6	2.7±0.6
Middle Crust	K	-	-	-	-	1.67	1.91	$1.52^{+0.81}_{-0.52}$
	Th	-	-	-	-	6.1	6.5	$4.86^{+4.30}_{-2.25}$
	U	-	-	-	-	1.6	1.3	$0.97^{+0.58}_{-0.36}$
Lower Crust	K	0.28	0.53	1.31	1.24	0.50	0.50	$0.65^{+0.34}_{-0.22}$
	Th	1.06	2.0	6.6	5.6	1.2	1.2	$0.96^{+1.18}_{-0.51}$
	U	0.28	0.53	0.93	0.7	0.2	0.2	$0.16^{+0.14}_{-0.07}$
Bulk CC	P	5.6	6.3	8.5	7.9	7.7	7.4	$6.8^{1.4}_{-1.1}$

3.3 Local model of the crust

The major contribution to geo-neutrino signal comes from the region close to the detector due to its proximity. For KamLAND and Borexino, Mantovani et al. [*Mantovani et al., 2004*] estimated that about one half of the signal originates from an area surrounding the detector within a radius of 400 km and 800 km, respectively (Fig. 3.8). This region, although containing a globally negligible amount of U and Th, produces a large contribution to the signal as a consequence of its proximity to the detector.

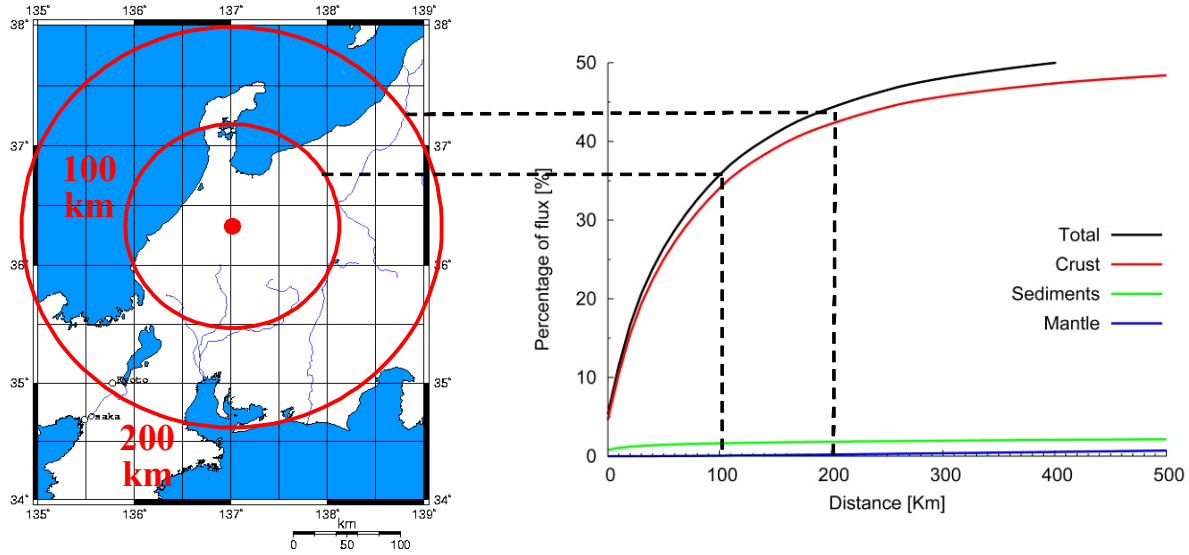

(a)

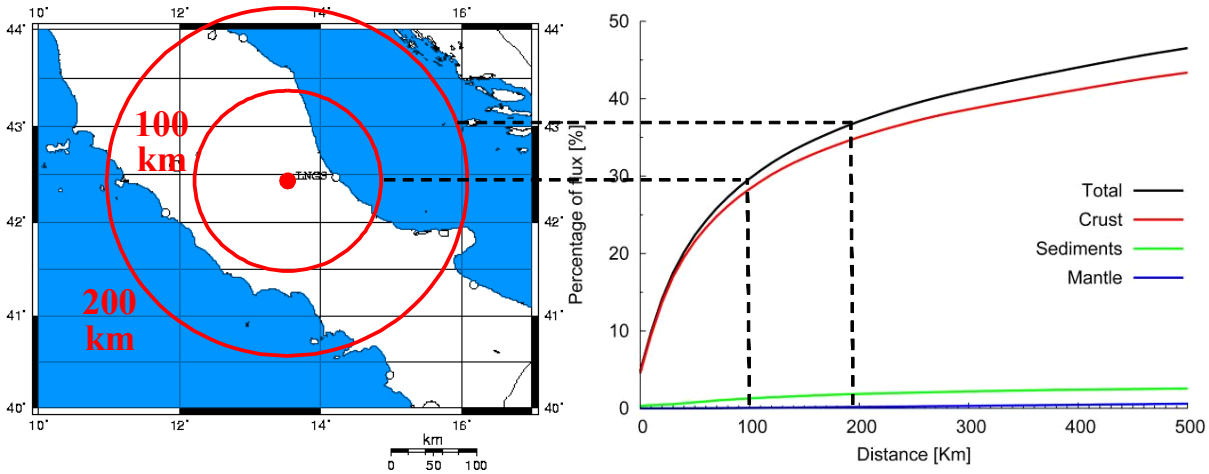

(b)

Fig. 3.8 (a) 50% of the total geo-neutrino signal in Borexino originates within 900 km around detector; (b) 50% of the total geo-neutrino signal in KamLAND originates within 600 km around detector.

Current reference models [*Mantovani et al., 2004, Fogli et al. 2005, Enomoto 2007, Dye 2010*] for the Earth's crust use the map of [*Bassin et al. 2000*] divided into 2° x 2° horizontally homogeneous tiles, which is clearly a very rough approximation for describing the region surrounding the detector. Moreover, worldwide averages for the chemical composition of different regions of the Earth (e.g., upper crust, lower crust, and mantle) are used to estimate U and Th concentrations. However, if one wants to extract from the total signal relevant information on the deep Earth, the regional/local contribution needs to be determined on the grounds of a more detailed geological, geochemical and geophysical study of the region. The reasonable refinement of the model supposes that the local contribution to the geo-neutrino signal needs to be determined with an accuracy that is comparable to the uncertainties from the contributions of the rest of the Earth.

This highlights the need for a detailed study for the region around detector, which improves the accuracy of the reference model. Such a study was performed in [*Fiorentini et al., 2005; Enomoto et al., 2007*] for Kamioka; a refined reference model for Gran Sasso is presented in this chapter.

According to the reference model [*Mantovani et al. 2004*] the total predicted geo-neutrino signal at Gran Sasso area is 40.5 TNU. The last column of Table 3.7 shows the contributions of the different reservoirs to the signal in this model. The mantle contributes 9 TNU, about 20% of the total signal, while crust and sediments all over the world provide the rest of the contribution (31.5 TNU). Half of this originates from the six tiles depicted in Fig. 3.9 which provide a "local contribution":

$$S_{reg} = 15.3 \text{ TNU}$$

Within this region, the 2° x 2° Central Tile, indicated as CT in Fig. 3.9, generates a "local contribution" of:

$$S_{CT} = 11.8 \text{ TNU}$$

Geological units and structures, which present in the detector area, might be washed out in the 2°×2° crustal map. To improve the knowledge of this region a three dimensional (3D) geological model of the 2° x 2° area around Gran Sasso was build. It is based on the results of a deep seismic exploration of the Mediterranean and Italy (the CROP project) [*Finetti, 2005a*], as well as geological and stratigraphical distribution of the sedimentary covers (SC) recognizable from geological maps, integrated with data from deep oil and gas wells. The main feature of this area is a thick sedimentary cover, which was not adequately accounted for in the averages leading to the 2° x 2° crustal map

Table 3.7. The contribution of the different reservoirs and areas to the geo-neutrino signal at Gran Sasso, in TNU units, according to the reference model of [*Mantovani et al. 2004*] and to the local study presented in this chapter. Results are presented for the approximate detector position (42° N, 14° E) used in [*Mantovani et al. 2004*] and for the more precise value (42° 27' N, 13° 34' E) found in [*Bellotti 1988*].

Detector Latitude and Longitude		42° 27' N 13° 34' E			42° 27' N 13° 34' E	42° N 14° E
Area and reservoir		Local Study			[*Mantovani et al. 2004*]	
		S(U)	S(Th)	S(U+Th)	S(U+Th)	S(U+Th)
a) Local contribution						
Central Tile (CT)	Sediments	2.33	0.37	2.70	0.53	1.75
	UC	3.76	0.92	4.68	7.59	6.25
	MC	-	-	-	3.09	2.77
	LC	0.22	0.16	0.38	1.08	0.98
Rest of the local area	Sediments	0.29	0.05	0.34	0.29	0.32
	UC	1.35	0.33	1.68	1.52	1.56
	MC	-	-	-	1.02	1.12
	LC	0.14	0.10	0.24	0.47	0.51
Local contribution, total		*8.09*	*1.93*	*10.02*	*15.59*	*15.26*
b) Rest of the crust, total		-	-	-	*16.42*	*16.25*
c) Mantle		-	-	-	*9.0*	*9.0*
d) Earth, total		-	-	-	41.0	40.5

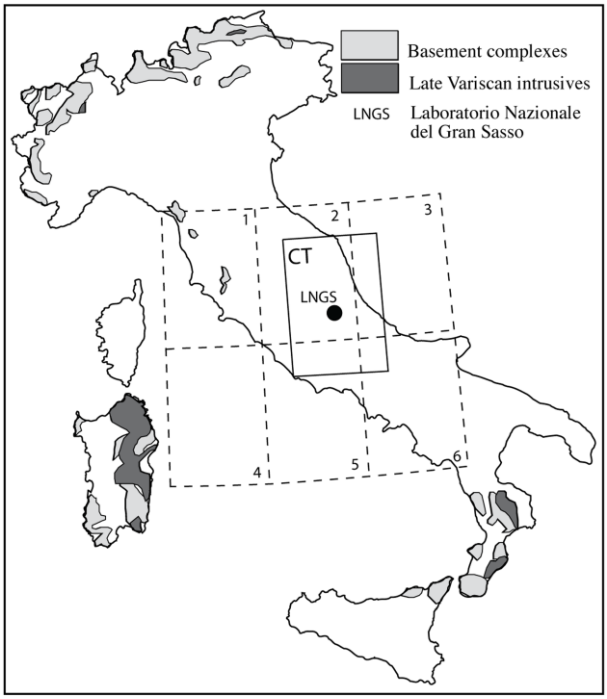

Fig. 3.9 – Schematic map of the main area where basement complexes and Late Variscan intrusive bodies outcrop in Italy (modified after [*Boriani et al., 2003*]). The central tile (CT) of the 2°x2° centred at the Gran Sasso laboratory (LNGS) and the six tiles which provide the "local contribution" to the geoneutrino flux are also reported.

In addition, regional differences in the geochemical composition (abundances of radioactive elements) of different reservoirs compared to the world averages need to be evaluated. To check that these global averages are appropriate for the Gran Sasso region, representative samples of the sediments and upper and lower crustal lithologies in Northern Italy (Ivrea-Verbano zone and Valsugana) were analysed.

For the rest of the region – i.e., what remains of the six tiles after subtracting the central tile (Fig. 3.9), a less detailed study was performed.

Before closing this section, it is useful to take into account the position of the LNGS, in [*Mantovani et al. 2004*] it was rounded to 42° N, 13° E. This approximation was adequately given the tile size of the 2°x2° crustal map used in that reference model. For this study, a better precision is required. In fact, the geographical position of the underground laboratory is 42° 27' N and 13° 34' E of Greenwich, see [*Bellotti 1988*]; this more precise position is adopted here. Note that by changing the position to this value, holding all other parameters constant, the predicted signal increases by 0.5 TNU, i.e. about 1%, (Table 3.7).

3.3.1. Sampling and analytical methods

In order to measure abundance of U and Th in Gran Sasso area, an accurate sampling was carried out. The sedimentary rocks were sampled a distance of 20 km of LNGS. Due to the lack of UC and LC material around the studied area and assuming rock abundances and composition of the south Alpine basement fairly homogeneous for the whole Adriatic microplate, a detailed sampling was carried out through the LC-UC section of Ivrea-Verbano Zone from granulitic rocks of Val Strona, Val Sessera and Val Sesia [*Hunziker and Zingg, 1980*; *De Marchi et al., 1998*; *Quick et al., 1992; 2003*] to amphibolitic schists of Serie dei Laghi and related intrusives [*Boriani et al., 1990*; *Franz and Romer, 2007*]. To complete the UC section, the low grade metamorphic philladic rocks outcropping in Valsugana, and related intrusive rocks of Caoria and Cima d'Asta complexes [*Dal Piaz and Martin, 1998*; *D'Amico et al., 1971*; *Sassi et al., 2004*] were also sampled.

Taking into account the thickness of the sedimentary cover around Gran Sasso area it was considered as separate reservoir from Upper Crust. On the contrary, due to the geological and geophysical difficulties of precisely define the intermediate layer introduced by [*Rudnick and Fountain 1995*] the crust was subdivided in only two layers, namely the Lower Crust and the Upper Crust, as also proposed by [*Wedephol 1995*].

Summarizing for the sedimentary successions 28 samples, 14 within 20 km and 14 within 200 Km from the LNGS were collected. 29 metamorphic and intrusive samples were collected in Valsugana and Ivrea-Verbano-Laghi areas, with particular emphasis to felsic rocks of the UC due to their high content in radionuclides [*Colotorti et al. 2011*].

3.3.2 U and Th abundances in the central tile

The Upper Crust (UC) can be defined as the portion of continental crust ranging from the bottom of the sedimentary cover to the Conrad discontinuity, which marks the top of the Lower Crust. This approach, which is mainly based on geophysical data, shows some problems when trying to define the position of the medium-grade, amphibolite facies rocks. Indeed, Rudnick and Fountain [*Rudnick and Fountain, 1995*] introduced a Middle Crust mainly composed by migmatitic rocks, whereas Wedepohl [*Wedepohl, 1995*] includes the amphibolites within the UC. The geophysical profiles beneath Central Italy do not support the existence of a well defined intermediate level, while the limited thickness of the LC induced to insert the amphibolitic rocks within the UC.

Sedimentary cover

It shall be assumed that sediments formed in similar depositional environments would have similar and rather homogeneous chemical characteristics, thus linking geochemistry to lithofacies. In this respect the approach is similar to that proposed by [*Plank and Langmuir, 1998*], allowing to reduce the number of samples to be analysed but preserving at the same time the geological meaningful information. They estimate that even a reduced number of samples can bring to an error in the geochemical estimates <30%, which considering the aim of this work and the large variety of sediments is a favourable result.

For the purpose of this work the Cenozoic terrigenous and the terrigenous/carbonatic Permo-Mesozoic succession has been divided in four reservoirs:

a) Cenozoic terrigenous units (sandstones, siltites and clays)

b1) Meso-Cenozoic basinal carbonate units (marly and shaly carbonates, sometimes with black shales)

b2) Mesozoic Carbonate Units (limestones, dolomites and evaporites, with a negligible marl and clay content)

b3) Permian clastic units (sandstones and conglomerates)

U and Th mass abundances in the three reservoirs are obtained by arithmetical averages of the measured samples. Lithotypes belonging to the last reservoir (b3) outcrop rarely within the entire Italian Peninsula and due to their conglomeratic nature, sampling is quite difficult to be carried out. For these reasons and taking into account that the Permian clastic units ("Verrucano" Fm.) result from the dismantling and erosion of the Paleozoic basement rocks, U and Th contents of reservoir b3 assumed to be similar to those of the UC.

In each reservoir, the dispersion of the measured abundances is much larger than the analytical uncertainty and also the uncertainties on the mass of the reservoirs are negligible respect to them. Taking into account the relative volume (Table 3.8) of the four reservoirs estimated on the base of the 3D geological model (see below) the abundances of U and Th for the whole sedimentary cover can be determined (Table 3.9).

TABLE 3.8 – Volume (in km^3 and %) and thickness (in km) of the four sedimentary reservoirs and of the UC and LC. Thickness are reported according to the local model and the CRUST 2.0 model, [*Bassin et al., 2000*].

	Volume (km^3)	Volume (%)	Thickness (km)	
			CRUST 2.0	This study
a) Cenozoic terrigenous sediments	83,589	6.8	0.5	13
b1) Meso-Cenozoic Basinal Carbonates	9,028	0.7		
b2) Mesozoic Carbonates	345,684	28.1		
b3) Permian clastic units	25,163	2.0		
Upper crust	468,772	38.0	10	13
Middle crust	/	/	10	/
Lower crust	300,566	24.4	10.5	9
Total	**1,232,802**	**100**	**31**	**35**

Table 3.9. Calculated U and Th abundances for the whole sedimentary cover (SC) of the Central Tile. Approximate average densities are from [*Telford et al., 1990*] and are in agreement with the densities assumed by [*Laske et al., 2001*] for the rest of the world.

Reservoir		Density [g/cm^3]	Volume [%]	Mass [%]	*a*(U) [ppm]	*a*(Th) [ppm]
a) Cenozoic terrigenous sediments		2.1	18.0	15.6	2.3 ± 0.2	8.3 ± 0.8
b) Permo-Mesozoic carbonatic succession	b1) Meso-Cenozoic Basinal Carbonates	2.3	2.0	1.8	1.7 ± 0.9	1.5 ± 0.5
	b2) Mesozoic Carbonates	2.5	74.6	76.8	0.3 ± 0.1	0.2 ± 0.1
	b3) Permian clastic units	2.6	5.4	5.8	2.2 ± 0.4	8.1 ± 1.6
Mass weighted averages					0.8 ± 0.1	2.0 ± 0.2
[*Plank and Langmuir, 1998*]					1.7	6.9

The largest area in the Gran Sasso region is occupied by U- and Th-poor Mesozoic carbonates. The mass weighted average concentrations are U = 0.8 ppm and Th = 2.0 ppm, which are significantly lower than the world average for sediments adopted in the previous reference models, U = 1.7 and Th = 6.9 ppm [*Plank and Langmuir, 1998*]. This is a consequence of the large fraction of carbonates in the sedimentary cover. Indeed, the LNGS is located inside a U- and Th-poor carbonate mountain. Two explorative drill cores made at the time of excavation for the detector provided an opportunity to measure U and Th abundances of the rocks in the tunnel by means of a GeLi instrument [*Campos Venuti et al., 1982*]. Thirty samples were collected and analysed, with the result a(U) = (0.12 ± 0.11) ppm and a(Th) = (0.45 ± 0.16) ppm.

Upper Crust

In the last two decades a great effort has been dedicated in order to infer crustal composition as a function of depth by comparing the results of seismic profiles with high-pressure laboratory measurements of seismic velocity for a wide range of rocks [*Holbrook et al., 1992*; *Christensen and Mooney, 1995*; *Rudnick and Fountain, 1995*; *Wedepohl, 1995*; *Gao et al., 1998*; *Behn and Kelemen, 2003*].

Although the compressional wave velocity depends on many factors (temperature, mineralogical composition, confining pressure, anisotropy and pore fluid pressure), felsic rocks are characterized by sound speed generally lower than in mafic rocks. Two groups of samples were thus defined: one felsic and another intermediate/mafic. Average elemental abundances for the two groups were calculated and seismic arguments used in order to fix their relative amounts within UC.

The collected felsic rock types (granite, granodiorite, quartz schist and felsic gneiss) are characterized by compressional wave velocity $v_p(f)$ near 6.2 km/s, while intermediate/mafic rock types (amphibolite, diorite and gabbro) have $v_p(m)$ close to 6.8 km/s. These values for v_p refer to a depth of about 15 km, assuming a stable geotherm (15°C/km) [*Holbrook et al., 1992*; *Christensen and Mooney, 1995*].

Several authors have investigated the deep structure of the central Apennines, in particular analysing data from the eastern part of CROP 11 [*Finetti, 2005b*; *Cassinis et al., 2005*; *Patacca et al., 2008*; *Di Luzio et al., 2009*]. For this area the comparison among different estimates, yields for the upper crust:

$$v_p = 6.32 \pm 0.30 \text{ km/s}.$$

From these data it can be deduced that the upper portion of the crust of the central Italy is prevalently felsic. The fraction f of felsic rocks and that of mafic rocks $(m=1-f)$ can be determined by requiring that the observed value of v_p in the crust is reproduced, i.e. $f = [v_p(m)-v_p] / [v_p(m)-v_p(f)]$. This gives:

$$f = 0.75 \pm 0.40$$

It is clear that values >1 are meaningless from a geological point of view. They derived from the fact that $v_p(f)$ results greater than the lowest value of v_p. Nevertheless, this result is consistent with the composition of crustal models available in the literature. Christensen and Mooney [*Christensen and Mooney, 1995*] assigned 75% of felsic and 25% of mafic rocks to the crustal depth between 10 and 25 kms. Wedephol [*Wedephol, 1995*] identifies nearly 85% of felsic and 15% of mafic reservoirs for the (sediment-free) UC layer and marks the transition UC/LC with the 6.5 km/sec discontinuity in the European Geotraverse. Rudnick and Gao [*Rudnick and Gao, 2003*] distinguish an upper from a middle crust. Their middle crust includes rocks on amphibolitic facies. They describe several exposed middle crust cross-sections worldwide, where the felsic reservoir generally predominates (90%).

Table 3.10. U and Th abundances for the Upper Crust obtained from mass weighted average. Approximate average densities are from [*Telford et al., 1990*] and are in agreement with the densities assumed by [*Laske et al., 2001*] for the rest of the world. Uncertainties on the mass weighted average are calculated taking also into account the spread on the mafic/felsic ratios.

Reservoir		Density [g/cm^3]	Volume [%]	Mass [%]	a(U) [ppm]	a(Th) [ppm]
Upper Crust	Mafic	3.0	25	27	0.4 ± 0.1	0.3 ± 0.1
	Felsic	2.7	75	73	2.8 ± 0.3	11.0 ± 0.9
Mass weighted average					2.2 ± 0.4	8.1 ± 1.6
[*Rudnick and Gao, 2003*]					2.5	9.8

At this point the elemental abundances a for the whole Upper Crust can be calculated, from $a = a_f f + a_m (1-f)$, where a_f and a_m represent the U or Th abundances in the felsic and mafic reservoirs respectively, which in turn result from the arithmetical average. The dispersion among the samples is larger than the measurement errors. The results are shown in Table 3.10, where

comparable uncertainties arise from the spread of elemental abundances among rock types and from the uncertainty on the felsic/mafic percentage.
The range of published values for U and Th abundances in the UC, which were used in previous reference models, (last line of Table 3.10 [*Rudnick and Gao, 2003*]) essentially overlaps with the range provided by our estimates. These latters have no pretension of being more accurate: by using material collected in a region relatively close to central Italy

Lower Crust

LC rocks are available only thanks to tectonic processes which denudate the deepest portion of the crust or to basaltic magmatism scavenging small pieces of LC (xenoliths) during their uprising from the mantle to the Earth' surface. The two geological evidences however lead to contrasting results as far as relative proportions of mafic and felsic rocks are concerned. As reviewed by [*Rudnick and Fountain, 1995*], mafic rocks are more represented in xenoliths, than usually are in tectonically emplaced LC terrains where, on the contrary, felsic rocks are equally encountered if not predominant. Horizontal heterogeneity within LC is of course expected, but the simplest explanation for this contrast may lie on the tool, which was used for sampling. Where basalts are present, underplating process may have been working even for a long while, thus mafic rocks in this settings - where xenoliths are taken - may be more extensively represented.

Analyses show that U abundance is quite low in all granulites (0.01-1.14 ppm), while the average Th content in felsic granulites is more than one order of magnitude higher than in the mafic (see also [*Schnetger, 1994*]). Values for the four samples of mafic rocks and for the five samples of felsic lower crustal rocks have been averaged and results are reported in Table 3.11. Once again, however the relative proportions of the two components needs to be determined by using indirect methods.

Following seismic arguments sound speeds in the range 6.7-7.2 km/s have been detected in the area of interest [*Ponziani et al., 1995; Finetti, 2005b; Cassinis et al., 2005; Mele et al., 2006; Patacca et al., 2008; Di Luzio et al., 2009*]. This range appears to be in agreement with [*Christensen and Mooney, 1995*] and [*Holbrook et al., 1992*] who measured an average p-waves velocity of 6.3 and 7.0 for the felsic and mafic reservoirs respectively. If the lowest value is considered a felsic/mafic proportion of ca. 40/60 can be obtained, whereas the highest value would bring the composition of the LC completely composed by mafic rocks.

Taking into account the above reported geophysical and geochemical evidences the percentage of mafic rocks can be finally estimated to be:

$$m = 0.60 \pm 0.40$$

This result is in agreement with the felsic/mafic mixture proposed by [*Wedephol, 1995; Rudnick and Fountain, 1995; Gao et al 1998*].

Using this percentage the U and Th abundances in the whole LC can be obtained: a(U)=(0.3±0.1) ppm and a(Th)=(2.6±1.2) ppm (Table 3.11).

As in the case of UC, the ranges of published values for U and Th abundances in the LC, which were used in previous reference models (last line of Table 3.11) [*Rudnick and Gao, 2003*], essentially overlap with this estimate.

TABLE 3.11 – U and Th abundances for the lower crust.

Reservoir		*a*(U) [ppm]	*a*(Th) [ppm]
Lower Crust	Mafic	0.1 ± 0.1	0.2 ± 0.1
	Felsic	0.5 ± 0.2	6.1 ± 2.3
Mass weighted average		0.3 ± 0.1	2.6 ± 1.2
[*Rudnick and Gao, 2003*]		0.6	3.7

3.3.3 Geophysical model of the Gran Sasso area

The Central Tile

A simplified three dimensional (3D) model has been developed on an area of 2° x 2° of latitude and longitude, centred on the LNGS (Central Tile) (Figs. 3.9). The upper boundary of the model was fixed at the mean sea-level whereas the lower boundary was fixed at the Moho discontinuity.

The starting points for model building are the profiles published by the CROP Project [*Finetti, 2005a*]. Although various models have been recently proposed [*Cavinato and De Celles, 1999*; *Billi et al. 2006*, *Di Luzio et al. 2009*] the Finetti's model was followed because of the more abundant information in the sections. The Moho surface was extracted by digitizing the Moho Isopachs Map (CROP) for both Adriatic and Apenninic crustal blocks [*Finetti, 2005b*]. The Moho surface of the Adriatic micro-plate required a propagation of the data under the Apenninic crust because of the absence of information in the Moho Isopachs map. The propagation required the application of a kriging interpolation corrected with cubical drift because the non stationarity of the surface. This propagation was also used to check the base of the crust with respect to the available crustal sections published in [*Finetti et al. 2005b*].

The conversion from travel-times to actual depths [*Finetti, 2005b*] was performed going upward, starting from the constructed Moho surface. This solution was preferred because of the strong uncertainties for the velocities in the sedimentary cover as explained by [*Finetti 2005b*]. It also provides more regular velocities of the Upper and Lower Crust with respect to the Sedimentary Cover. In fact, only printed versions of the crustal seismic sections were used, implying some errors coming from the graphical representation. In particular, the most uncertainties were concentrated in the upper part of the crust (Sedimentary Cover), where public domain data coming from the hydrocarbon explorations were used. Geophysical profiles were then cross-checked with position and depth of the various formation obtained from 53 exploration wells [*Mostardini and Merlini, 1986*]. The main inputs used for building the 3D model are summarized in Fig. 3.10.

A 3D grid was then constructed by using Schlumberger-Petrel software, in order to quantify the bulk rock volumes of the six main layers: 4 layers of sediments, UC and LC (see section 3.1). These model surfaces were also modelled using kriging interpolation with a cubical drift. For the model input more than 1000 points for the base of the grid and more than 250 points in the interior of the grid were used. The faults were modelled using more than 1000

points. The numerical output of the model is a file which contains, for each cell the latitude, longitude and depth of its center, volume of the cell and reservoir type. The grid has 1.1 x 10^6 cells, each with a volume of about 2 km^3. The typical size of each cell is 2 x 2 x 0.5 km. The size of structures which can be appreciated is however much larger, depending on the quantity and quality of the input data. The resulting model is illustrated in Fig. 3.11, which were built in order to satisfy and to cross-check with the CROP published models and interpretations on the Central Apennines of [*Finetti 2005a*]

After building the model, the total volumes for each crustal unit was calculated. From Table 3.9 it is evident that ca. 80% of the total volume of the sedimentary cover is given by the Permo-Mesozoic succession, the largest fraction being composed by the Mesozoic carbonate units. In contrast, [*Wedepohl 1995*] estimates about 40% of the mean European sedimentary cover consisting of carbonates.

It is interesting to compare the thickness of the different layers in the present model and in the CRUST 2.0 model (Table 3.8). The sediment layer is over 25 times thicker in the this study than assumed in the previous crustal model, whereas the Moho depths are within ten percent.

The main uncertainties in defining the points used for building the model come from velocity-depth conversion, which is critical for the best accuracy of the grid. The uncertainties were estimated using the velocity-depth conversion using all available data in the literature about seismic velocities in the crust. The estimated depths of individual reservoirs are dependent on the model that is being used, whereas the Moho depth between the different models is within 15%.

The Rest of the Region

For the rest of the region a less detailed study was performed, since this area is expected to contribute a much smaller fraction of the signal. Three layers (sediments, upper and lower crust) were distinguished. The following geophysical information was used:

1) Moho depth is taken from the map of [*Finetti 2005b*].
2) The three CROP sections (n. 3 Pesaro–Pienza, n. 4 Barletta–Acropoli, n. 11 Pescara – Civitavecchia, and M2A) are used to build 29 virtual pits, extending from the surface to the Moho.
3) A structural axis, NW-SE [*Bigi et al., 1992*], corresponding to the merging between the Adriatic and European plates, was identified.
4) Information on the depth of each layer was obtained by linearly interpolating the values available on adjacent CROP lines along the structural axis.

In this way, the depth of different layers was estimated on a mesh of 1/4° x 1/4°. A representative view is shown in Fig. 3.12.

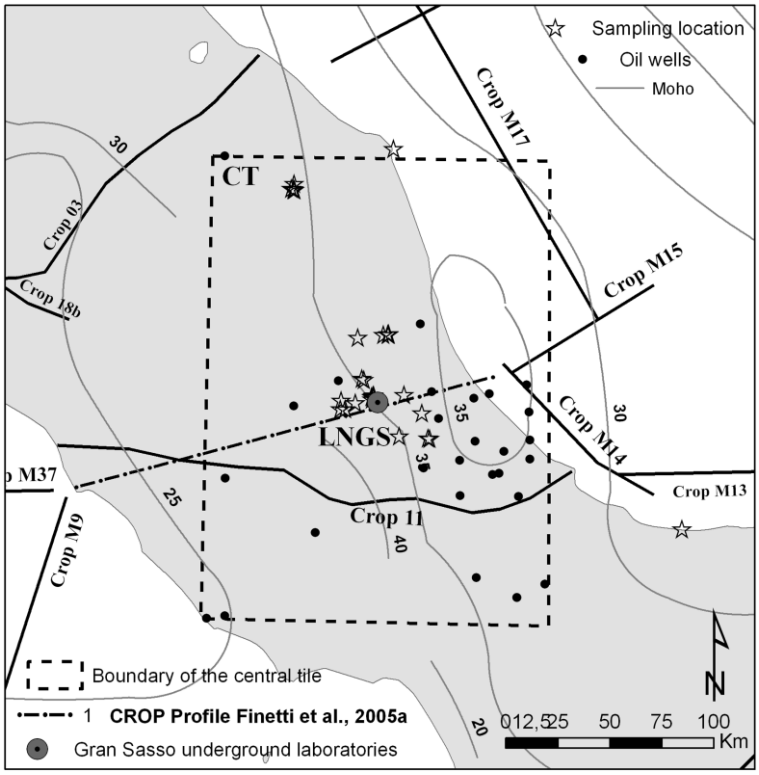

Fig. 3.10. The main inputs used for building the 3D model of the Central Tile. The dot-dashed line (RLSS) corresponds to the Reconstructed Lithospheric Seismological Section of [*Finetti, 2005a*]. EPC11 denotes the eastern part of CROP 11, used for comparison of different investigations. Also shown are the locations of the Sedimentary Cover samples used in this work.

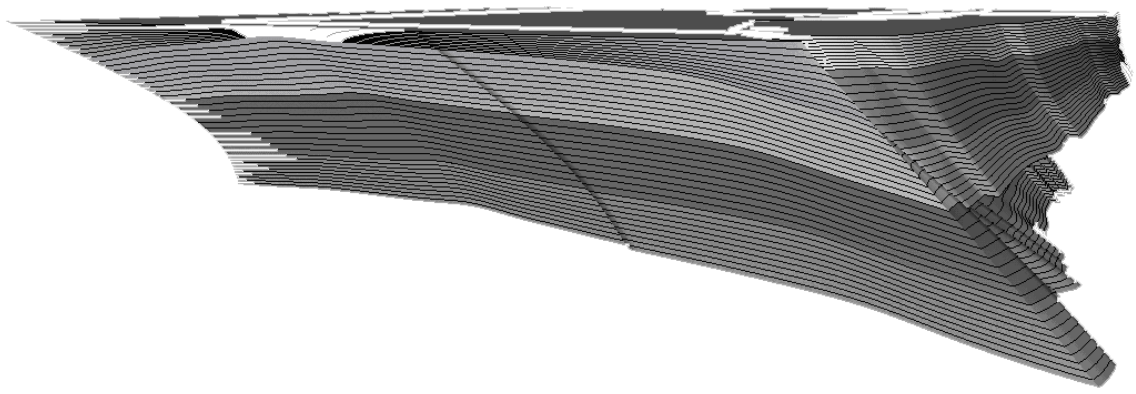

Fig. 3.11.A view of the 3D model of the central tile.

a) Sediments

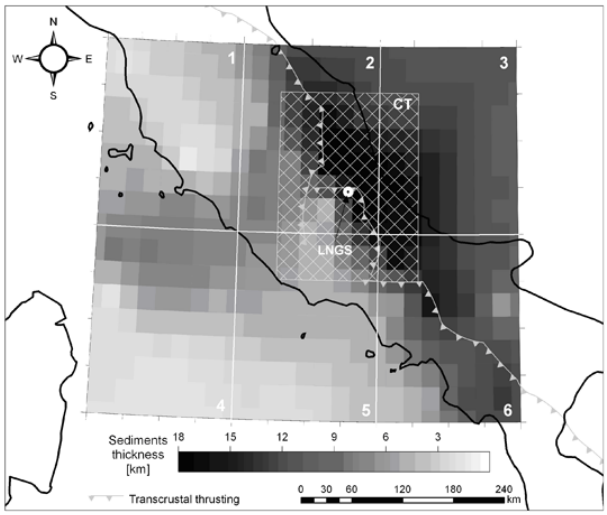

b) Upper Crust

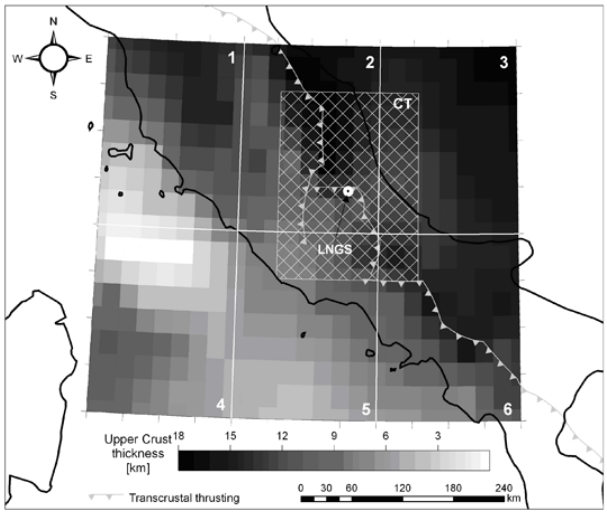

c) Lower Crust

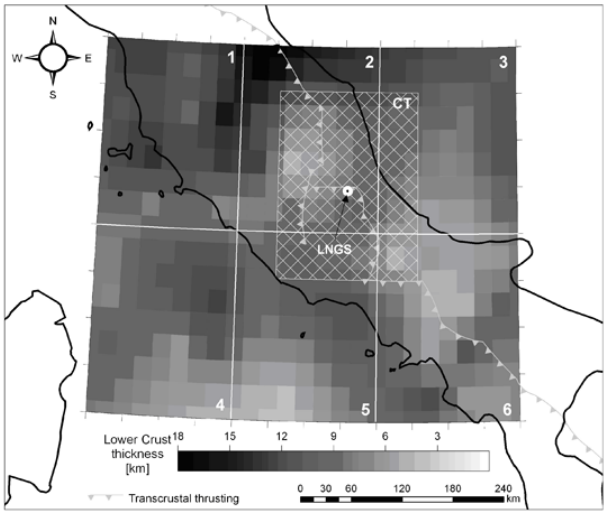

Fig. 3.12. Thickness of the three layers according to the 3D constructed geological model.

3.3.4 The predicted geoneutrino signal from the local area at Gran Sasso

At this stage, there are all the ingredients which are needed to estimate of the local contribution to geoneutrino signal from U and Th decay chains at the LNGS.

The Regional Contribution

For the central tile, a 3D model developed above was used. It distinguishes eight reservoirs, organized as follow: four for the SC (a, b1, b2 and b3), two for UC (felsic and mafic) and two for LC (felsic and mafic). For each of these reservoirs the derived U and Th abundances (Tables 3.9, 3.10 and 3.11) were used.

For the rest of the regional area, the model developed in section 3.3.3 was used, which distinguishes lower crust, upper crust and sediments, treated as a single and homogeneous layer. Results for U and Th abundances are adopted. For the overlying sedimentary rocks, we assume U and Th abundances to be given by the weighted average performed according to the lithology in the Gran Sasso area, where U- and Th-poor carbonates account for some ¾ by mass of the whole sediments (see below for the consequences of this assumption).

The predicted signal and its uncertainty

The local contribution from U+Th is 5 TNU lower than that of the reference model [*Mantovani et al. 2004*]. The main reason for this difference is due to the treatment of the sediment layer in the central tile. In fact, in this area the average Moho depth is close to the value found in [*Mantovani et al. 2004*], however the presence of a thick (some 13 km near Gran Sasso) sedimentary deposit composed primarily of U- and Th-poor carbonates essentially reduces the contribution to the signal. Note also that the regional values for the U and Th abundance in UC are some 10% lower than those assumed in the reference model. In contrast, assumptions about U and Th in the sediments for rest of the regional area have little impact on the estimated signal: if the world average abundances would be used in reference model the Th+U signal would increase by only 0.5 TNU.

With the aim of obtaining an estimate of the uncertainty, the signals contributed from each reservoir r the uncertainties of the elemental abundances a_r in that reservoir were propagated (see Table 3.12 and section 3.3.5). For each element, abundances in different reservoirs are assumed to be affected by independent uncertainties.

The resulting 1 σ uncertainties form the local area, ΔS_{LOC} (U) = 0.99 TNU and ΔS_{LOC} (Th)= 0.27 TNU. One has to observe that information on U and Th abundances are generally (at least partially) correlated, within each layer as well as for the BSE model: often, the abundance of one element is deduced from that of the other, assuming that the abundances ratio is better known. This is the case, for example, when rescaling the CI abundances in order to obtain the BSE estimate. Also, when considering the felsic/mafic rocks ratio in the crust, one introduces uncertainties that move U and Th abundances in the same direction. All these are positive correlations. Conservatively, it should be assumed that the errors affecting the U and Th signal are fully positively correlated, i.e.:

$$\Delta S(U+Th) = \Delta S(U) + \Delta S\ (Th) = 1.26\ TNU$$

3.3.5 Estimation of uncertainties

With the aim of obtaining an indication of the uncertainty on the regional contribution to the signal, two the signals S_r *(U)* and S_r *(Th)* were propagated from each reservoirs r the uncertainties of the elemental abundances a_r in each reservoir, with the following criteria:

i. uncertainties on the CT are fully correlated with those of the rest of the regional area, as based on the same measurements and on the same hypothesis. Thus it is assumed the relative error to be the same as that of CT and consider the whole regional area as a single block, subdivided into three reservoirs (Sediments, UC and LC)

ii. in each reservoir the contributed signal is proportional to the elemental abundance, $S_r = \alpha_r a_r$, so that the contributed error is

$$\Delta S_r = \alpha_r \Delta a_r$$

where for simplicity an index specifying the element (U or Th) is understood.

iii. uncertainties on the contribution of each reservoir are considered as independent of each other, as they derive from dispersions among the measurements of physically different sample sets; they will thus be combined in quadrature:

$$\Delta S_{reg} = \sqrt{\sum_r \Delta S_r^2}$$

For both U and Th, the contributed $\Delta S_r = \alpha_r \Delta a_r$ and the resulting ΔS_{reg} are calculated in Table 3.12.

Table 3.12– Estimated uncertainties on the geo-neutrino signal, in TNU, from the local area.

Area and reservoir	ΔS(U)	ΔS(Th)
Sediments	0.21	0.04
Upper Crust	0.96	0.24
Lower Crust	0.11	0.11
Local contribution, total	0.99	0.27

3.4 Model of the mantle

Information about the Earth decreases dramatically with depth. Particularly, direct sampling of rocks for lower mantle may not be obtained, since we cannot essentially reach it. Situation is slightly better in understanding of the upper mantle, because some portion of it is transported to the surface in ascending magmas, and is available for composition determination. On the other hand, geoneutrinos are an extraordinary probe of the deep Earth. These particles carry to the surface information about the chemical composition of the whole planet and, in comparison with other emissions of the planet (e.g., heat or noble gases), they escape freely and instantaneously from the Earth's interior.

Indeed, the mantle component to the measured geo-neutrino flux can be evaluated by subtracting the crust contribution [*Fiorentini 2012*]. It allows to test geological hypothesis about the mantle. On the other hand, the state-of-the-art information about the structure and composition of mantle can be used to calculate the total geo-neutrino flux and to verify the competing compositional models of the whole planet [*Sramek et al. 2012*].

It is necessary to note that existing detectors (Borexino and KamLAND) were built for the different scientific goals and detection of geo-neutrinos is just one of them. For reliable measurements of geoneutrino flux from the mantle, a new detector is needed to be built. It should be placed far from nuclear reactors, which is the main source of background (see chapter 4) and from the continental crust, were major amount of HPE is placed. Such detector (Hanohano) was proposed to be deployable in the ocean [*Learned et al., 2008*].

A simple model of the mantle is constructed here. A detailed investigation of the mantle is not a priority of this study. However the top of the mantle was considered more intently, since geo-neutrino signal decrease as $1/R^2$ with distance. The physical structure of mantle was based on PREM (Preliminary Earth Reference Model, a 1-D seismologically based global model [*Dziewonski and Anderson, 1981*]). The density profile tabulated in Table 2 of PREM is in a good agreement with the given parameterization, and the last was used Fig. 3.14.

The mantle is considered to be composed of three dominant reservoirs: the lithospheric mantle (LM), the DM (Depleted Mantle, which is the source of mid ocean-ridge-basalts – MORB), the EM (Enriched Mantle, which is the source of Ocean Island Basalts -- OIB). The definitions given by *Arevalo et al.* [2009] for the modern mantle, which is composed of two domains: a depleted mantle, DM, and a lower enriched mantle, EM is used. Amount of HPEs in EM is estimated through a mass balance of, assuming a BSE composition of McDonough and

Sun [McDonough and Sun , 1995].The hidden reservoir, which may or may not exist are not a consideration of this here.

3.4.1 Geophysical model of lithospheric mantle

Previous reference Earth models [*Dye, 2010; Enomoto et al., 2007; Fogli et al., 2006; 260 Mantovani et al., 2004*] have treated the crust and the mantle as two separate geophysical and geochemical reservoirs. In particular, the mantle was conventionally described as a shell between the crust and the core, and considered compositionally homogeneous. These models didn't consider the heterogeneous topography of the base of the crust, or the likely differences in composition of the lithospheric mantle underlying the oceanic and continental crusts.

The LM beneath the continents is treated here as a distinct geophysical and geochemical reservoir that is coupled to the crust (Fig. 3.1). The heterogeious depth of the LM top (D_{LM}) is evaluated from topography, bathymetry (H_{topo}) and thickness of crust (H_{Crust}):

$$D_{LM} = H_{topo} - H_{Crust}$$

where H_{topo} – can take negative values, H_{Crust} – thicknes of crust. Map of D_{LM} is shown in Fig. 3.13.

The LM beneath the oceans is assumed compositionally identical to DM, and therefore there was no attempt to constrain its thickness. The base of the CLM beneath the continents is difficult to constrain [*Artemieva, 2006; Conrad and Lithgow-Bertelloni, 2006; Gung et al., 2003; Pasyanos, 2010*]. The seismically, thermally and rheologically-defined depth to the base of the lithosphere may not be the same [*Jaupart and Mareschal, 1999; Jaupart et al., 1998; Jordan, 1975; Rudnick and Nyblade, 1999*], and the thickness of the lithosphere can vary significantly across tectonic provinces, ranging from about 100 km in areas affected by Phanerozoic tectonism, to ≥250 km in stable cratonic regions [*Artemieva*, 2006; *Pasyanos*, 2010]. Here, 175±75 km (half-range uncertainty; 1 σ) as representative of the average depth to the base of CLM is adopted (see Table 3.3).

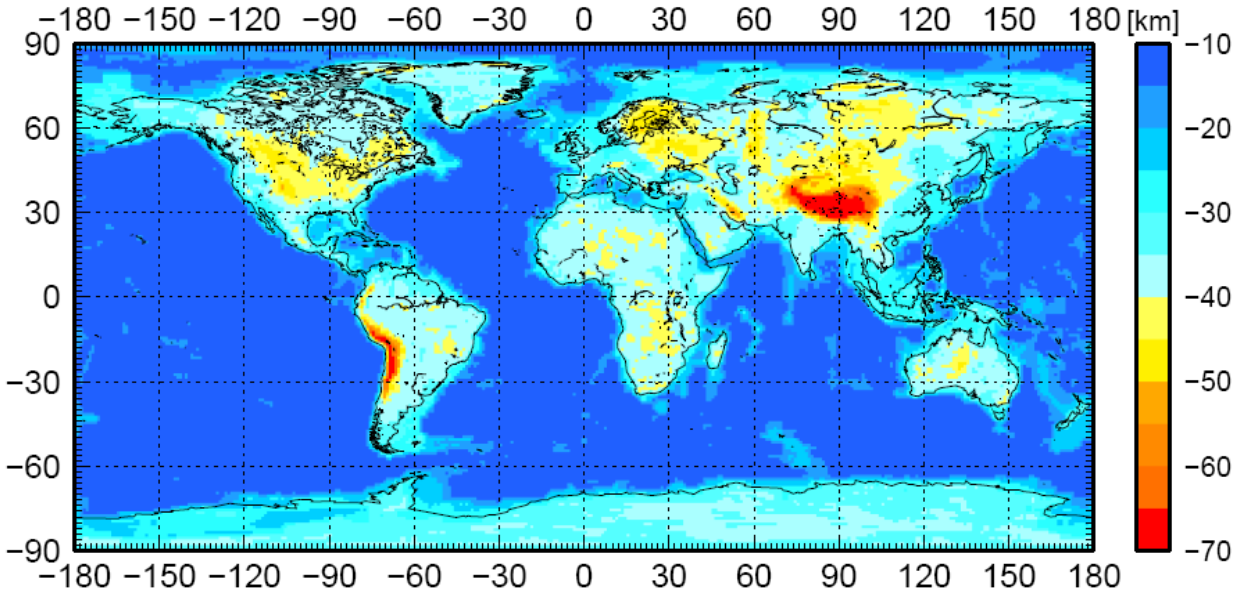

Fig. 3.13. The heterogeneous depth of the LM top

3.4.2 Geophysical model of sublithospheric mantle

The structure of mantle between the base of lithosphere and the core-mantle boundary (CMB) has been a topic of great debate. Tomographic images of subducting slabs suggest deep mantle convection [e.g., *van der Hilst et al., 1997*], while some geochemical observations favor a physically and chemically distinct upper and lower mantle, separated by the transition zone at the 660 km seismic discontinuity [e.g., *Kramers and Tolstikhin, 1997; Turcotte et al., 2001*]. Within the geochemical community, there is considerable disagreement regarding the composition of the upper and lower mantle [*Allègre et al., 1996; Boyet and Carlson, 2005; Javoy et al., 2010; McDonough and Sun, 1995; Murakami et al., 2012*].

For simplicity the sublithospheric mantle is treated here as two compositionally homogeneous reservoirs: depleted mantle (DM), which is on the top, and the underlying spherically symmetric enriched mantle (EM) (Fig. 3.1). The DM is the source region for MORB, which provide constraints on its chemical composition [*Arevalo and McDonough, 2010; Arevalo et al., 2009*]. The DM under CC and OC is variable in thickness due to the variable lithospheric thicknesses (Fig. 3.1). The EM is an enriched reservoir beneath the DM, and the boundary between the two reservoirs, extending up to 710 km above the CMB (Core Mantle Boundary), is estimated by assuming that EM accounts 18% of the total mass of the mantle [*Arevalo et al., 2009; Arevalo et al., 2012*].

3.4.3 Composition of continental lithospheric mantle (CLM)

The composition of the CLM is taken from an updated database of xenolithic peridotite compositions [*Huang et al. 2013*]. The mass of CLM is reported in Table 3.3; the main source of uncertainty comes from the average depth of the base of CLM, while the uncertainty on Moho depth gives a negligible contribution.

3.4.4 Composition of sublithospheric mantle (DM and EM)

Amount of HPE in the mantle was evaluated by using BSE model of [*McDonough and Sun 1995*]. The abundances of HPEs in the DM are ten times less than the global average MORB abundances [*Arevalo and McDonough, 2010*]; the enrichment factor of EM over DM is estimated through a mass balance of HPEs in the mantle. The compositions of the DM and EM (without any associated uncertainties) are reported in Table 3.3. No uncertainties are assigned here since the range of uncertainties is difficult to be estimated (usage of different BSE models gives different abundances of HPEs by factor of 2) and more detailed studies of mantle are presented in the literature. Sramek et al. [*Sramek et al. 2012*] provide a more comprehensive assessment of how different geophysical and geochemical mantle models influence the calculated geoneutrino fluxes from Earth's mantle. Different models of mantle are compared by Fiorentini et al. [*Fiorentini et al., 2012*] on the basis of available geoneutrino measurements.

3.4.5 Geoneutrino flux and radiogenic heat power

In the reference model consist of three main reservoirs: LM, DM and EM. LM mantle was introduced as an intermediate layer between mantle and crust. It link geophysical settings of these two reservoirs. Abundances of HPEs were accepted from geochemical measurements of representative samples. Corresponding mass of HPEs inside LM was evaluated (Table 3.5). The rest of the mantle is considered to consist from DM and EM. From the mass balance equation and BSE model amount of HPEs in these two layers was estimated. To calculate geo-neutrino flux DM and EM were considered as homogeneous spherical reservoirs. LM was divided into voxel following the model of crust (section 3.2).

According to the model developed here DM and EM account for 8.4 TNU. CLM contributes 2.2 TNU to the geoneutrino signal at Borexino. The uncertainties associated with the

signal coming from this portion of lithosphere are large, and an increase in signal by a factor three is permitted at the 1 σ level. Determining the distribution of U and Th in the lithospheric mantle sections underlying the detectors would thus be desirable in the future. Despite the fact that the mass of the CLM is about five times the crustal mass, it contains approximately 10% of the total mass of HPEs in the crust. The radiogenic heat power of CLM is $0.8^{+1.1}_{-0.6}$ TW: the main contribution to the uncertainty comes from the large 1 σ uncertainty of HPE abundances in peridotites.

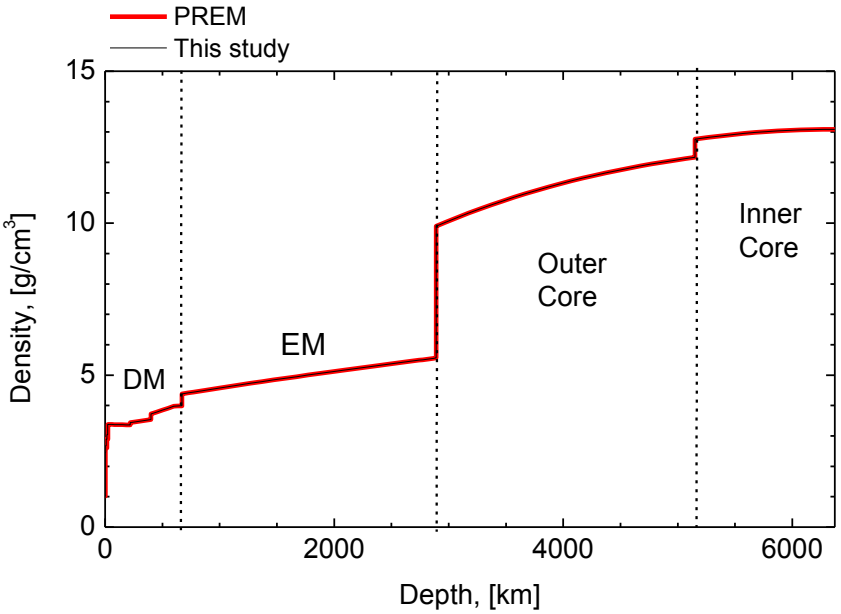

(a)

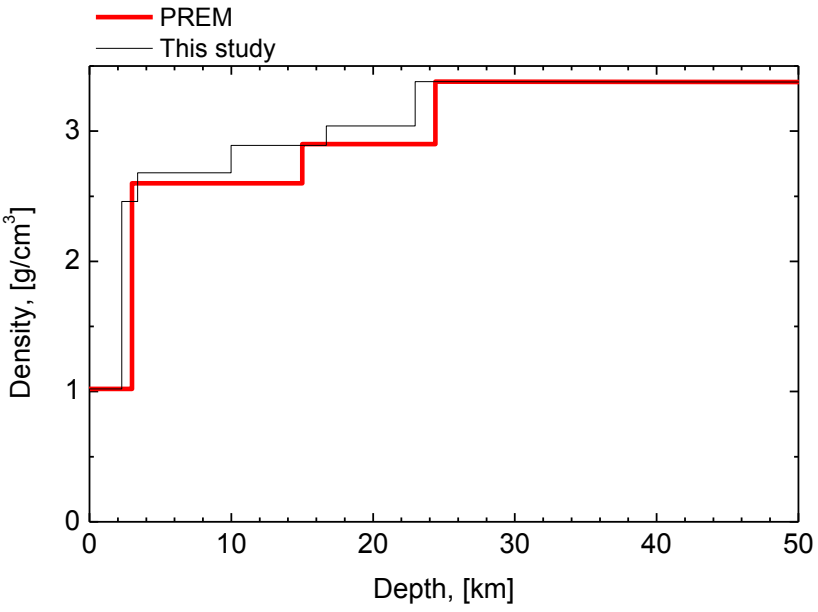

(b)

Fig. 3.14. The density profile of the develop reference model compared with PREM [*Dziewonski and Anderson, 1981*].

4 Antineutrinos from reactors expected in Borexino

The focus of this chapter is the calculation of antineutrino signal from nuclear power plants, as the fundamental background for geo-neutrino measurements. Beta decay of unstable isotopes inside reactors produces antineutrinos with energy up to 8 MeV and their spectrum overlaps the geo-neutrino energy window (LER) (Fig. 4.1). The High Energy Region (HER) has to be controlled to study the contributions from the nuclear reactors.

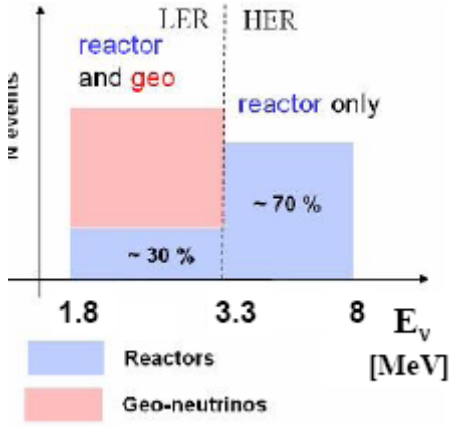

Fig. 4.1 Energies of geo- and anti- neutrinos.

Similar to geo-neutrino signal (S_{geo}), background from reactors (S_r) varies from place to place according to location of nuclear power plants, their type and thermal power. An important quantity for evaluating the potential of existing and future experiments is the ratio S_{geo}/S_r. Than bigger S_{geo}/S_r, than better accuracy of geo-neutrino flux and correspondingly more precise information about the Earth can be obtained after collecting required statistic.

The most isotopes produced by reactor fuel fission are short-lived, and neutrinos are emitted instantly following fuel fission. Thus the dominant background from nuclear power plants is produced by decay of short-lived isotopes, which can be calculated from the present operating experience of each nuclear power plant.

In the same time fission of nuclear fuel produce small fraction of long-lived isotopes. These isotopes are accumulated inside the fuel and decay slowly even after fuel is removed from nuclear power plant. The amount of long-lived isotopes depends on history of reactors operation. In the case of vicinity of exhausted fuel storing place to detector it can give a significant contribution to the background.

Only operating commercial reactors were considered to estimate the antineutrino background. Experimental, military and other reactors were not taken into account because of their comparably small thermal power and big distances from the neutrino experiments.

To evaluate background from reactors someone has to know amount of antineutrinos produced in reactor cores, their evolution during the movement to detector, and properties of detector.

4.1. Antineutrino flux produced in reactor cores

To evaluate the amount of antineutrinos produced in each reactor core the database was compiled. It includes the variation of general features of all cores in the period from December 2007 to August 2012. The total number of cores had minimal value equal to 438 in 2009 and maximal 439 in 2010. Database includes the following information about each core:

1. Location;
2. Designing characteristics: moment of time of the beginning of commercial operation, core type (PWR, BWR, PHWR, GCR, LWGR, FBR see Fig. 4.1), fuel material, fuel weight, fuel enrichment by ^{235}U, average fuel power, refueling frequency in month, part of core refueled, discharge burn up and moderator material;
3. Operating experience: annual thermal and electrical net capacities, monthly LF (definition is given in further).

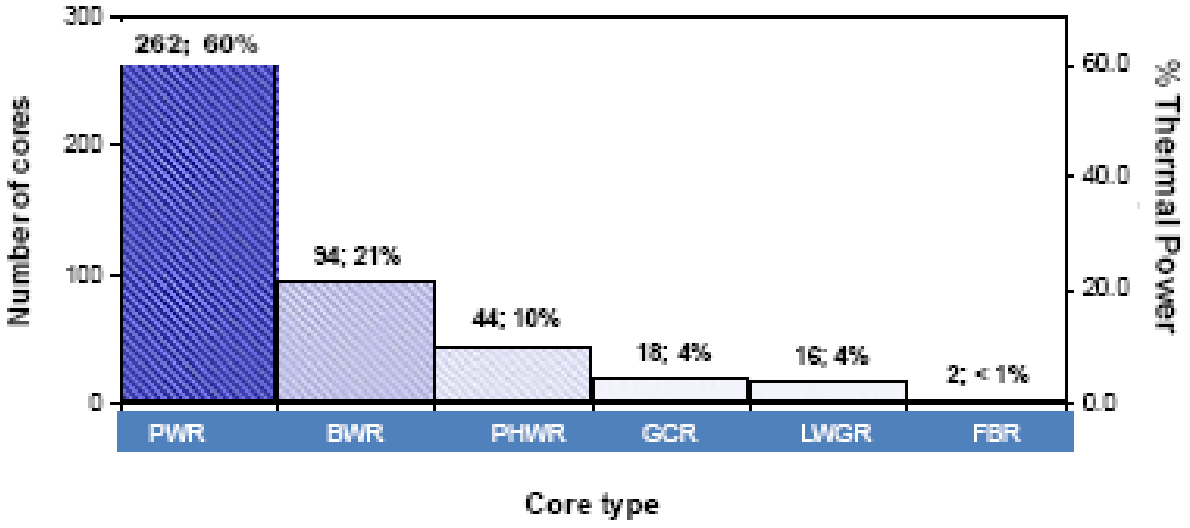

Fig.4.1 Number of cores of each type: pressurized water reactor (PWR), boiling water reactor (BWR), pressurized heavy water reactor (PHWR, includes CANDU reactors), gas-cooled reactor (GCR), light water graphite reactor (LWGR) and fast breeder reactor (FBR).

Locations of cores on the globe were taken from [*NASA database website*]. Designing characteristics, and information on operating experience was used from two documents published by International Atomic Energy Agency (IAEA) [*Nuclear Power Reactors in the World, Reference Data Series No.2, published since 1981; Operating Experience with Nuclear Power Plants in Member States, published since 1970*]. It is necessary to note, that designing characteristics can also be changed during reactor live time as a result of changes of operating conditions, environment or equipment.

In nuclear reactors electron antineutrinos with energies above the threshold eq. (1.1) are produced dominantly by the beta decay of the fission products from the four isotopes i = ^{235}U, ^{239}Pu, ^{238}U, and ^{241}Pu [*Huber and Schwetz, 2004*]. Contribution from other isotopes and fission fragments are well below 0.1% and were neglected. Ideally, we would like to know the fission rates (R_i) (i.e. number of fission per unit time), and antineutrino spectrum ($\lambda_i(E_\nu)$) for each isotope in each core. This was not fully succeeded. Antineutrino spectra parameterized by a polynomial fit were taken from [*Huber and Schwetz, 2004*]. Fission rates were expressed through the generated thermal power (P_{th}), energy released to the reactor per fission of each isotope (Q_i) and power fractions (p_i). Q_i presented in the Table 4.1 was taken from [*Huber and Schwetz, 2004*]. Assuming to know generated thermal power, the total fission rate R can be expressed through the average energy per one fission $<Q> = \sum f_i Q_i$

$$P_{th} = R <Q> \tag{4.1}$$

where f_i – the relative fission yield, the fraction of fissions which is produced by the i-th element:

$$R_i = f_i R = P_{th} f_i / <Q> \tag{4.2}$$

The same quantity can be expressed through the relative power yield p_i – the fraction of thermal power P_{th} which is produced by the i-th element:

$$R_i = P_{th}\, p_i / Q_i \tag{4.3}$$

Power fractions p_i should not be confused with fission fractions f_i. One can be obtained from another:

$$p_i = f_i \; Q_i / \sum f_i Q_i \tag{4.4}$$

The differences between p_i and f_i are small, of the order of 5MeV/200 MeV, however it is non zero.

I used p_i averaged over an operating cycle (between refueling outage times) presented in Table 4.1. For the cores with a low enriched uranium fuel (concentration of ^{235}U is about 3-5%) power fractions p_i were calculated from fission fractions f_i corresponding to the longest exposure of KamLAND [*S. Abe et al., 2008*] (^{235}U : ^{238}U : ^{239}Pu : ^{241}Pu = 0.570 : 0.078 : 0.295 : 0.057), which implies <Q>= 205.02 MeV. Different power fractions for cores, which burn a low

enriched uranium fuel, were found in the literature. They are presented in Table 4.1 for a comparison.

Another complication comes from the fact that more than 30 reactors use recycled fuel, so called MOX type. MOX is a mixed oxide fuel, which contains more than one oxide of fissile material. It use plutonium, recovered from spent nuclear fuel, blended with natural uranium, reprocessed uranium, or depleted uranium. MOX is an alternative to the low-enriched uranium fuel and it can be burned in light water reactors that predominate nuclear power generation. An attraction of MOX fuel is that it helps to utilize surplus weapons-grade plutonium, which is usually stored as nuclear waste. Thus it should reduce the risk of nuclear proliferation.

Today MOX fuel is used in Europe and in Japan. About 40 reactors in Europe (Belgium, Switzerland, Germany and France) are licensed to use MOX, and over 30 are doing so [*World Nuclear Association web site*]. In Japan about 10 reactors are licensed to use it and in 2010 Fukushima I was set the third to do so (Kyushu Electric's Genkai 3 started using MOX fuel in November 2009, and Shikoku's Ikata 3 loaded MOX fuel in March 2010).

Generally about 30% of the total power of these reactors comes from the MOX fuel (for some up to 50%), the remaining 70% of the power is produced by standard fuel. Medium power fractions of the MOX fuel were taken from [*Hagmann and Bernstein, 2003*] and presented in Table 4.1.

The power fractions for CANDU reactors, which burn natural uranium, were calculated. CANDU reactors are pressurized heavy water reactor invented in Canada. This type of reactors can burn uranium with natural abundance of ^{235}U. Fission fractions were calculated from the number of fission for each isotope [*Rae, 1997*]. CANDU power fractions are crucial for calculations of antineutrino background from reactors at SNO+ in Canada, where plenty of such reactors were built.

Table 4.1. Energy released to the reactor per fission (Q_k) and power fractions (*f*) (for different reactors) of each isotope according to different publications for different types of fuel.

	^{235}U	^{239}Pu	^{241}Pu	^{238}U	References
Q_k, [MeV]	201.7± 0.6	205.0± 0.9	210.0± 0.9	212.4± 1.0	[*Huber and Schwetz 2004*]
This study					
p (^{235}U enriched)	0.56	0.295	0.059	0.078	[*S. Abe et al., 2008*]
p (MOX)	0	0.708	0.212	0.08	[*Hagmann and Bernstein, 2003*]
p(CANDU)	0.54	0.41	0.02	0.02	
Different power fraction fond in the literature					
f (^{235}U enriched) = fuel composition	0.619	0.272	0.042	0.067	[*Hagmann and Bernstein, 2003*]
f (^{235}U enriched) = fuel composition	0.538	0.328	0.056	0.078	[*Mention et al., 2011*]
f (^{235}U enriched)	0.58	0.292	0.054	0.074	[*Djurcic et al., 2009*]
f (^{235}U enriched)	0.544	0.318	0.063	0.075	
f (^{235}U enriched)	0.577	0.292	0.057	0.074	
f (^{235}U enriched)	0.563	0.301	0.057	0.079	

To derive R_i it was necessary to know thermal power of reactor core. Determination of thermal power of operating nuclear core is a complex problem, moreover it is associated with a number of errors (instrumental, statistical, ect.). The most precise apparatus provide 0.5% accuracy [*Djurcic et al., 2009*]. Understanding impossibility of performing such measurements for all 440 cores and the fact that measured electrical power in general has better precision, thermal power was estimated on the basis of generated electrical one, taken from IAEA. For this goal we considered the following IAEA quantities:

- Energy Generated Net, EG [GW(e)h]: Net electrical energy produced during the reference period as measured at the unit outlet terminals, i.e. after deducting the electrical

energy taken by unit auxiliaries and the losses in transformers that are considered integral parts of the unit. If this quantity is less than zero, zero is reported.

- Reference Energy Generation, REG [MW(e)h]: Net electrical energy which would have been supplied to the grid if the unit were operated continuously at the reference unit power during the whole reference period.
- Load Factor, LF [%]: $LF = \frac{EG}{REG} \times 100$

Load factor, for a given period, is the ratio of the energy, which the power unit has produced over that period, to the energy it would have produced at its reference power capacity over that period.

- Thermal Capacity and Electrical Net Capacity [MW]: Reference thermal and electrical net capacities at the end of each year.

IAEA publish LF averaged over the whole period of plant operation, over one year and over one month. Thus LF allows to reconstruct amount of EG Net with temporal resolution of one month. Assuming constant efficiency of reactor (a very reasonable assumption, unless hardware upgrade is done in the power plant) generated thermal power can be evaluated as:

$$P_{th} = LF*\text{Thermal Capacity}$$

It gives P_{th} with an accuracy of 2%.

By using equations for R_i and parameterizations of $\lambda_i(E_v)$ the total flux from one core takes on a form:

$$\Phi(E_\nu) = P_{th} LF \sum_{k=1}^{N_{fuel}} \frac{p_k}{Q_k} \lambda_k(E_\nu) \tag{4.5}$$

4.2. Evolution of antineutrinos during their movement to detector

As it was already mentioned, locations of cores were taken from NASA database [*NASA database website*]. Each core was considered as a point source of antineutrinos because of big distance to them from detector. Distance (d) was calculated from spherical model of Earth with R=6371 km.

The survival probability is calculated by using eq. (1.6) and oscillation parameters reported in [*Fogli et al. 2011*] .

4.3. Detection of antineutrinos

A detection efficiency $\varepsilon = 1$ is assumed. Total number of free protons equal to $N_p = 10^{32}$ and temporal exposition $t = 3.15\ 10^7$ s (1 year) were used, which correspond to signal in TNU. Cross section $\sigma(E_\nu)$ of reaction (1.1) was taken from [*Strumia and Vissani, 2003*], eq. (1.2):

Final equation for antineutrino signal from reactors is:

$$N_{TOT} = \varepsilon N_p \tau \sum_{i=1}^{N_{reactor}} \frac{P_i}{4\pi d_i^2} \langle LF_i \rangle_{2009} \int dE_\nu \sum_{k=1}^{N_{fuel}} \frac{p_k}{Q_k} \lambda_k(E_\nu) P_{ee}(E_\nu, d_i) \sigma(E_\nu) \qquad (4.6)$$

4.4. Results and comments

The database of operating experience of all commercial nuclear power plants from December 2007 to August 2012 was built. Together with a review of the power fraction averaged over operating cycle for the main types of nuclear reactor cores allowed to estimate generated thermal power over this period. It, in turn, was used to calculated antineutrino signal (S_r) in Borexino detector which comes from nuclear reactors.

The average S_r in Borexino is equal to 88.8 TNU. In HER there are 65.2 TNU, and the rest 23.6 TNU are in geoneutrino energy window. Monthly evolution of the signal during last four years in geoneutrino energy range is presented in Fig 4.2.

The antineutrino signal in LER all over the globe was calculated Fig 4.3. Uncertainties and contribution of spent fuel were estimated (see Sec 4.5). Collected detailed information about nuclear power plants allowed to decrease the total uncertainties to 5%. Obtained results are in agreement with publications of other authors [*Bellini et al., 2010*].

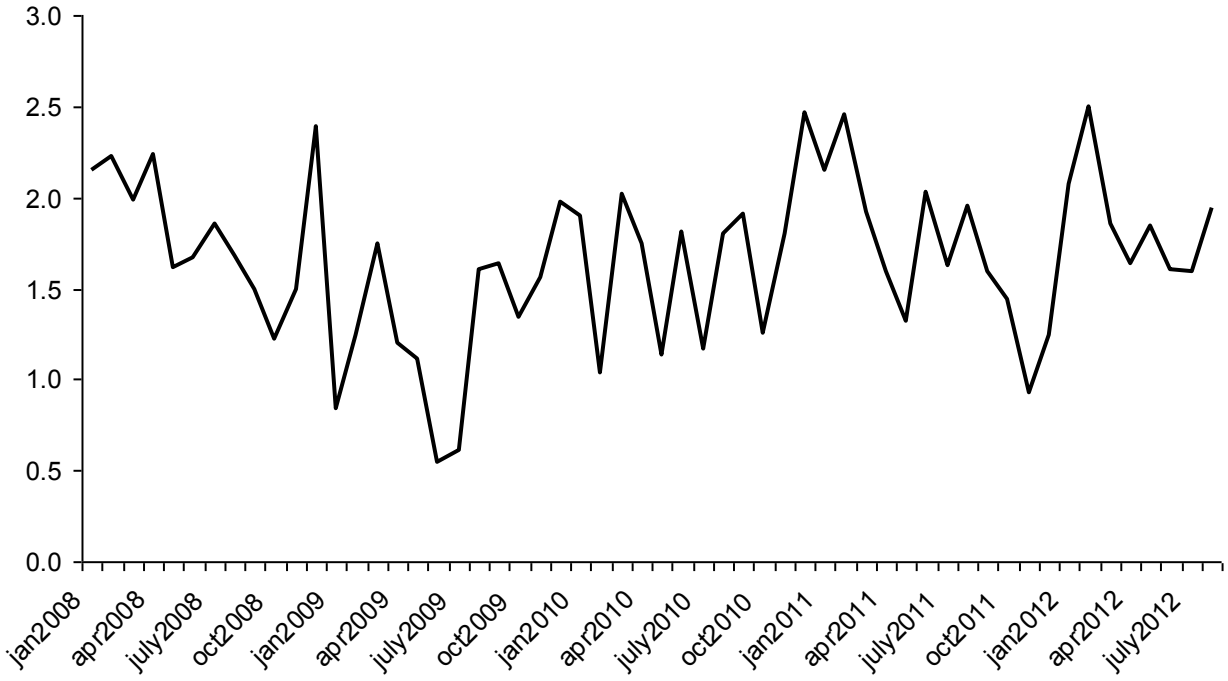

Fig.4.2. Monthly evolution of the event rate in Gran Sasso area, assuming a detector with efficiency equal to 1 and target volume contains 10^{32} protons.

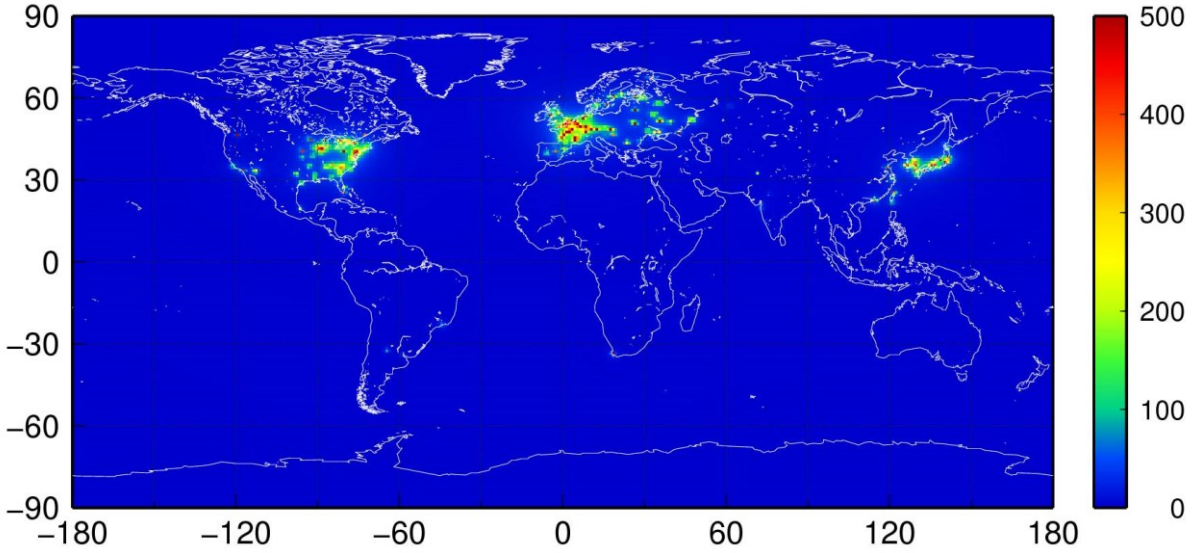

Fig. 4.3. Predicted antineutrino signal from nuclear power plants in geo-neutrino energy window. Signal is in TNU.

4.5. Estimation of uncertainties

Expression for calculation the antineutrino signal from reactors (4.6) has a complex structure. Because of it to analyze the total uncertainty all parameter were varied in allowable range independently from each other and followed the changes of the signal. The total uncertainty and its components are presented in Table 4.3.

4.5.1 Cross section

The paper [*Vissani and Strumia, 2003*] claims that "at low energy sigma has an overall 0.4% uncertainty" To take into account the error of the adopted parameterization, the cross section obtained with eq.(25) of [*Vissani and Strumia, 2003*] was compared with the "exact" values reported in Table 1 of [*Vissani and Strumia, 2003*]. It was found that the discrepancy is on the average 0.5% in the relevant energy range. In total, the error form the cross section is less than 1%.

4.5.2 Oscillation parameters

Δm^2 and θ are determined with their errors. The effect of these uncertainties was estimated by propagating them. The result, mainly due to the uncertainty on θ , is a 2.4 % effect at 1σ.

4.5.3 Antineutrino produced spectrum

Three points have to be noticed:

1) Parameterization

In [*Huber and Schwetz 2004*] two parameterizations of the neutrino spectrum are presented: polynomial of 2nd order and polynomial of 5th order. From fig. 1 of the paper, one can see that the 5th order polynomial represent a better fit to the data, mainly for $E_\nu > 7$MeV. For a comparison the expected signal in Borexino by using both the fits were calculated. The variation of result is less than 1%

2) Conversion of electron spectra to neutrino spectra

As stated in [*Vogel, 2007*], assuming a perfectly known electron spectrum, the neutrino spectrum can be reconstructed from a theoretical inversion procedure with a 1% error, provided several conditions are met (in particular, it is important that antineutrino energy bins are much larger than electron energy bins

3) Errors in the electron energy spectra

One starts with measured energy spectra, which have relatively large errors, of order of 4%. This is presumably the largest error source.

In the 2003 paper KamLAND states "The antineutrino spectrum per fission and its error (2.48%) are taken from the literature [^{235}U: *K. Schreckenbach et al., 1985*; ^{239,241}Pu : *A. A. Hahn et al.,1989*; ^{238}U: *Vogel et al., 1981*]". This is a reasonable estimate of the uncertainty.

4.5.4 Fuel composition

The KamLAND power fractions p_i were used for reactor, which burn ^{235}U enriched fuel. Also 35 European reactors with 30% of thermal power production from MOX fuel were added and 47 CANDU reactors.

To estimate uncertainties power fractions published by different authors were considered (see table 4.1). A 2% uncertainty is adopted form fuel composition as a conservative estimate.

4.5.5 Energy released for fission

In Table 4.1 the released energies from each fuel are reported with errors. It was found they imply an uncertainty of about 0.35%.

4.5.6 Numerical integration

The choice of the energy bin for numerical integration is relevant for the correctness and the stability of the result, see the Table 4.2. An energy bin of the order of 100 keV is necessary and sufficient for accuracy better than 1% on the total number of event level if 1MeV bins used the predicted event number is wrong by several percent and the oscillation pattern in the spectrum is lost.

Table 4.2. Antineutrino signal from reactors in TNU in the 1-10MeV energy range, as a function of Energy bin used in the integral of (eq. 4.6).

Ebin [MeV]	S_r, [TNU]
1	22.67
0.1	23.62
0.01	23.60
1.d-3	23.60
1.d-4	123.60

4.5.7 Reactor thermal power

An uncertainty of the thermal power of each core calculated on the basis of Thermal capacity and LF was estimated to be at the level of 2%. Which imply 2% uncertainty of the calculated signal.

4.5.8 Positions of cores

Assuming to know all coordinates with accuracy better than 0.5 km, the uncertainty of antineutrino signal should be less than 0.4%.

4.5.9 Effect of long lived nuclear reactor fission products

One has to remind that in addition to short lived fission products, there are other long lived isotopes (144Ce, 106Ru and 90 Sr) which are part of the "spent fuel" which can contribute to the neutrino spectrum. Sanshiro [*Sanshiro, 2005*] estimates these to provide an additional contribution of 2.4%. This contribution is hard to estimate, since it depends on how and were the spent fuel is stored. Conservatively, the Sanshiro's estimate is adopted and attribute an uncertainty of 1%.

Table 4.3. Different contribution to the total uncertainty of calculated signal for Borexino detector.

Source	Uncertainty
$\sigma(E)$	±1 %
Δm^2	±0.025%
θ	±2.6%
antineutrino spectrum	±2.5 %
Fuel composition	± 2%
Q_i	±0.35%
Thermal Power	± 2%
Positions of cores	±0.41%
Long lived isotopes	±1 %
Total error	**± 5%**

5 Antineutrinos in Borexino: expected signal and its uncertainties

5.1 Structure of Borexino detector

Several detectors (KamLAND, Borexino, SNO+, LENA, Hanohano, Baksan) were proposed for geo-neutrino measurements. KamLAND, at the Kamioka mine in Japan, and Borexino, at the Gran Sasso underground laboratories in Italy, are the only two of them which are currently operative. Initially designed for the goals other than detection of geo-neutrinos, they already provided first measurements of it [*Araki et al., 2005; Gando et al., 2011, Bellini et al., 2010*]. The SNO+ detector at the Sudbury Neutrino Observatory, Canada [*Chen, 2006*], will start to collect data in 2013.

The Borexino [*Alimonti G., et al., 2009a; Alimonti G., et al., 2009b*], is located deep underground in the Hall C of the National Laboratories at Gran Sasso. The 3800 m of water equivalent above the detector reduce the muon flux by a factor of about 10^6. The initial goal of the experiment was the detection of the neutrinos emitted from the Sun [*Marx G., 1960*] and some results of this measurement have been already published [*Arpesella, et al., 2008a; Arpesella, et al., 2008b, Bellini, et al., 2010b.*]. Meantime it was observed that radioactive background in Borexino is very low, which results in a potential broadening of the scientific scope of the experiment. Particularly it allowed detection of geo-neutrinos.

The structure of such detectors (Borexino and KamLAND) is almost the same and consists of several concentric spherical shells Fig 5.1. The inner shell is confined within a thin spherical nylon vessel with a radius of 4.25 m and contains of about 300 tons (~ 100 ton of "fiducial volume") of liquid scintillator (LS). The outer vessel, with a diameter 5.5 m, prevents ^{222}Rn emanated from the external materials (steel, glass, PMT materials) diffuse into the fiducial volume. Outer vessel is placed in a stainless steel sphere (SSS), which has a radius 6.85 m and is supported by 20 steel legs. The buffer fluid between the inner vessel and the SSS is the last shielding against external backgrounds. The scintillation light is detected by 2212 8" PMT's, which are mounted on the SSS and cover nearly 30% of the sphere. 1828 PMTs have light concentrators in order to reject light coming not from the active scintillator volume and to reduce the background. The rest 384 PMTs are without concentrators can be used to study background. The SSS is enclosed within a large tank water tank. The tank has a cylindrical shape with a diameter of 18 m and a hemispherical top with a maximum height of 16.9m. It is filled with ultra-pure water, which shields against external background (γ rays and neutrons from the rock)

and serve as Cherenkov muon counter and muon tracker. 208 PMTs measure the Cherenkov light emitted by muons in water.

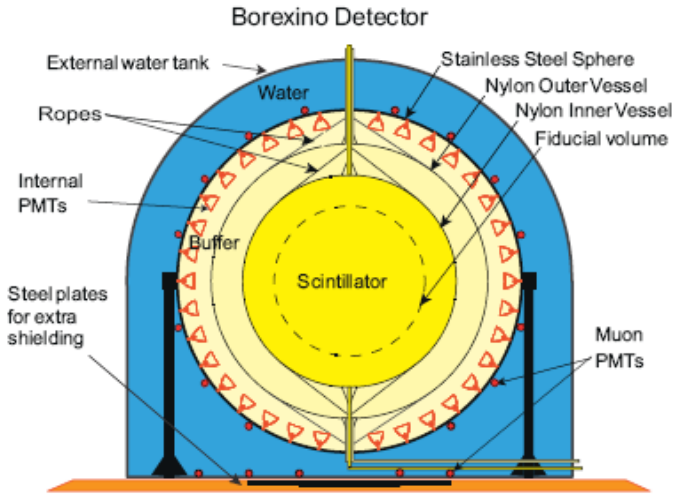

Fig. 5.1 Scheme of Borexino detector.

The electron antineutrinos at Borexino are detected by means of their inverse neutron beta decay:

$$\bar{\nu}_e + p \rightarrow e^+ + n - 1.806\text{MeV} \qquad (5.1)$$

The liquid scintillator (LS) essentially consists of hydrocarbons (C_nH_{2n}) which provide the hydrogen nuclei acting as targets for antineutrinos. The energy threshold of the reaction, 1.806 MeV, is low enough to detect a part of geo-neutrinos from ^{238}U and ^{232}Th-series, but not those from ^{40}K (Table 1.1).

The reaction makes two correlated signals (Fig. 5.2). The first signal, prompt signal, is made by the positron and two 0.51 MeV gamma particles generated by annihilation of the positron. The second signal, delayed signal, is made by a 2.2 MeV gamma particle, which is emitted in subsequence of thermal neutron capture on proton. This thermalization and capture process take about 200 μsec, and positions of neutron capture are typically 30~50 cm apart from the neutrino reaction vertices [16]. Measurement of two time and space correlated signals (prompt and fast) from antineutrinos provide an effective method for discrimination of background.

It is necessary to note, that Borexino detector allows to measure position and energy of scintillation events, but not the direction of the incoming neutrinos.

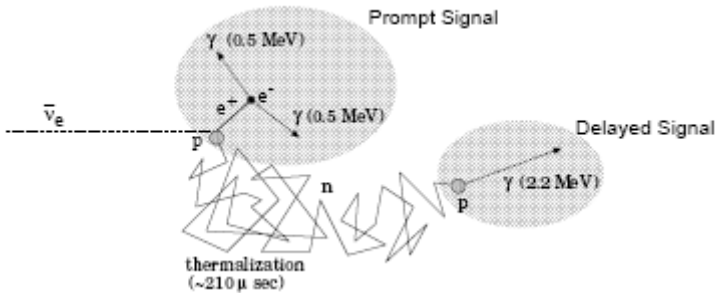

Fig 5.2 Scheme of antineutrino detection.

The necessity to measure a low neutrino flux with a massive detector requires high radiopurity of the scintillator and also the surrounding materials, since the neutrino induced events are intrinsically indistinguishable from β and γ radioactivity. It has been developed purification techniques for scintillator, water, and nitrogen. And a careful material selection has been performed. Additionally, the detector is designed to shield neutrino target (100 ton of "fiducial volume" in Borexino) from external γ radiation and neutrons originating from the rock and from the detector materials.

5.2 Geoneutrino measurements by Borexino detector

Borexino started to collect geo-neutrino data in December 2007 and in March 2010 published a first evidence of geo-neutrino with more than 3σ C.L [29]. The data were collected during 537.2 live time days (from December 2007 until December 2009). The fiducial exposure after cuts was 252.6 ton·yr. In spite of a total exposure of only 0.15×10^{32} target proton years, the absence of nearby reactors and the high purity of the LS resulted in a measurement of the signal with relatively small uncertainties.

After all selection cuts [Bellini et al. 2010] there were found 21 antineutrino events: 15 were in geo-neutrino energy window (LER) and 6 had higher energy (HER). 6 events events in HER are treated as antineutrinos from reactors. The expected number of background events with non antineutrino origin was evaluated to be 0.40 ± 0.05. Since there is no any other known source of antineutrinos, which could give a considerable contribution to the measured signal, an unbinned maximum likelihood analysis of the 21 observed events was made. An expected spectrum for electron antineutrinos in Borexino was used (Fig. 5.3, 5.4) to get the best fit. It gives $N_{geo} = 9.9^{+4.1}_{-3.4}$, $N_{react} = 10.7^{+4.3}_{-3.4}$ with 1 σ uncertainty. Expressed in TNU it is equal to $\mathrm{S_{geo}(U+Th)} = 64^{+26}_{-22}\mathrm{TNU}$, $\mathrm{S_{react}} = 69^{+28}_{-22}\mathrm{TNU}$.

The signal measured by the Borexino collaboration is closer to the prediction for a fully radiogenic model of Earth $\mathrm{H(U+Th)} = 43^{+29}_{-23}\mathrm{TW}$. However discrimination between BSE and fully radiogenic model of Earth requires smaller errors.

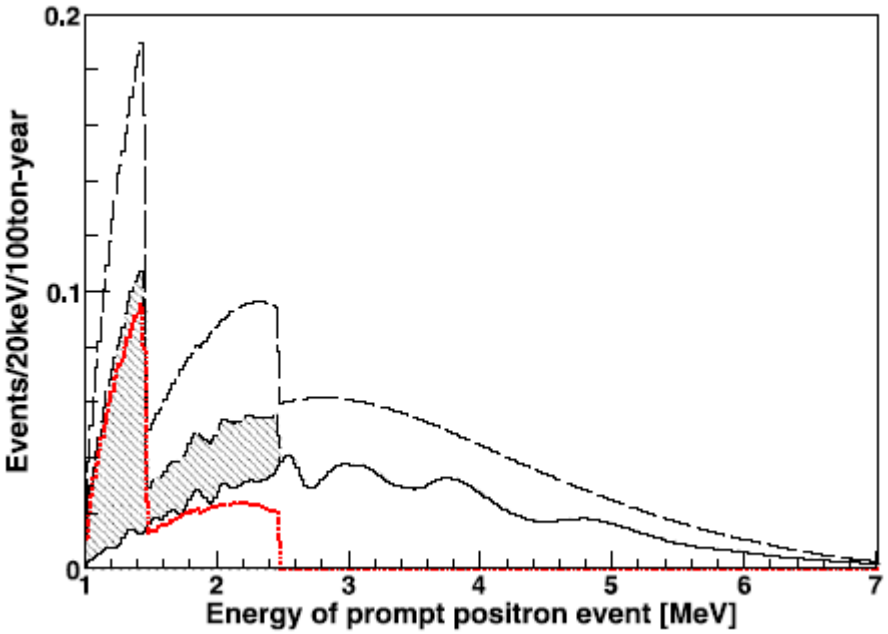

Fig. 5.3. Expected spectrum for electron anti-neutrinos in Borexino. The horizontal axis shows the kinetic plus the annihilation 1.022 MeV energy of the prompt positron event. Dashed line: total geoneutrino plus reactor antineutrino spectrum without oscillations. Solid thick lines geoneutrino and reactor antineutrino spectrum with oscillations. Dotted line (red): geoneutrino spectrum with the high (low) energy peak due to decays in the ^{238}U chain (238U + 232Th chains). Solid thin line is reactor antineutrinos [*Bellini et al. 2010*].

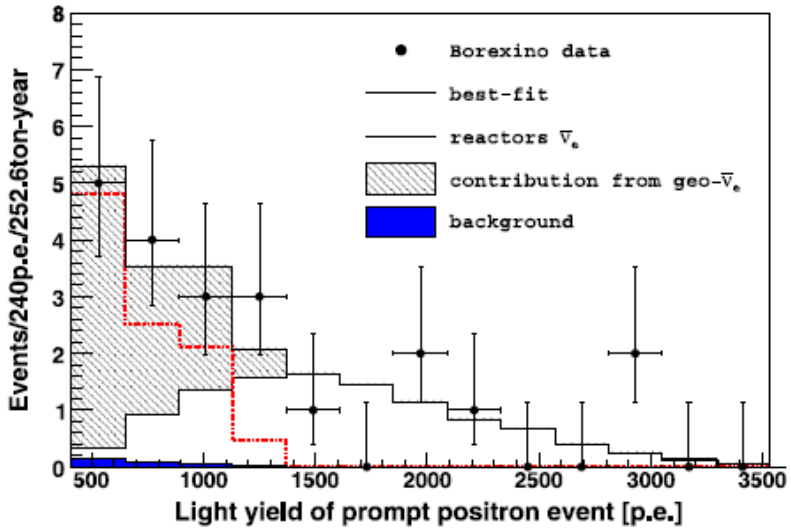

Fig. 5.4. Light yield spectrum for the positron prompt events of the 21 antineutrino candidates and the best-fit (solid thick line). The horizontal axis shows the number of photo electrons (p.e.). detected by the PMTs. The small filled area on the lower left part of the spectrum is the background. Thin solid line: reactor antineutrino signal from the fit. Dotted line (red): geoneutrino signal resulting from the fit. The darker area isolates the contribution of the

geoneutrino in the total signal. The conversion from p.e. to energy is approximately 500 p.e./MeV [*Bellini et al., 2010*].

5.3 Calculated geoneutrino flux at Gran Sasso

At this stage, there are all the ingredients which are needed to estimate the total geoneutrino signal from U and Th decay chains at the LNGS. From the 3D model developed above and a detailed study applied to the twenty four 1°×1° tiles around LNGS allowed to evaluate the local contribution to the geoneutrino signal at Borexino S_{LOC} = 5.95 ± 1.26 TNU (section 3.3).

For the global crust a new reference model was developed. Subtraction of the six crustal tiles around Borexino gives the geoneutrino signal from the rest of the crust equal to $S_{ROC} = 13.7^{+2.8}_{-2.3}$ TNU (section 3.2). Table 5.1 summarizes the contribution of the different reservoirs to the total refined geoneutrino signal. For the both S_{LOC} and S_{ROC} geophysical and geochemical uncertainties were propagated to estimate the overall uncertainty. Generally the measured abundances of HPEs in representative samples have a large spread which yields to dominance of geochemical uncertainties.

The previous reference models estimated the geoneutrino signal at Borexino at the level of 41 TNU (Table 3.1). The geoneutrino signal predicted on the ground of developed model here is $34.3^{+4.4}_{-2.9}$ TNU. However the predicted signal is still agree with the previous reference models because of big interval of uncertainties, the special attention should be paid to it. The large diminution of the signal is due to 3 refinements made gradually in the last years.

Study of the local area displayed a thick layer of sediments beneath Gran Sasso, with poor concentration of HPEs. They are thicker by more than twenty times than considered in the reference model (Table 3.8). Furthermore analysis of representative rocks has shown that sediments in this area have low abundances of U and Th: 0.8 μg/g and 2.0 μg/g instead of previously used 1.7 μg/g and 6.9 μg/g for U and Th correspondingly (Table 3.9). In total it resulted in a decrease of the local contribution to the signal by approximately 5 TNU.

Geophysical and geochemical refinements of the global reference model were performed. The thickness of the crust was calculated from three model based on different geological arguments. It is an attempt to use scattered geological knowledge to estimate geophysical properties of crust and to evaluate their uncertainties. Moreover, use of the recently developed GEMMA model [*Negretti et al., 2012*] provides a unique chance to increase significantly detail of the crust. New CC crust is 1.3 km thinner than the previous estimate. It decreases the signal by about 1 TNU. Thickness of OC increased, but it contains negligible amount HPEs and doesn't influence the signal. New estimates of U and Th concentration in MC and LC were performed.

Table 5.1 First part of the table indicates the predicted geoneutrino signal at Borexino from different reservoirs for the developed local and global Earth models. The second part presents the average background in the last four years from nuclear reactors all over the world. All values are in TNU.

	Borexino 42.45 N, 13.57 E		
	S(U)	S(Th)	S(U+Th)
LOC	8.09 ± 0.99	1.93 ± 0.27	10.02 ± 1.26
ROC	$10.3^{+2.6}_{-2.2}$	$3.2^{+1.1}_{-0.7}$	$13.7^{+2.8}_{-2.3}$
CLM	$1.4^{+2.7}_{-1.0}$	$0.4^{+1.0}_{-0.3}$	$2.2^{+3.1}_{-1.3}$
DM	4.1	0.8	4.9
EM	2.7	0.8	3.5
Grand Total	$34.3^{+4.4}_{-2.9}$		--
Background from reactors LER	65.2 ± 3.3		
Background from reactors HER	23.6 ± 1.2		

New estimates for abundances of HPEs in MC and LC continental crust were derived on the ground of seismic arguments. In comparison with the previously accepted model of [*Rudnick and Gao, 2003*] it gives: 0.97 and 4.86 μg/g instead of 1.3 and 6.5 μg/g for U and Th correspondingly in MC; 0.16 and 0.96 μg/g instead of 0.2 and 1.2 μg/g for U and Th in LC. In the reference model developed here distribution of U and Th is not homogeneous all over the Earth, which seems more realistic (Fig. 3.6). It also decreases a total geoneutrino signal by approximately 1 TNU.

Signal from the mantle in the reference model contributes 9.4 TNU and it is essentially the same as in the previous estimation [*Mantovani et al., 2004*, *Fogli et al., 2005*, *Enomoto, 2005*, *Dye, 2010*]. Continental lithospheric mantle was introduced here to study the top of the mantle. It is a first step for detailed study of the top mantle, which is requiring for investigation of the lower mantle by applying the experimentally measured geoneutrino signal [*Same et al. 2012, Fiorentini et al., 2012*]. Though mantle has relatively low abundances of HPEs and small

variation of its shape doesn't affect the signal. In general, amount of geoneutrinos generated in mantle is determined by the chosen BSE model that gives masses of HPEs.

All applied refinements are independent and in total they diminish the geoneutrino signal at Borexino by about 7 TNU. However the predicted signal S = $34.3^{+4.4}_{-2.9}$ TNU is somehow far from the first results of Borexino collaboration $S_{geo}(U+Th) = 64^{+26}_{-22}$TNU the uncertainties are still to large to make any judgments and new measurements with collection of higher statistics desired.

Another important attribute of the model is the radiogenic heat production rate. Here crust contributes 6.8 TW, which agree with earlier estimates (Table 3.6).

5.4 Model uncertainties

The estimated local contribution to geoneutrino signal at LNGS has uncertainty of the same order of magnitude as signal from the rest of the crust (Table 5.1), which was the aim of this study.

In spite of the more detailed study the total uncertainty of the model didn't decrease with respect to previous calculation. It is explained by incorporation of new sources of uncertainties, which were not considered earlier.

Geoneutrino signals from local and global contributions are assumed to be affected by independent uncertainties.

6 Conclusion

With the aim of estimation of the total geo-neutrino signal at Borexino and its associated uncertainties global and local models of crust were developed here. Thickness of the whole crust was obtained from the average of the three geophysical global crustal models based on reflection and refraction seismic body wave (CRUST 2.0), surface wave dispersion (CUB 2.0), and gravimetric anomalies (GEMMA). Uncertainty was estimated as the half-range. It yields the average crustal thicknesses of 34.4±4.1 km in the continents and 8.0±2.7 km in the oceans. HPE's abundances in sediments and upper crust were adopted from the previous measurements [*Plank, 2013; White and Klein, 2013; Rudnick and Gao, 2003*]. Abundances in the middle and lower continental crust were calculated by using seismic arguments and composition of felsic and mafic rocks [*Huang et al., 2013*]. The developed global crustal reference Earth model is digitalized on 1°×1° scale.

The average continental crust derived here contains $1.31^{+0.29}_{-0.25}$ μg/g U, $5.61^{+1.59}_{-0.89}$ μg/g Th and $1.52^{+0.29}_{-0.22}$ wt. % K, has Th/U = $4.3^{+1.6}_{-1.0}$, K/U = $11{,}621^{+3{,}512}_{-2{,}516}$ and produces $6.8^{+1.4}_{-1.1}$ TW of heat. These asymmetric uncertainties are propagated from the non-Gaussian distributions of HPE abundances in the deep continental crust and continental lithospheric mantle using Monte Carlo simulation.

For the local study there were selected twenty four 1°×1° tiles around Gran Sasso. Geophysical properties of the crust in this area were calculated from the available publications. Amount of HPEs was measured by collecting representative rocks.

The geoneutrino signal from the continental lithospheric mantle is calculated here for the first-time based on an updated xenolithic peridotite database [*Huang et al., 2013*]. The calculated geoneutrino signal from the CLM exceeds that from the OC.

For the rest of the mantle a generally accepted model were used.

The total geoneutrino signal at Borexino for the new reference model of crust is equal to $34.3^{+4.4}_{-2.9}$ TNU. 7 TNU reduction of the signal respect to the previous publication is discussed in the text.

The main two sources of uncertainties were considered: the physical structure (geophysical uncertainty) and the abundances of HPEs in the reservoirs (geochemical uncertainty). Contributions from the two different sources of uncertainty to the global uncertainties are estimated for the first time, and it is shown that the geochemical uncertainty exerts the greatest control on the overall uncertainties.

The antineutrino background from nuclear reactors was examined. Operating experience of all commercial nuclear reactors in the last four years was collected in one database. Three different power fractions for 3 main types of reactor's fuel burn cycles, used in the world, were considered.

Bibliography

Abe S. et al. The KamLAND Collaboration (2008), Precision measurement of neutrino oscillation parameters with KamLAND. Phys. Rev. Lett. 100, 221803(1-5), doi: 10.1103/PhysRevLett.100.221803.

Allègre, C. J., A. Hofmann, and K. O'Nions (1996), The argon constraints on mantle structure. Geophys. Res. Lett., 23(24), 3555-3557, doi: 10.1029/96gl03373.

Allègre, C. J., J.-P. Poirier, E. Humler, and A. W. Hofmann (1995), The chemical composition of the Earth, Earth and Planetary Science Letters, 134(3–4), 515-526, doi: 10.1016/0012-821x(95)00123-t.

Alimonti G., et al., Borexino Collaboration (2009a), The Borexino detector at the Laboratori Nazionali del Gran Sasso, Nucl. Instr. Methods A 600, 568.

Alimonti G., et al., Borexino Collaboration (2009b), The liquid handling systems for the Borexino solar neutrino detector, Nucl. Instr. Methods A 609, 58.

Anderson, D. L. (2007), New theory of the Earth, Cambridge University Press.

Araki, T., et al. (2005), Experimental investigation of geologically produced antineutrinos with KamLAND, Nature, 436(7050), 499-503, doi: 10.1038/nature03980.

Arevalo, R., and W. F. McDonough (2010), Chemical variations and regional diversity observed in MORB, Chemical Geology, 271(1-2), 70-85, doi: 10.1016/j.chemgeo.2009.12.013.

Arevalo, R., W. F. McDonough, and M. Luong (2009), The K/U ratio of the silicate Earth: Insights into mantle composition, structure and thermal evolution, Earth and Planetary Science Letters, 278(3-4), 361-369, doi: 10.1016/j.epsl.2008.12.023.

Arevalo, R., W. F. McDonough, A. Stracke, M. Willbold, T. I. Ireland, and R. J. Walker (2012), Th abundances and radiogenic heat generation in OIB sources, Nature Geoscience, under review.

Arpesella C., et al., Borexino Collaboration (2008a), First real time detection of ^{7}Be solar neutrinos by Borexino, Phys. Lett. B 658,101-108.

Arpesella C., et al., Borexino Collaboration (2008b), Direct Measurent of the ^{7}Be Solar Neutrino Flux with 192 Days of Borexino Data, Phys. Rev. Lett. 101, 091302.

Artemieva, I. M. (2006), Global 1°×1° thermal model TC1 for the continental lithosphere: Implications for lithosphere secular evolution, Tectonophysics, 416(1-4), 245-277, doi: 10.1016/j.tecto.2005.11.022.

Bassin, C., G. Laske, and T. G. Masters (2000), The current limits of resolution for surface wave tomography in North America, EOS Trans.

Behn, M. D., and P. B. Kelemen (2003), Relationship between seismic P-wave velocity and the composition of anhydrous igneous and meta-igneous rocks, Geochem. Geophys. Geosyst., 4(5), 1041, doi: 10.1029/2002gc000393.

Bellini, G., et al. (2010), Observation of geo-neutrinos, Physics Letters B, 687(4–5), 299-304, doi: 10.1016/j.physletb.2010.03.051.

Bellini G. et al. (2010b), Measurement of the solar ^{8}B neutrino rate with a liquid scintillator target and 3 MeV energy threshold in the Borexino detector, Phys. Rev. D 82, 033006.

Bellotti E. (1988) The Gran Sasso Underground Laboratory. Nucl. Instr. and Meth. A264, 274-277.

Bemporad, C., G. Gratta, and P. Vogel (2002), Reactor-based neutrino oscillation experiments, Reviews of Modern Physics, 74(2), 297-328, doi: 10.1103/RevModPhys.74.297.

Bevington, P. R., and D. K. Robinson (2003), Data reduction and error analysis for the physical sciences, 3rd ed., McGraw-Hill, Boston.

Billi A., Tiberti M. M., Cavinato G. P., Cosentino D., Di Luzio E., Keller J. V. A., Kluth, C., Orlando L., Parotto M., Praturlon A., Romanelli M., Storti F. and Wardell N. (2006) First results from the CROP-11 deep seismic profile, central Apennines, Italy: Evidence of mid-crustal folding. J. Geol. Soc. London 163. 583–586.

Boriani A., Origoni Giobbi E., Borghi A. and Caironi V. (1990) The evolution of the “Serie dei Laghi” (Strona-Ceneri and Schisti dei Laghi): the upper component of the Ivrea-Verbano crustal section, Southern Alps, North Italy and Ticino, Switzerland. Tectonophysics 182, 103–118.

Boriani A., Sassi F. P. and Sassi R. (2003) The Basement Complexes in Italy, with special regards to those exposed in the Alps: a review. Episodes 26(3), 186-192

Boyet, M., and R. W. Carlson (2005), 142Nd evidence for early (>4.53 Ga) global differentiation of the silicate Earth, Science, 309(5734), 576-581, doi: 10.1126/science.1113634.

Čadek, O., and Z. Martinec (1991), Spherical harmonic expansion of the Earth's crustal thickness up to degree and order 30, Studia Geophysica et Geodaetica, 35(3), 151-165, doi: 10.1007/bf01614063.

Campos Venuti G., Esposito A., Grisanti A., Grisanti G., Pelliccioni M. and Risica S. (1982) Internal report of INFN, LNF 82/78(R).

Cassinis R., Scarascia S. and Lozej A. (2005) Review of seismic Wide-Angle Reflection-Refraction (WARR) Results in the Italian Region (1956-1987). In CROP PROJECT: Deep Seismic Exploration of the Central Mediterranean and Italy (ed. Finetti I. R.). Elsevier, Amsterdam. pp 31-56.

Cavinato G. P. and De Celles P. G. (1999) Extensional basins in the tectonically bimodal central Apennines fold-thrust belt, Italy: Response to corner flow above a subducting slab in retrograde motion. Geology 27 (10), 955-958.

Chen, M. C. (2006), Geo-neutrinos in SNO+, Earth, Moon, and Planets, 99(1-4), 221-228, doi: 10.1007/s11038-006-9116-4.

Christensen, N. I., and W. D. Mooney (1995), Seismic velocity structure and composition of the continental crust: A global view, J. Geophys. Res.-Solid Earth, 100(B6), 9761-9788, doi: 10.1029/95jb00259.

Coltorti, M., et al. (2011), U and Th content in the Central Apennines continental crust: A contribution to the determination of the geo-neutrinos flux at LNGS, Geochimica et Cosmochimica Acta, 75(9), 2271-2294, doi: 10.1016/j.gca.2011.01.024.

Conrad, C. P., and C. Lithgow-Bertelloni (2006), Influence of continental roots and asthenosphere on plate-mantle coupling, Geophysical Research Letters, 33(5), doi: 10.1029/2005gl025621.

Dal Piaz G. V. and Martin S. (1998) Evoluzione litosferica e magmatismo nel dominio austoalpino dall'orogenesi varisica al rifting permo–mesozoico. Mem. Soc. Geol. It. 53, 43–62.

D'Amico C., Del Monte M. and Gandolfi G. (1971) Multiple intusions in the Cima d'Asta pluton (Northern Italy). Contrib. Mineral. Petrol. 31, 13-27.

De Marchi G., Quick J. E., Sinigoi S. and Mayer A. (1998) Pressure Gradient and Original Orientation of a Lower-Crustal Intrusion in the Ivrea-Verbano Zone, Northern Italy. J. Geol. 106, 609-605.

Di Luzio E., Mele G., Tiberti M. M., Cavinato G. P. and Parotto M. (2009) Moho deepening and shallow upper crustal delamination beneath the central Apennines. Earth Planet. Sci. Lett. 280, 1-12.

Djurcic Z., Detwiler J. A., Piepke A., Foster Jr. V. R., Miller L., and Gratta G. (2009), Uncertainties in the anti-neutrino production at nuclear reactors. J. Phys. G: Nucl. Part. Phys. 36, 045002, doi:10.1088/0954-3899/36/4/045002

Dye, S. T. (2010), Geo-neutrinos and silicate earth enrichment of U and Th, Earth and Planetary Science Letters, 297(1-2), 1-9, doi: 10.1016/j.epsl.2010.06.012.

Dye, S. T. (2012), Geoneutrinos and the radioactive power of the Earth, Reviews of Geophysics, 50(3), doi: 10.1029/2012rg000400.

Dziewonski, A. M., and D. L. Anderson (1981), Preliminary reference Earth model, Physics of the Earth and Planetary Interiors, 25, 297-356, doi: 10.1016/0031-9201(81)90046-7.

Enomoto, S., 2005, Neutrino Geophysics and Observation of Geo-Neutrinos at KamLAND, Ph.D. thesis, Tohoku University, available online at http://www.awa.tohoku.ac.jp/~sanshiro/research/SanshirosDoctoralDissertation.pdf.

Eder G. (1966) Terrestrial neutrinos. Nucl. Phys. 78, 657-662.

Enomoto, S., E. Ohtani, K. Inoue, and A. Suzuki (2007), Neutrino geophysics with KamLAND and future prospects, Earth and Planetary Science Letters, 258(1-2), 147-159, doi: 10.1016/j.epsl.2007.03.038.

Firestone, R. B., and V. S. Shirley (1996), Table of Isotopes (John Wiley and Sons, Inc.), eighth edition, the numerical values available online: http://isotopes.lbl.gov/education/isotopes.htm.

Finetti I.R. (2005a), Crop Project: Deep Seismic Exploration of the Central Mediterranean and Italy. Elsevier, Amsterdam. 779p.

Finetti I.R. (2005b), Depth contour map of the Moho discontinuity in the Central Mediterranean region from new CROP seismic data. In CROP Project: Deep Seismic Exploration of the Central Mediterranean and Italy, Atlases in Geoscience 1 (ed. I. R. Finetti). Elsevier, The Netherlands. pp. 597–606.

Fiorentini, G., M. Lissia, and F. Mantovani (2007), Geo-neutrinos and earth's interior, Physics Reports, 453(5-6), 117-172, doi: 10.1016/j.physrep.2007.09.001.

Fiorentini, G., G. Fogli, E. Lisi, F. Mantovani, and A. Rotunno (2012), Mantle geoneutrinos in KamLAND and Borexino, Physical Review D, 86(3), doi: 10.1103/PhysRevD.86.033004.

Fiorentini, G., A. Ianni, G. Korga, M. Lissia, F. Mantovani, L. Miramonti, L. Oberauer, M. Obolensky, O. Smirnov, and Y. Suvorov (2010), Nuclear physics for geo-neutrino studies, Physical Review C, 81(3), doi: 10.1103/PhysRevC.81.034602.

Fogli, G. L., E. Lisi, A. Palazzo, and A. M. Rotunno (2006), Geo-neutrinos: A systematic approach to uncertainties and correlations, Earth, Moon, and Planets, 99(1-4), 111-130, doi: 10.1007/s11038-006-9107-5.

Fogli, G. L., E. Lisi, A. Marrone, A. Palazzo, and A. M. Rotunno (2011), Evidence of θ13>0 from global neutrino data analysis, Physical Review D, 84(5), 053007, doi: 10.1103/PhysRevD.84.053007.

Franz L. and Romer R. L. (2007) Caledonian high-pressure metamorphism in the Strona-Ceneri Zone (Southern Alps of southern Switzerland and northern Italy). Swiss J. Geosci. 100, 457 – 467.

Gao S., Luo T., Zhang B., Zhang H. Y. W., Zhao Z. and Hu Y. (1998) Chemical composition of the continental crust as revealed by studies in east China. Geochim. Cosmochim. Acta 62, 1959-1975

Gando, A., et al. (2011), Partial radiogenic heat model for Earth revealed by geoneutrino measurements, Nature Geosci, 4(9), 647-651, doi: 10.1038/ngeo1205.

Gung, Y., M. Panning, and B. Romanowicz (2003), Global anisotropy and the thickness of continents, Nature, 422(6933), 707-711, doi: 10.1038/nature01559.

C. A. Hagmann, and A. Bernstein (2003), IEEE Nuclear Science Symposium, Portland, OR, Oct 19-25.

Hacker, B. R., P. B. Kelemen, and M. D. Behn (2011), Differentiation of the continental crust by relamination, Earth and Planetary Science Letters, 307(3–4), 501-516, doi: 10.1016/j.epsl.2011.05.024.

Hahn A.A., Schreckenbach K., Gelletly W., von Feilitzsch F., Colvin G., and Krusche B. (1989), Antineutrino spectra from 241Pu and 239Pu thermal neutron fission products, Phys. Lett. B218, 365-368.

Hart, S. R., and A. Zindler (1986), In search of a bulk-Earth composition, Chemical Geology, 57(3–4), 247-267, doi: 10.1016/0009-2541(86)90053-7.

Hofmeister A.M., and Criss R.E (2005), Earth's heat flux revised and linked to chemistry, Tectonophysics 395, 159-177 (2005).

Holbrook, W. S., W. D. Mooney, and N. I. Christensen (1992), The seismic velocity structure of the deep continental crust, in Lower Continental Crust, edited by D. M. Fountain, R. Arculus and R. Kay, pp. 1-43, Elsevier, Amsterdam.

Huang, Y., Chubakov, V., Mantovani, M., Rudnick, R. L., and McDonough, W. F. (2013). A reference Earth model for the heat producing elements and associated geoneutrino flux. G-Cubed, under review.

Huang, Y., W. F. McDonough, and F. Mantovani (2012), Propagation of uncertainties in geochemistry by Monte Carlo simulation, Chemical Geology, under review.

Huber P., and Schwetz T. (2004), Precision spectroscopy with reactor anti-neutrinos, Phys. Rev. D70, 053011.

Hunziker J. C. and Zingg A. (1980) Lower Palaeozoic Amphibolite to Granulite Facies Metamorphism in the Ivrea Zone (Southern Alps, Northern Italy). Schweiz. Mineral. Petrogr. Mitt. 60, 181-213.

International Atomic Energy Agency (IAEA) http://www.iaea.org/: Nuclear Power Reactors in the World, Reference Data Series No.2, published since 1981; Operating Experience with Nuclear Power Plants in Member States, published since 1970.

Jaupart, C.,Labrosse,S.,Mareschal,J.-C. (2007).Temperatures, heat and energy in the mantle of the Earth. In: Bercovici D. (Ed.), Mantle Dynamics, Treatise on Geophysics, vol.7. Elsevier Scientific Publishing Company, NewYork, 253–303, http://dx.doi.org/10.1016/B978-044452748-6.00114-0. (Chap.7.06Editor-in-chiefG.Schubert).

Jaupart, C., and J. C. Mareschal (1999), The thermal structure and thickness of continental roots, Lithos, 48(1–4), 93-114, doi: 10.1016/s0024-4937(99)00023-7.

Jaupart, C., J. C. Mareschal, L. Guillou-Frottier, and A. Davaille (1998), Heat flow and thickness of the lithosphere in the Canadian Shield, Journal of Geophysical Research, 103(B7), 15,269-215,286.

Javoy, M., et al. (2010), The chemical composition of the Earth: Enstatite chondrite models, Earth and Planetary Science Letters, 293(3-4), 259-268, doi: 10.1016/j.epsl.2010.02.033.

Jordan, T. H. (1975), The continental tectosphere, Reviews of Geophysics, 13(3), 1-12, doi: 10.1029/RG013i003p00001.

Kramers, J. D., and I. N. Tolstikhin (1997), Two terrestrial lead isotope paradoxes, forward transport modelling, core formation and the history of the continental crust, Chemical Geology, 139(1–4), 75-110, doi: 10.1016/s0009-2541(97)00027-2.

Learned, J. G.; Dye, S. T.; Pakvasa, S. (2008), Hanohano: a deep ocean anti-neutrino detector for unique neutrino physics and geophysics studies". Proceedings of the Twelfth International Workshop on Neutrino Telescopes, Venice, March 2007. arXiv:0810.4975

Lyubetskaya, T, and Korenaga, J. (2007), Chemical composition of Earth's primitive mantle and its variance: 1. Method and results. J. Geophys. Res. 112, B03211.

Laske, G., and T. G. Masters (1997), A global digital map of sediment thickness, EOS Trans. AGU, 78 F483.

Laske, G., T. G. Masters, and C. Reif (2001), CRUST 2.0: A new global crustal model at 2 x 2 degrees, edited, http://igppweb.ucsd.edu/~gabi/crust2.html.

Le Bas, M. J., and A. L. Streckeisen (1991), The IUGS systematics of igneous rocks, Journal of the Geological Society, 148(5), 825-833, doi: 10.1144/gsjgs.148.5.0825.

Marx G. (1969) Geophysics by neutrinos. Czech. J. Phys. B19, 1471-1479.

Mantovani, F., L. Carmignani, G. Fiorentini, and M. Lissia (2004), Antineutrinos from Earth: A reference model and its uncertainties, Physical Review D, 69(1), doi: 10.1103/PhysRevD.69.013001.

McDonough, W. F. (1990), Constraints on the composition of the continental lithospheric mantle, Earth and Planetary Science Letters, 101(1), 1-18, doi: 10.1016/0012-821x(90)90119-i.

McDonough, W. F. (2003), Compositional model for The Earth's core, in The Mantle and Core, Vol. 2 Treatise on Geochemistry, edited by R. W. Carlson, 547-568, Elsevier, Oxford.

McDonough, W. F. (1999), in Encyclopedia of Geochemistry, edited by C. P. Marshall and R. F. Fairbridge (Kluwer Academic Publishers), 151–156.

McDonough, W. F., and S.-S. Sun (1995), The composition of the Earth, Chemical Geology,

120, 223-253, doi: 10.1016/0009-2541(94)00140-4.

McLennan, S. M. (2001), Relationships between the trace element composition of sedimentary rocks and upper continental crust, Geochem. Geophys. Geosyst., 2(4), doi: 10.1029/2000gc000109.

Mele G., Sandvol E. and Cavinato G. P. (2006) Evidence of crustal thickening beneath the central Apennines (Italy) from teleseismic receiver functions. Earth Planet. Sci. Lett. 249, 425-435.

Mention G., Fechner M., Lasserre Th., Mueller Th. A., Lhuillier D., Cribier M., and Letourneau A. (2011), The Reactor Antineutrino Anomaly, Phys. Rev. D 83, 073006, doi: 10.1103/PhysRevD.83.073006

Mooney, W. D., G. Laske, and T. G. Masters (1998), CRUST 5.1: A global crustal model at 5o x 5o, Journal of Geophysical Research, 103(B1), 727-747, doi: 10.1029/97JB02122.

Mostardini F. and Merlini S. (1986) Appennino centro-meridionale: sezioni geologiche e proposta di modello strutturale. AGIP Mineraria, Atti 73° Congresso Soc. Geol. It., 1-59.

Murakami, M., Y. Ohishi, N. Hirao, and K. Hirose (2012), A perovskitic lower mantle inferred from high-pressure, high-temperature sound velocity data, Nature, 485(7396), 90-94, doi: 10.1038/nature11004.

NASA Database
http://gcmd.nasa.gov/KeywordSearch/Metadata.do?Portal=GCMD&KeywordPath=&NumericId=449&MetadataView=Text&MetadataType=0&lbnode=mdlb2

Nataf, H.-C., and Y. Richard (1996), 3SMAC: an a priori tomographic model of the upper mantle based on geophysical modeling, Physics of the Earth and Planetary Interiors, 95, 101-122, doi: 10.1016/0031-9201(95)03105-7.

Negretti, M., M. Reguzzoni, and D. Sampietro (2012), A web processing service for GOCE data exploitation, in First International GOCE Solid Earth workshop, edited, Enschede, The Netherlands.

O'Neill, H. S. C., and H. Palme (2008), Collisional erosion and the non-chondritic composition of the terrestrial planets, Philosophical Transactions of the Royal Society A: Mathematical, Physical and Engineering Sciences, 366(1883), 4205-4238, doi: 10.1098/rsta.2008.0111.

Pollack, H. N., Hurter S. J., and Johnson J. R. (1993) Heat flow from the earth's interior: analysis of the global data set, Reviews of Geophysics 31, 267-280, doi: 10.1029/93RG01249.

Pail, R., et al. (2011), First GOCE gravity field models derived by three different approaches, Journal of Geodesy, 85(11), 819-843, doi: 10.1007/s00190-011-0467-x.

Palme, H., and H. S. C. O'Neill (2003), Cosmochemical estimates of mantle composition, in The Mantle and Core, Vol. 2 Treatise of Geochemistry, edited by R. W. Carlson, pp. 1-38, Elsevier, Oxford.

Pasyanos, M. E. (2010), Lithospheric thickness modeled from long-period surface wave dispersion, Tectonophysics, 481(1-4), 38-50, doi: 10.1016/j.tecto.2009.02.023.

Patacca E., Scandone P., Di Luzio E., Cavinato G. P. and Parotto M. (2008) Structural architecture of the central Apennines: Interpretation of the CROP 11 seismic profile from the Adriatic coast to the orographic divide, Tectonics 27, TC3006, 1-36.

Plank T. and Langmuir C. (1998) The chemical composition of subducting sediment and its consequences for the crust and mantle. Chem. Geol. 145, 325-394.

Plank, T. (2013), The chemical composition of subducting sediments, in Treatise of Geochemistry, 2nd edition, edited.

Pollack, H. N., and D. S. Chapman (1977), On the regional variation of heat flow, geotherms, and lithospheric thickness, Tectonophysics, 38(3–4), 279-296, doi: 10.1016/0040-1951(77)90215-3.

Ponziani F., De Franco R., Minelli G., Biella G., Federico C. and Pialli G. (1995) Crustal shortening and duplication of the Moho in the Northern Appennines: a view from seismic refraction data. Tectonophysics 252, 391-418.

Quick J., Sinigoi S., Negrini L., Demarchi G., and Mayer A. (1992), Synmagmatic deformation in the underplated intrusive complex of the Ivrea–Verbano Zone: evidence and implications. Geology 20, 613–616.

Quick J. E., Sinigoi S., Snoke A. W., Kalakay T. J., Mayer A., and Peressini G. (2003), Geologic Map of the Southern Ivrea–Verbano Zone, Northwestern Italy. U.S. Geological Survey I-Map, 2776.

Rae H.K. (1997), Reactor Physics and Control, in D.G. Hurst, ed., Canada Enters the Nuclear

Age. A Technical History of Atomic Energy of Canada Limited. Montreal: McGill-Queen's University Press for Atomic Energy of Canada Limited, 1997, 215-232.

Reguzzoni, M., and N. Tselfes (2009), Optimal multi-step collocation: application to the space-wise approach for GOCE data analysis, Journal of Geodesy, 83(1), 13-29, doi: 10.1007/s00190-008-0225-x.

Reguzzoni, M., and D. Sampietro (2012), Moho estimation using GOCE data: A numerical simulation, in Geodesy for Planet Earth, edited by S. Kenyon, M. C. Pacino and U. Marti, pp. 205-214, Springer Berlin Heidelberg.

Robert, C. P., and G. Casella (2004), Monte Carlo statistical methods 2nd edition, Springer, New York.

Rubinstein, R. Y., and D. P. Kroese (2008), Simulation and the Monte Carlo Method, Student Solution Manual, 2nd Edition, edited, John Wiley & Sons. Inc. , Hoboken, New Jersey.

Rudnick, R. L., and D. M. Fountain (1995), Nature and composition of the continental crust: A lower crustal perspective, Reviews of Geophysics, 33(3), 267-309, doi: 10.1029/95rg01302.

Rudnick, R. L., and A. A. Nyblade (1999), The composition and thickness of Archean continental roots: constraints from xenolith thermobarometry, in Mantle Petrology: Field Observations and High-Pressure Experimentation: A Tribute to Francis R. (Joe) Boyd, edited by Y. Fei, C. M. Bertka and B. O. Mysen, pp. 3-12, Geochemical Society Special Publication 6.

Rudnick, R. L., and S. Gao (2003), Composition of the continental crust, in The Crust, Vol. 3 Treatise on Geochemistry, edited by R. L. Rudnick, pp. 1-64, Elsevier, Oxford.

Strumia, A., and F. Vissani (2003) Precise quasielastic neutrino/nucleon cross section, Phys. Lett. B564, 42-54, doi: 10.1016/S0370-2693(03)00616-6.

Sassi F. P., Cesare B., Mazzoli C., Peruzzo L., Sassi R. and Spiess R. (2004) The cristalline basement of the Italian eastern Alps: a review of the metamorphic features. Per. Miner. 73, 23-42.

Schnetger B. (1994) Partial melting during the evolution of the amphibolite- to granulite-facies gneisses of the Ivrea Zone, northern Italy. Chem. Geol. 113, 71-101.

Schreckenbach K., Colvin G., Gelletly W., and von Feilitzsch F. (1985), Determination of the antineutrino spectrum from 235U thermal neutron fission products up to 9.5 MeV, Phys. Lett.

B160, 325-330.

Shapiro, N. M., and M. H. Ritzwoller (2002), Monte-Carlo inversion for a global shear-velocity model of the crust and upper mantle, Geophysical Journal International, 151, 88-105, doi: 10.1046/j.1365-246X.2002.01742.x.

Sramek, O., W. F. McDonough, E. S. Kite, V. Lekic, S. T. Dye, and S. Zhong (2012), Geophysical and geochemical constraints on geoneutrino fluxes from Earth's mantle, Earth and Planetary Science Letters, in press, doi: 10.1016/j.epsl.2012.11.001.

Taylor, S. R., and S. M. McLennan (1995), The geochemical evolution of the continental crust, Rev. Geophys., 33(2), 241-265, doi: 10.1029/95rg00262.

Telford W. M., Geldart L. P. and Sheriff R. E. (1990) Applied Geophysics. Cambridge University Press. 771 p.

Tenzer, R., K. Hamayun, and P. Vajda (2009), Global maps of the CRUST 2.0 crustal components stripped gravity disturbances, Journal of Geophysical Research, 114(B5), doi: 10.1029/2008jb006016.

Turcotte, D. L., and G. Schubert (2002), Geodynamics, applications of continuum physics to geological problems Cambridge University Press, second edition.

Turcotte, D. L., D. Paul, and W. M. White (2001), Thorium-uranium systematics require layered mantle convection, J. Geophys. Res., 106(B3), 4265-4276, doi: 10.1029/2000jb900409.

Vogel P. (2007), Conversion of electron spectrum associated with fission into the antineutrino spectrum, Phys. Rev. C 76, 025504, doi: 10.1103/PhysRevC.76.025504

van der Hilst, R. D., S. Widiyantoro, and E. R. Engdahl (1997), Evidence for deep mantle circulation from global tomography, Nature, 386(6625), 578-584, doi: 10.1038/386578a0.

Wedepohl, K. H. (1995), The composition of the continental crust, Geochimica et Cosmochimica Acta, 59(7), 1217-1232, doi: 10.1016/0016-7037(95)00038-2.

White, W. M., and E. M. Klein (2013), The oceanic crust, in Treatise of Geochemistry, 2nd edition, edited.

World Nuclear Association http://www.world-nuclear.org/info/inf29.html